



UNIVERSITY OF TWENTE.

Faculty of Water Engineering
and Management

Mangrove dynamics in the Richmond River's estuary

Steven J. W. Hoogeveen

M.Sc. Thesis

December 2020

Supervisors:

dr. ir. E. M. Horstman
prof. dr. K. M. Wijnberg
dr. D. J. Stokes
ir. R. Gijsman

Marine and Fluvial Systems
Faculty of Engineering Technology
University of Twente
P.O. Box 217
7500 AE Enschede
The Netherlands

Acknowledgements

This research is the final work of my MSc Civil Engineering and Management at the Water Engineering and Management department at the University of Twente. During the last 2.5 years I felt at home due to all the water related courses. The highlight of this period was the field campaign in Australia, where I had the opportunity to study the remote and harsh but amazing mangrove environment.

This research project would not have been possible without the help of a number of people. First, I would like to thank my graduation committee consisting of Erik Horstman, Debra Stokes, Rik Gijsman and Kathelijne Wijnberg for their supervision and support throughout this project. Debra, thank you for everything during my stay in Australia, you really made me feel at home. The moments where we would swear at the millions mozzies while plowing through the dense trees and branches are unforgettable, but you made these moments a lot more bearable. I also appreciate the supplied data after I unfortunately had to fly back home. Erik, thank you for giving me the opportunity to go to Australia and for all the meetings we had. Those (many) meetings really helped me in my thought process, and gave structure and direction to my research. I also can't thank you enough for all the time and effort you put into this, because of you I was able to get through it. Rik, you provided a lot of new insights and valuable comments during my proposal and thesis for which I am very grateful. I would also like to thank Kathelijne for her time and effort and for the feedback on the report. I also appreciate Pim Willemsen for his help with my modelling problems.

Furthermore I want to thank Marijn Gelderland and Shawnee Bandhoe for their help setting-up the models. You were always willing to answer my questions, despite being graduated and maybe trying to forget Delft-FM. Likewise, special thanks to my friends, roommates and lichting 17 for their help and support.

Lastly, I would like to thank my parents and sister for their ongoing support, motivation and patience and for giving me the confidence to keep going. Without them, this final product would not have been possible.

I hope that this thesis will evoke your curiosity towards mangroves just as much as the research did to me, and that you enjoy reading it.

*S.J.W. Hoogeveen
Enschede, December 2020*

Abstract

Coastal ecosystems such as mangroves can reduce risk of flooding and wave damage to people and infrastructure from wave. The continued provision of these coastal defence services by mangroves is dependent on their capacity to adapt to long-term (anthropogenic) stresses such as sea level rise, decrease in sediment supply and coastal squeeze. Mangrove forest width is thought to be an important factor for the adaptation capacity of mangroves. Therefore, the aim of this research is to gain insight in the morphodynamic response of two transects of different mangrove forest widths, when variations in river discharge and fluvial sediment concentrations are considered.

In order to accurately assess the impact of mangrove width on the hydro- and morphodynamics, a case study of the South Ballina mangrove forest, which is evidently characterising for mangroves along the coast of New South Wales (NSW), has been executed. Quantitative field data regarding topography, vegetation and sediment characteristics were obtained. Field observations concluded that the effect of mangrove width on the biophysical properties and interactions is limited. This study concludes that the estuarine location, bio-geophysical settings and transect properties are the major causes for the observed differences within the mangrove forest, and not the mangrove width.

In addition to the field campaign, two depth-averaged process-based numerical models were developed in Delft-3D Flexible Mesh (DFM), which provided decent estimations of flow velocities and deposition rates. The two models allowed for comparison of the impact of mangrove width on the morphodynamic response to variable river discharges and fluvial sediment concentrations, by means of model simulations. The results from the model study regarding the effect of mangrove width on the biophysical properties and interactions remains inconclusive, since no clear comparison could be made regarding variations in mangrove width. During low discharge conditions, both models showed a turnaround from ebb-dominance towards flood-dominance throughout the spring-neap cycle. This could lead to an accumulation of water in the estuary, resulting in net accumulation of sediments in the river stream and foreshore. River flood conditions will lead to larger velocities within the forest at the 'long' transect compared to the 'short' transect, and is attributed to the width of the flow domain of the model. Furthermore, this study concludes that the Richmond River has a limited capacity for river flood discharge. When this capacity is exceeded, flooding of the adjoining mangroves as a traditional floodplain occurs. The mangroves then provide for floodwater storage and discharge as well as sediment deposition.

The findings in this study strongly indicate the need for a-periodic flood events to occur, in order for higher elevated parts of the mangrove forest to inundate and accrete. This study investigated a minor flood with a return period of one in two years. It is however likely that there is a limit towards the magnitude of the flood on one hand, and the amount of deposition in the forest on the other hand. This inverse proportion between the flood magnitude and the sediment trapping capacity should be investigated in future research.



Contents

Acknowledgements	i
Summary	iii
Abbreviations	vii
List of figures	x
List of tables	xi
1 Introduction	1
1.1 Definition of mangroves	2
1.2 Mangrove settings and types	2
1.3 Biophysical interactions in mangroves	5
1.4 Problem definition	8
1.5 Research objective	10
1.6 Report outline	11
2 Fieldwork methodology	14
2.1 Study area	14
2.2 Data collection	18
3 Fieldwork results	27
3.1 Elevation profile	27
3.2 Vegetation survey	28
3.3 Hydrodynamics	31
3.4 Total suspended solids	37
3.5 Sediment deposition	38
4 Model methodology	41
4.1 Model description	41
4.2 Model set-up	43
4.3 Model calibration	53
4.4 Validation	54
4.5 Scenarios	54
4.6 Calibration and scenario summary	56
5 Model results	59
5.1 Calibration	59
5.2 Validation	65
5.3 Scenario results	66

6 Discussion	78
6.1 Effect of mangrove width on mangrove dynamics	78
6.2 Effect of variations in river discharge characteristics on the behaviour of the mangrove system	80
6.3 Limitations	81
6.4 Applicability	83
7 Conclusions	85
7.1 The effect of mangrove width on the biophysical properties and interactions	85
7.2 The effect of mangrove width when seasonal variations are considered	85
8 Recommendations	88
References	89
Appendices	96
A Introduction to mangroves	96
A.1 Definition	96
A.2 Biological aspects	96
A.3 Ecological aspects	99
B Biophysical interactions	106
B.1 Hydrodynamics	106
B.2 Sediment dynamics	110
B.3 Morphodynamics	112
C Scenario results	115
C.1 Hydrodynamics	115
C.2 Morphodynamics	117
D Flood scenario quiver	119
E Direction of flow S-transect	121

Abbreviations

AHD	Australian Height Datum
DBH	Diameter at Breast Height
ET	EvapoTranspiration
ENSO	El Niño-Southern Oscillation
GIA	Glacial Isostatic Adjustment
LWT	Linear Wave Theory
MSL	Mean Sea level
NSW	New South Wales
RSET	Rod Surface-elevation table
SLR	Sea Level Rise
SSC	Suspended Sediment Concentration
TCM	TCM-4 Shallow Water Tilt Current Meter
TSS	Total Suspended Solids

List of Figures

1	Interactions in mangrove systems	1
2	Different root systems; Pneumatophores (l), knee roots (m), stilt roots (r) de Vos (2004)	2
3	White mangrove (l), Red mangrove (m), Black mangrove (r) de Vos (2004)	3
4	Five geomorphological settings for mangroves as stated by Woodroffe (1987) (de Vos, 2004). The red circles represent the focus of this study.	4
5	Mangrove forest types. Red circle indicates the type that is investigated in this study. (de Vos, 2004)	4
6	Environmental and biological factors influencing the surface elevation dynamics in mangroves (McIvor et al., 2013)	9
7	Flow chart of the research steps and the corresponding research questions Q.	12
8	Location of the study area	15
9	(Overview of the measurement locations of (b) the L-transect and (c) the S-transect (Imagery: Google Earth)	17
10	Location of the L-transect survey plots (Draper, 2017)	19
11	Overview of the set-up of a pressure gauge and conductivity sensor pair.	20
12	Set-up and schematic overview of the used Lowell TCM-4 Shallow Water Tilt Current Meter (TCM)'s	21
13	Visualisation of TTS sampling moments (black dots) during multiple spring-neap cycles.	23
14	The Rod Surface-elevation table (RSET) apparatus, shown schematically (Callaway et al., 2015)	24
15	(a) Set-up of the RSET in the field including sampling platforms and boardwalk (b) Close up of the RSET and measuring pins in order to map the height differences.	25
16	Elevation profile with respect to AHD of the S-transect, including instrument positions. Vegetation zones along the transect are demarcated by dashed lines. Characteristic tidal water levels are indicated near the left axis (HHWL = highest high water level; MSL = Mean Sea Level; LLWL = lowest low water level)	27
17	Elevation profile with respect to AHD of the L-transect, including instrument positions. Vegetation zones along the transect are demarcated by dashed lines. The locations of the vegetation survey plots are located at the bottom of the graph (Fringe Plot I; Inner Plot I-V). Characteristic tidal water levels are indicated near the left axis (HHWL = highest high water level; MSL = Mean Sea Level; LLWL = lowest low water level)	28
18	Tree count and species distribution with distance from the seaward fringe at the L-transect (after work by Draper (2017))	28
19	Location of the two different vegetation zones per transect	29
20	Water level at the S-transect measured between 4 and 19 of March. The blue line indicates S1, red is the station at S3.	31
21	Water level at L1 measured between 19 of March and 28 of April. The blue line indicates L1, red is the station at L3.	32
22	Measured flow velocities S1. Red dots indicate the data points, the orange line is the moving average of these data points.	33

23	Close up of the flow velocities S1 during spring (top) and neap (bottom) tides. Red dots indicate the data points, the orange line is the moving average of these data points. The dashed blue line is the observed water level.	34
24	Direction of flow during spring tides (left) and neap tides (right) at S1 in cm/s. The black line indicates the relative position of the forest fringe. Inner circles represent the degree of occurrence.	34
25	Flow velocities L1. Red dots indicate the data points, the orange line is the moving average of these data points.	35
26	Close up of the flow velocities L1. Red dots indicate the data points, the orange line is the moving average of these data points. The dashed blue line is the observed water level.	36
27	Direction of flow during spring tides (left) and neap tides (right) at L1 in cm/s. The black line indicates THE relative position of the forest fringe. Inner circles represent the degree of occurrence.	36
28	Total suspended solids (TSS) ($mg L^{-1}$) at both sites, during high- and low-tide in the spring-neap cycle. Each '+' represents one measurement	37
29	Location of the domain of both models within the estuary.	44
30	A schematisation of the domain for the S-transect (left) and L-transect (right), along with the different grid sizes and boundaries.	45
31	Initial elevation of both models in cross-shore direction. The initial profile is uniform in along-river direction. Characteristic tidal water levels are indicated near the left axis (HHWL = highest high water level; MSL = Mean Sea Level; LLWL = lowest low water level)	46
32	Front view of the sparse <i>Avicennia marina</i> (left) and dense <i>Aegiceras corniculatum</i> (right).	47
33	Reconstruction of the tidal signal along with observed water levels at Byrnes Point (top) and S1 and L1 (bottom).	48
34	Scaling and transformation of the discharge boundary based on ratios in the water level boundary.	50
35	Constructed discharge and reconstructed tidal boundary conditions (top). The marked grey area indicates the time period of the bottom plot, where a close up of the discharge and tide set-up is shown.	51
36	Tidal and discharge boundary settings for all scenarios. The marked areas indicate the modelled period for the S-transect (S) and L-transect (L). Calibration (CAL) and validation (VAL) time frames are indicated in the top plot.	56
37	X and Y component of the measured and modelled flow velocities at S1.	60
38	X and Y component of the measured and modelled flow velocities at L1.	60
39	Magnitude of the modelled and measured flow velocity at S1. Blue dashed line indicates the modelled water level.	61
40	Magnitude of the modelled and measured flow velocity at L1.	62
41	Results of the bed roughness calibration at S1.	63
42	Results of the bed roughness calibration at L1.	63
43	Observed and modelled sediment deposition for different suspended sediment concentrations and settling velocities (S-transect)	64
44	Observed and modelled sediment deposition for different suspended sediment concentrations and settling velocities (L-transect)	64

45	Observed flow velocities and modelled flow velocities during the calibration run for the S-transect. The model accuracy is are plotted in the upper left corner.	66
46	Observed flow velocities and modelled flow velocities during the calibration run for the S-transect. The model accuracy is are plotted in the upper left corner.	66
47	Modelled flow velocities at S1-3 for the three scenarios. The water levels plotted correspond with the reference/low flow scenario. Water levels during the flood scenario are constantly 2 m + AHD.	68
48	Modelled flow velocities at L1-3 for the three scenarios.The water levels plotted correspond with the reference/low flow scenario. Water levels during the flood scenario are constantly 2 m + AHD	70
49	Degree of deposition and erosion gradients across the area of interest S-transect (left). The black line indicates the location of the forest fringe. Red indicates erosion while blue indicates deposition. The right plot shows the average bed level profile after the run (between x = 100 and x = 200). Amounts of erosion/deposition are multiplied with a factor 15 for visibility.	72
50	Degree of deposition and erosion gradients across the area of interest L-transect (left). The black line indicates the location of the forest fringe. Red indicates erosion while blue indicates deposition. The right plot shows the average bed level profile after the run (between x = 100 and x = 200). Amounts of erosion/deposition are multiplied with a factor 15 for visibility.	75
52	White mangrove (l), Red mangrove (m), Black mangrove (r) de Vos (2004)	97
53	Different root systems; Pneumatophores (l), knee roots (m), stilt roots (r) de Vos (2004)	98
54	World distribution of mangroves showing their coastal extent (outlined) and two global hemispheres as discussed in text Duke (1992)	100
55	Five geomorphological settings for mangroves as stated by Woodroffe (1987) (de Vos, 2004)	101
56	Mangrove forest types de Vos (2004)	102
57	Schematic representation of the three thresholds that need to be reached during establishment of an <i>Avicennia</i> seedling (Balke et al., 2011)	104
58	Environmental and biological factors influencing the surface elevation dynamics in mangroves (McIvor et al., 2013)	114
59	Modelled flow velocities at S1 for the four scenario's	115
60	Modelled flow velocities at S1 for the four scenario's	116
61	Deposition and erosion gradients across the domain for all scenario's. The black line indicates the location of the forest fringe. Red indicates erosion while blue indicates deposition.	117
62	Deposition and erosion gradients across the domain for all scenario's. The black line indicates the location of the forest fringe. Red indicates erosion while blue indicates deposition.	118
63	Direction of flow during the flood scenario. The black line indicates the fringe.	119
64	Close up of the quiver during the flood scenario.	120
65	Possible directions of flow during flood and ebb tide near the S-transect. Red arrows indicate river discharge, blue arrows indicate saltwater.	121

List of Tables

1	Overview of equipment deployment including observed parameters, positioning, instrument settings and deployment duration	21
2	Sampling schedule TSS	23
3	Average tree and pneumatophore characteristics for all locations.	30
4	Averaged Total suspended solids (TSS) [mgL^{-1}] at both sites, during high- and low-tide in the spring-neap cycle.	38
5	Observed averaged sediment deposition rates and characteristic sediment properties at each of the monitoring locations	39
6	Observed average elevation change in mm/yr between 2016-2020.	39
7	Vegetation density n , diameter D and vegetation height h_v for the two vegetation zones.	47
8	Set-up overview for both transects.	52
9	Time frame of the runs	55
10	Overview of the calibration runs	57
11	Model accuracies (MA) of the calibration runs.	59
12	Overview of the calibration results and the scenario run set-up. Subscripts 'S' and 'L' indicate the transects.	65

1 Introduction

Globally, coastlines are under pressure as human population growth along coasts and urbanisation continue, while climate change leads to stormier weather and rising sea-levels. Conventional coastal engineering, e.g. the building of sea walls, dikes and embankments, used to be the ultimate solution to combat flood risks. However, to counter the ever increasing flood risk, continual and costly investments have to be made which are unsustainable (Temmerman et al., 2013). Another drawback of the conventional coastal engineering as mentioned by Borsje et al. (2011), Perkins et al. (2015) and Temmerman et al. (2013) is the inability of hard shorelines to naturally adapt to keep up with the relative sea-level rise. Ecosystem-based flood defence has been brought into large-scale practice in recent years as a more sustainable and sometimes even more cost-effective solution than conventional coastal engineering. By creating ecosystems, such as tidal marshes, mangroves, dunes and coral reefs, storm waves and storm surges can be naturally attenuated, and some these coastal systems can, under the right conditions, keep up with sea-level rise by natural accretion of sediments (Kirwan et al., 2010).

Mangroves are regarded as the second highest valued biome according to de Groot et al. (2012). The only biome with a higher economical value are coral reef ecosystems. These values are based on provisioning services (e.g. food, fresh water, wood), regulating services (e.g. climate, floods, diseases, purifying water), habitat services for different species and cultural services such as aesthetics or educational or recreational functions de Groot et al. (2012). This importance of mangrove forests asks for good management or protection of these forests. To manage these forests, knowledge is necessary about the processes that play a role in the mangrove system and how these processes interact. Three different components of the system, that interact through many different processes can be distinguished: mangrove growth and reproduction processes, hydrodynamic processes and morphodynamic processes. Mazda et al. (2005) summarise this interaction when they state that: *the mangrove ecosystem was constructed over a long span of time through feedback processes including the biotic activity, landform evolution and water flows.* This interaction is displayed in figure 1.

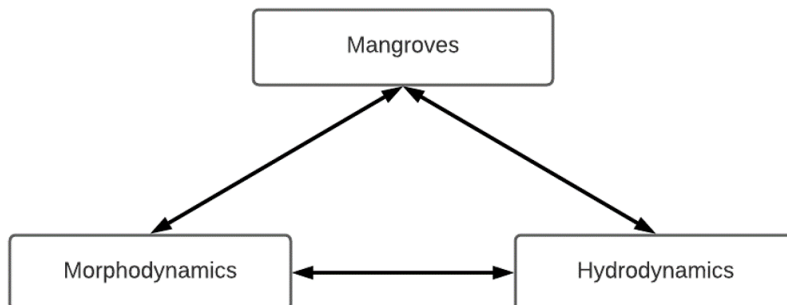


Figure 1: Interactions in mangrove systems

1.1 Definition of mangroves

The term 'mangrove' is used in two ways. First, it can be interpreted as a single tree or shrub, with specific attributes, e.g. viviparous propagulus, roots to support the above ground mass and special breathing structures such as, pneumatophores or other above-ground root structures, and small air-breathing lenticels (Duke, 1992). This enables them to grow in harsh and saline environments, such as the intertidal zone of marine coastal environments. The individual mangrove tree also has a very distinct above ground root structure, as seen in figure 2. These different root systems are further elaborated on in Appendix A: **Introduction to mangroves**. Secondly, the term mangroves can be used to indicate tropical coastal forests or ecosystems consisting of such species and their associated organisms (e.g. microbes, fungi, plants and animals), and can also be referred to as 'mangal' (Giri et al., 2011; Hutchings and Saenger, 1972; Tomlinson, 1986).

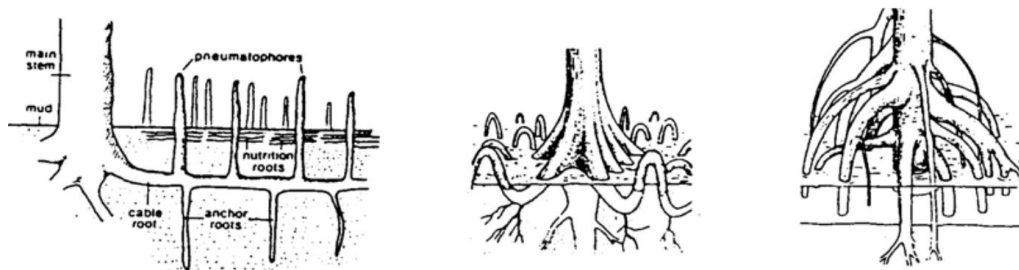


Figure 2: Different root systems; Pneumatophores (l), knee roots (m), stilt roots (r) de Vos (2004)

The classification of mangroves is not straightforward, species have often been categorized as 'true' mangroves and others as 'mangrove associates' (Duke, 1992). Lugo and Snedaker (1974) describe mangroves as a group of halophytic species belonging to twelve genera in eight different families. The combination of morphological and physical adaptations which is observed in this diverse group of plants have no equal among other plant families. Of all these species, the most well known and most common are the species of the genera *Rhizophora* and *Avicennia*. Their representatives, *Avicennia germinans* and *Rhizophora mangle*, are often referred to as, respectively, the 'Black mangrove' and the 'Red mangrove' (figure 52). Together with the 'White mangrove', *Laguncularia racemosa*, they are the main mangrove species in the New World (Oceania and the Americas). In the Old World, referring to Africa and Asia, the *Avicennia marina*, *Rhizophora mucronata* and those in the genera *Lumnitzera* and *Nypa* are most common Lugo and Snedaker (1974).

1.2 Mangrove settings and types

Mangroves occur in a number of environmental settings, consisting of particular suites of recurring land-forms while they differ in the physical processes responsible for sediment transport and deposition Woodroffe (1987). These environmental settings describe which particular combinations of geomorphological processes are dominant, which in turn affect the ecological constraints on the population and development of mangrove species Adame et al. (2010). The geophysical characteristics (e.g. climate,

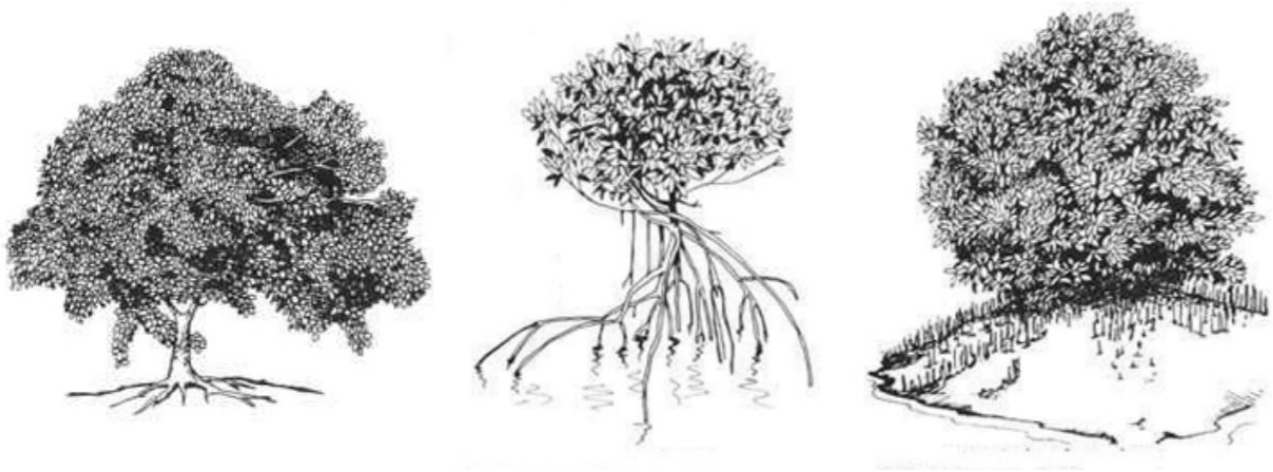


Figure 3: *White mangrove (l), Red mangrove (m), Black mangrove (r) de Vos (2004)*

tides and sea-level), the geomorphological characteristics (the dynamic history of the land surface and present-day geomorphological processes) and the biological characteristics (e.g. micro topographic, elevation and sediments, drainage and nutrient status) define the setting. Woodroffe (1987) gives a summary of the five environmental settings as described by Thom et al. (1975). A schematic representation can be seen in figure 4. The red circle represents the applicable environmental setting of this study; 'wave dominated barrier lagoon'. Coasts that are dominated by wave energy and where there is an abundant supply of sand, shore-parallel sandy ridges are formed. High wave energy and sandy substrates are usually not favourable for mangrove colonisation, but mangroves are found on the protected leeward side of the barriers and along the shores of the lagoon. An example of this is Tugerah Lake in Australia. An extensive description of each environmental setting can be found in Appendix A: [Introduction to mangroves](#).

Lugo and Snedaker (1974) developed a functional classification of mangrove forests, which is widely used and accepted. This classification consists of six categories and is shown in figure 5. This study focusses on the 'fringe' type mangroves. This forest type occurs along the fringes of protected shorelines and islands and is occurs most commonly along shorelines whose elevations are higher than mean tide. Due to the relatively open exposure along shorelines, the fringe forest is occasionally subjected to strong winds or storms. The other types are discussed extensively in Appendix A: [Introduction to mangroves](#).

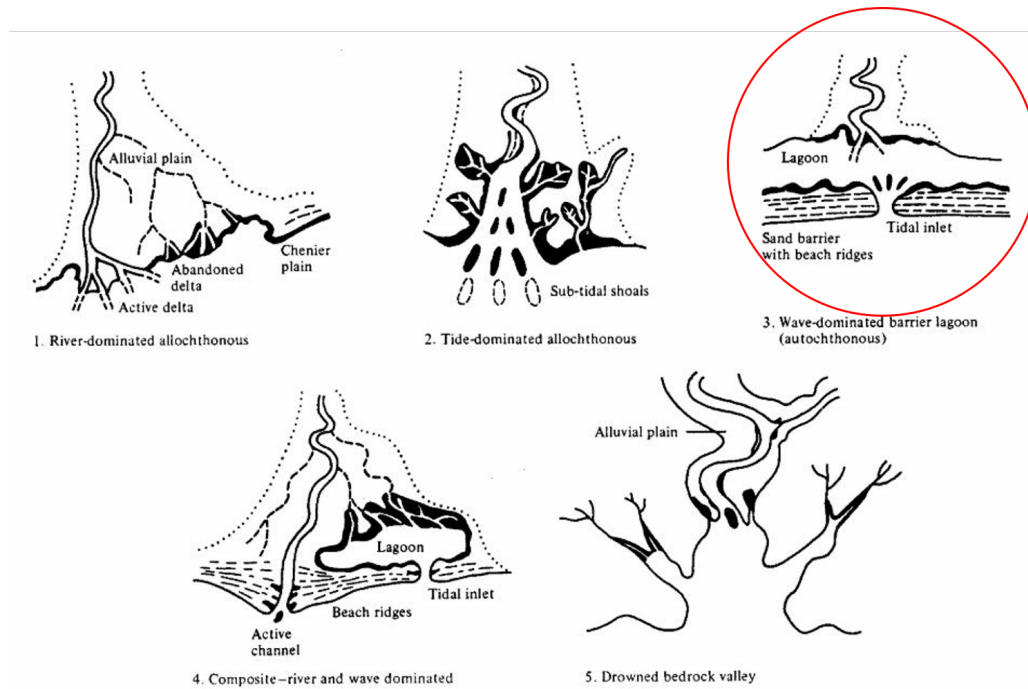


Figure 4: Five geomorphological settings for mangroves as stated by Woodroffe (1987) (de Vos, 2004). The red circles represent the focus of this study.

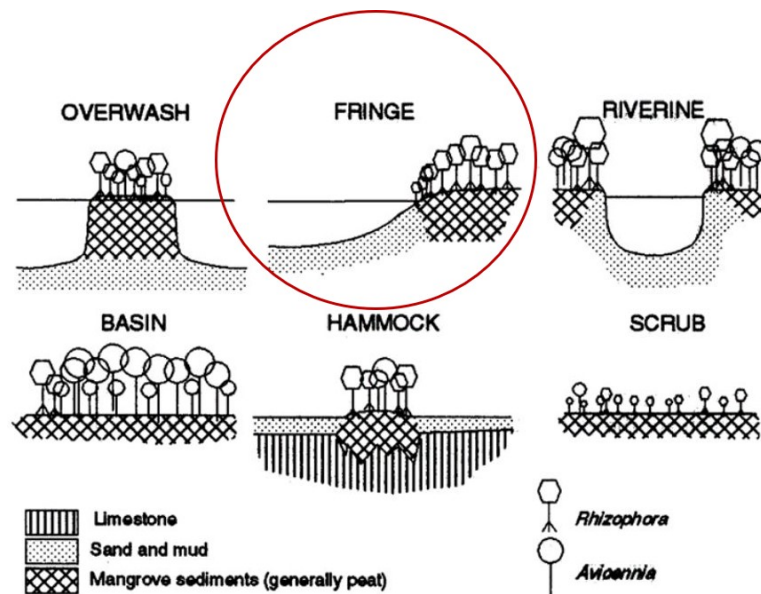


Figure 5: Mangrove forest types. Red circle indicates the type that is investigated in this study. (de Vos, 2004)

1.3 Biophysical interactions in mangroves

Biophysical interactions concern the impacts of hydrodynamic forces on vegetation and the land surface and inversely the feedback of vegetation on the hydrodynamics and sediment dynamics. With mangroves existing at the land-sea interface and being subject to inundations, physical processes related to hydrodynamics and morphodynamics shape the mangrove environment. The physical processes work at different time and length scales. The available knowledge on these physical processes that are of importance in a mangrove ecosystem are described in this section.

1.3.1 Hydrodynamics

This section will start with the hydrodynamics on the largest scales that are relevant to mangroves, and it will conclude with turbulence, which are the smallest scale of hydrodynamic forces. The processes are first described in a general way, and then applied to a mangrove environment.

Tides

The longest oceanic waves are those associated with the tides. They are characterised by the rhythmic rise (flood) and fall (ebb) of sea-level over a period of half a day or a day. The rise and fall are a result of the horizontal progression of water in the tidal wave (The Open University, 1999b; Roos, 2014). Tidal current velocities in mangroves are in general much lower than in the tidal creeks or in the waters in front of the mangrove forest and have a maximum of around 0,2 m/s (Furukawa et al., 1997). This observation is due to the presence of vegetation, which in turn causes extra turbulence that dissipates the tidal energy (Kazemi et al., 2019). This results in a gradient in flow velocity during ebb and flood tide in the creeks, often referred to as the 'tidal asymmetry'. This tidal asymmetry is acknowledged and described by i.a. Dronkers (1986); Furukawa et al. (1997) and Mazda et al. (1995). The latter found that the tidal current velocity in a mangrove creek is the sum of two components; u_H and u_A . u_H is due to tidal flows in a tidal channel without a floodplain, and is tidal symmetric. u_A is due to water exchange between the creek and the swamp, and shows a clear tidal asymmetry. A numerical model was developed by Horstman et al. (2015) to study the contributions of various bio-geophysical mangrove settings to these observed tidal dynamics. They concluded that the topography and relative elevation are the main drivers of this tidal flow routing, instead of vegetation density. Wolanski (1992) showed that tidal currents in the creek generally exceed 1 m/s , with stronger ebb currents than flood currents. As stated before, the lower velocities in the forests are mainly due to the energy dissipation by vegetation. The impact of this energy dissipation mechanism is larger compared to bottom friction (Mazda et al., 1997, 1995).

Turbulence

The most complex dynamics of water occurs on the smallest scale. This irregular motion results in chaotic changes in pressure and flow velocity, which is in contrast to laminar flow, where fluid flows in parallel layers with each layer moving smoothly past the adjacent layers with little or no mixing. The presence of vegetation or roughness introduces significant spatial variation to flow and turbulence, which ultimately affects the distribution of sediment within vegetated areas (Mullarney and Henderson, 2019). These obstacles also generate complex two-dimensional currents, with jets, eddies and stagnation regions (Furukawa et al., 1997). Drag forces and turbulent intensity depend on

properties of the flow (e.g. flow velocity and water depth) as well as the vegetation characteristics: the number, size, shape and flexibility of stems (Norris et al., 2017).

1.3.2 Sediment transport

In the following sub-sections, attention is given to sediment transport due to tides, waves and river discharge.

Sediment transport due to tides

The tidal asymmetry is acknowledged to be one of the major causes for the sediment deposition in mangroves Furukawa and Wolanski (1996). As mentioned before, the peak flood and ebb velocities during a tidal cycle are rarely of an equal magnitude. This leads to an effect called 'tidal pumping', where flood tides carry sediments farther upstream than ebb flows carry it downstream. This mechanism can trap sediments in the estuary (Woodroffe et al., 2016). Furukawa and Wolanski (1996) show that mangroves actively create their own ecosystems by trapping sediment. The trapping mechanism is due to the high micro-turbulence created by the flow around the vegetation, which maintains sediment in suspension at flood tidal currents. This sediment settles at the time of slack flood tide, when turbulence decreases. This sediment is not likely to re-entrain in vegetated areas by ebb tidal currents, because of the sluggish flow velocity. These processes result in a net input of sediments into the vegetated areas of mangroves, while the creeks are scoured by the enhanced ebb tidal outflow due to the tidal asymmetry Mazda et al. (1995). In their field study Horstman et al. (2017) observed increased sediment concentrations in front of vegetated areas, which might be due to the sediment's re-suspension.

Sediment transport due to waves

In addition to tidal currents, short waves also contribute to bringing and keeping sediment in suspension in estuaries. The orbital velocities of the waves protrude downward to the seabed, where they are able to entrain sediments. When sediment particles are entrained underneath waves and near the bed, the particles are transported into the mangrove forest due to the horizontal wave progression. Dronkers (1986) notices that waves counteract a landward residual transport of fine sediment by tidal currents, or enhance a seaward residual transport. However, the cross-shore sand transport, in particular the wave related component, is not fully understood due to the complex interaction processes between the flow, suspended sand and the seabed Van Rijn et al. (2013); Elfrink et al. (2006).

Sediment transport due to river discharge

Freshwater discharge appears to be an important external physical force that controls sediment deposition and transport to the continental shelf through estuaries Hossain et al. (2001). This physical process is largely controlled by seasonal changes of the river discharge pattern. Due to significant increases in current velocity and river discharge, net sediment transport rate increases during the rainy months. At this time, the buoyancy effect is important as freshwater is captured in the forest during high tide. In addition, the increased erosion rates due to the increase in discharge velocity contributes to the sediment budget at the foreshore of mangroves. The low discharges during the dry season result in a landward transport of sediment by tides. But, the reduced river discharges lowers the fluvial sediment input (Hossain et al., 2001; Hossain and Eyre, 2002; Saad et al., 1999). In the end, the average sediment accretion rate is lower during dry seasons compared to wet seasons Saad et al. (1999).

1.3.3 Morphodynamics

This sub-section gives an overview of the processes occurring in mangroves which are responsible for the mangrove morphodynamics. Sediment trapping processes enable mangroves to gain surface elevation when sea levels are rising. In order to understand when and where mangrove surface elevation is likely to be able to keep pace with sea level rise in the future, we need to understand the processes involved in surface elevation change. Figure 6 shows the environmental and biological factors influencing the mangrove surface elevation. These processes can be divided into surface processes and sub-surface processes (McIvor et al., 2013).

Surface processes

Surface processes include all processes which affect the material arriving at the sediment surface and the fate of this material. A distinction can be made into four processes; sedimentation, accretion, erosion and faunal processes (i.e. processes caused by animals that live within mangrove areas). According to McIvor et al. (2013) the factors which are likely to affect sedimentation rates in mangroves are the amount of incoming sediment and locally generated material, the period of inundation when external material can settle, and factors affecting whether particles are able to settle or are quickly re-suspended, including flow rates and flocculation of particles. Sedimentation also contributes to accretion, which occurs when the deposited material becomes fixed in place. In other words, when it can no longer be washed away by waves and tides (Krauss et al., 2008). Factors influencing the accretion are e.g. the growth of mangrove roots, formation of benthic mats and consolidation. Erosion refers to the loss of surface material caused by the top layer of the surface being sheared off by the flow of water. This leads to a loss in elevation. Erosion is dependent on the erodibility of the surface layer and the hydraulic stress. Finally, the surface is also affected by faunal processes such as algal mats Woodroffe (1987) and bioturbation Mullarney and Henderson (2019).

Sub-surface processes

McIvor et al. (2013) proposes a distinction between three groups of subsurface processes, namely: the growth and decomposition of mangrove roots and organic matter, the swelling and shrinkage of soils and the compaction or compression of soils (see figure 6). The growth and decomposition of mangrove vegetation is influenced by tree health, salinity, temperature, nutrient, tree species, and soil aeration. Some of these factors have already been mentioned in section A.3.4. These factors can have a positive effect on vegetation growth, and thus an increase in sub-surface expansion. Conversely, when roots decompose, they take up less space, causing a reduction in soil volume and resulting in shallow subsidence. The swelling and shrinkage of soils can be attributed to an increase or decrease in the soil water content. Compaction of soils usually refers to the consolidation of soils over time, as soil particles are packed closer together and moisture is forced out of the soil. McIvor et al. (2013) state that there is little known about the factors affecting the compaction and compression of mangrove soils. Important factors are likely to be the weight of material or water pressing down on the soil, the relative volumes of particles and pores, the soil composition (and particularly the organic content), and the depth of different soil layers.

1.3.4 Effect of Sea Level Rise

According to [McIvor et al. \(2013\)](#) sea level rise is expected to affect several of the surface elevation processes within mangroves. First, a rise in sea level will result in an increased hydro-period, during which sedimentation can occur, possibly resulting in increased accretion. Second, a rise in sea level will increase water depth, allowing waves to penetrate further into mangrove areas. This can in turn lead to an increase in re-suspension and erosion of sediments, or to an increase in sediment delivery into the forest. Third, an increase in water logging is expected, which in turn leads to an absence of oxygen and thus possibly affecting root growth. Finally, (brackish) groundwater levels are expected to rise, possibly affecting plant and sub-surface root growth. The above stated interactions are very hypothetical, since few studies have investigated them. However, it is clear that sea level rise could influence surface elevation change rates in multiple ways.

Sea Level Rise (SLR) requires mangroves to increase their surface elevation vertically (through sediment trapping or the addition of below-ground organic matter) and/or to move laterally inland to obtain an elevation gain that offsets the rate of SLR, so that the entire mangrove system maintains its relative position in the tidal frame ([Willemsen et al., 2016](#)). Where possible, space should be allowed behind mangroves for their landward migration in the face of sea level rise. This will ensure that mangroves can continue to exist along a coast, even if they are not able to remain in their current location. For as long as some mangrove areas remain intact, they can be expected to continue to provide coastal defence services, such as wave reduction, and other ecosystem services, such as supporting fisheries ([McIvor et al., 2013](#)).

The relationship between environmental factors and surface elevation change, and also any interactions between these processes are schematically shown in figure 6.

1.4 Problem definition

Mangroves are both some of the most vulnerable and most economically important ecosystems on Earth. Although these ecosystems are highly valued, a significant percentage has been lost due to direct conversion into agricultural land, aquaculture and industrialisation ([Kirwan et al., 2010](#); [Finlayson et al., 2013](#)). In addition, the conversion of mangroves to open water through SLR is expected to accelerate. Other long-term anthropogenic stresses such as a decrease in sediment supply and coastal squeeze appear to be major drivers in the future state of mangrove forests ([Craft et al., 2009](#)).

Mangroves can adapt to these direct and indirect anthropogenic stresses, as long as certain physical and ecological thresholds are not exceeded. Even though significant progress has been achieved in identifying and understanding above mentioned drivers, biophysical processes and relationships between these processes, quantitative knowledge about thresholds is still largely missing ([Lee et al., 2014](#)). Research shows the contribution of mangroves to accretion, either by peat formation or by accelerating sedimentation, however such research is limited in scope and geographic extent, so it needs to be reproduced in different settings to assess the function of mangroves more generally ([Lee et al., 2014](#)).

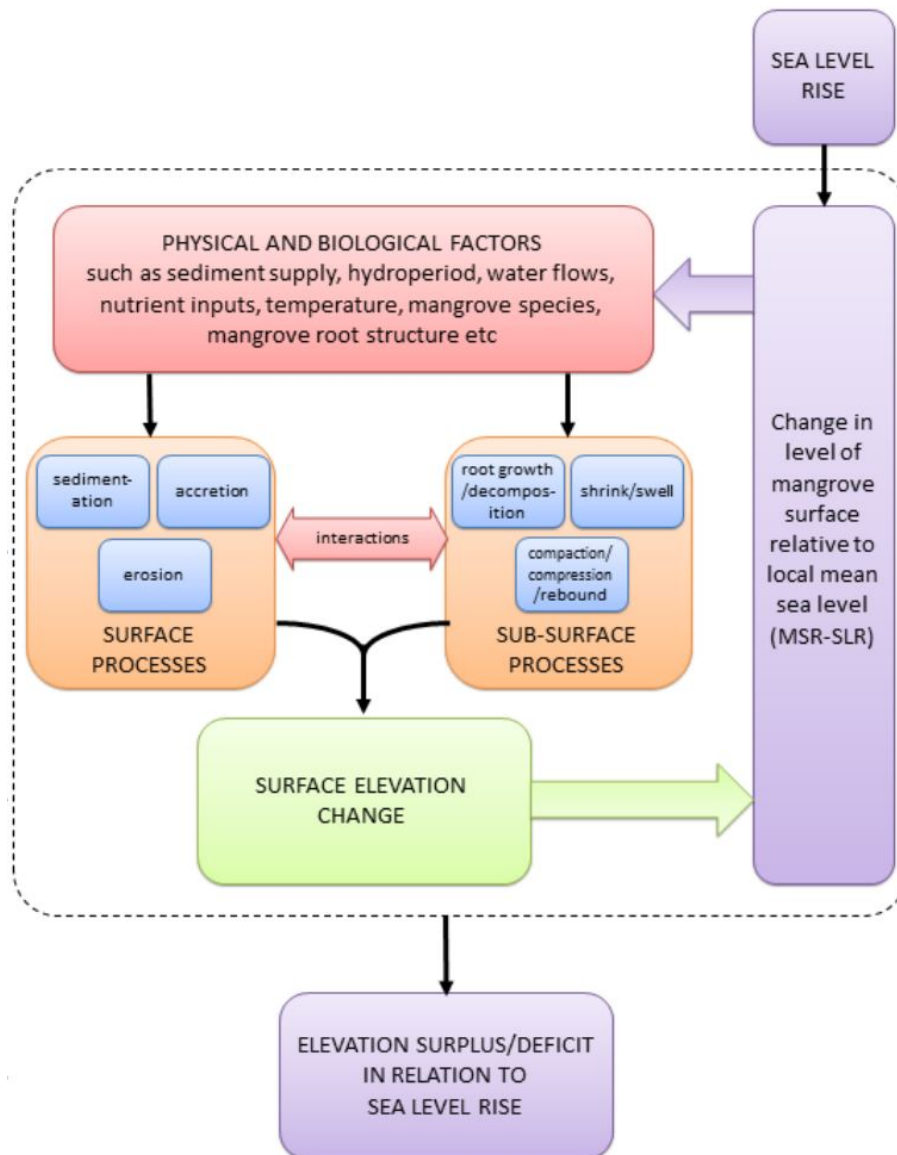


Figure 6: Environmental and biological factors influencing the surface elevation dynamics in mangroves (McIvor et al., 2013)

As mentioned before, human induced impacts are the major drivers in mangrove survival. However, [Kirwan and Megonigal \(2013\)](#) argue that interactions between rapid sea-level rise and human impacts will drive mangrove stability in the future. As stated before, **SLR** requires mangrove to increase their surface elevation vertically or laterally. However, coastal squeeze can reduce the inter-tidal area (‘room for the sea’), depleting the mangroves from the ready supply of sediments upon which their survival depends. The feedback between mudflat profile, onshore sediment transport and sedimentation room or mangrove forest width may induce a rapid decline of the wetlands ([Winterwerp et al., 2013](#)). However, definite conclusions on the behaviour and resilience of mangrove systems varying in width are to date uncertain and should be investigated ([Best et al., 2018](#)).

Also, sediment transport dynamics in estuarine systems have received considerable attention in recent years in response to increasing awareness of water quality degradation and an increase in navigational and flooding problems ([Hossain and Eyre, 2002](#)). Sediment transport in an estuary is often controlled by both periodic fortnightly tidal variation under low flows, and a-periodic floods. Under low river flows the fortnightly tidal cycle maintains a large volume of sediment in motion and may trap the sediment in the estuary through repeated cycles of deposition and erosion. During a-periodic events many estuaries can carry high suspended sediment loads, and this can drastically change a system’s morphology. Freshwater discharge, therefore, appears to be an important external physical force that controls sediment deposition and transport into estuaries and the continental shelf. However, few studies regarding sediment dynamics have been undertaken in wet and dry tropical Australian estuaries ([Hossain et al., 2001](#)). Furthermore, the different hydrological characteristics of Australian catchments, such as low rainfall and very high flood peaks relative to normal flow suggest that a detailed investigation of sediment transport dynamics is necessary ([Finlayson et al., 2013](#); [Willemsen et al., 2015](#)). This knowledge gap is also identified by [Kirwan and Megonigal \(2013\)](#), addressing the incorporation of these variations e.g. sediment availability as a key challenge for future modelling attempts of coastal wetland evolution. Such models can help addressing the consequences of variations in the river discharge and sediment supply on mangroves, which are one of the most valuable and yet most threatened ecosystems [de Groot et al. \(2012\)](#).

1.5 Research objective

Building on these previous studies, the aim of this research is to gain insight in the hydro- and sediment dynamics and consequently the morphodynamic response of two transects of different mangrove forest widths. Furthermore, this study aims to investigate the effect of different mangrove forest widths on the biophysical interactions when variations in river discharge and fluvial sediment input are considered. This is done by means of a case study of the South Ballina mangrove forest, which is evidently characterising for mangroves along the coast of **NSW** ([Akumu et al., 2011](#); [Saintilan et al., 2018](#)). In order to increase knowledge about the interactions between the individual processes in a mangrove ecosystem and the (morphological) development of such ecosystem, a field campaign is first undertaken. The objective of this field campaign is to gather quantitative data regarding the system’s biophysical properties and boundary conditions. This field campaign functions as the basis of a model study, where a numerical, process-based model (Delft-FM) will be used. This model combines a flow, vegetation and a morphology model to determine the sediment transport and morphodynamics. The objective of this model study is to use the data from the field campaign to set up representative models and to simu-

late the hydro- and sediment dynamics during normal conditions, low flow conditions and a flood event.

All the aforementioned is captured in the main research question stated below.

How does a variation in mangrove forest width influence the hydro- and morphodynamics of the South Ballina mangrove forest under normal conditions, and when variations in river discharge and fluvial sediment concentrations are considered?

In order to answer the main research question, sub-questions have been formulated in order to make the research more comprehensive and structured. These sub-questions follow the next steps: system and initial conditions, biophysical processes and possible implications of different scenarios. The sub-questions read:

1. What is the effect of mangrove width on the biophysical properties and interactions?
 - (a) What are the differences in topographic, vegetation and sediment characteristics of the two transects?
 - (b) What is the effect of these transects properties and variations on the hydro- and morphodynamics?
 - (c) What differences between the two transects can be observed regarding the biophysical interactions and how can this be linked to the difference in mangrove width?
2. What is the effect of mangrove width on the hydro- and sediment dynamics, when variations in river discharge and sediment concentration are considered?
 - (a) How are the hydro- and sediment dynamics at the two transects affected by a low river discharge with low concentrations of sediment?
 - (b) How are the hydro- and sediment dynamics at the two transects affected by a river flood event forcing an increase in river discharge and in the sediment supply?

The steps within this research are schematised in figure 7. The first part of this study consists of mapping the transect properties, the hydro- and morphodynamics and the interactions between them. In the second part, the obtained field data is used as input for the models regarding their domain, bathymetry, vegetation cover and hydrodynamic- and sediment boundary conditions. Hereafter, the model is being calibrated and validated against field data. Finally, the calibrated models are used to explore the effects of low flow conditions and a flood event.

1.6 Report outline

First, the fieldwork methodology is explained in chapter 2. This chapter starts with an description of the study area. Hereafter, the data collection methods for each investigated property is explained. This is followed by chapter 3, where the obtained data of the field campaign is presented. Chapter 4 starts with a description of the set-up of the numerical model, after which the calibration and validation, as well as the scenario set-up are described. Chapter 5 starts by presenting the calibration and validation results and choices, followed by the results of the scenario runs. In chapter 6 and 7 the discussion and conclusions of this study are depicted. This thesis ends with the recommendations for future research, as described in chapter 8.

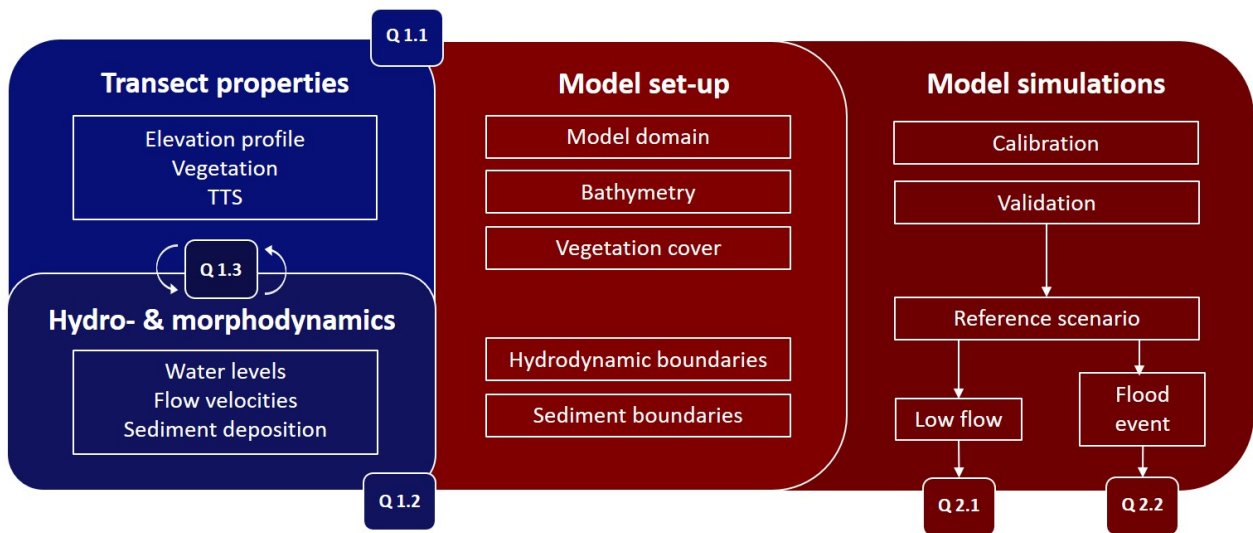


Figure 7: Flow chart of the research steps and the corresponding research questions Q.

2 Fieldwork methodology

A field campaign has been executed in order to obtain data of the hydro- and morphodynamics in a mangrove forest. This field campaign took place in Ballina in New South Wales, Australia, and took place during the months February-May 2020. Part of this field campaign has not been executed by the author, but by D. Stokes due to the COVID-19 situation. The methods and exact location of the field campaign will be described in this chapter. The methods for measuring hydrodynamic and morphodynamic variables are in this chapter depicted, including an explanation of the applied measuring equipment and other techniques.

2.1 Study area

2.1.1 Location

This study will focus on the mangrove forest located on the southern banks of the Richmond River's estuary in NSW Australia ($28^{\circ}52'32.8''S$ $153^{\circ}32'13.0''E$) (see figures 8a and 8b), this estuary directly dissects the township of Ballina. The Richmond River is a mature wave dominated, barrier lagoon estuary. It is navigable for around 12 km up its length, but the main usage is irrigation. Also some weirs have been constructed to mitigate the effects of flooding (Ryder et al., 2015). The estuary and surrounding catchment has been highly modified since the late 1800s. Rock-walls were erected to provide a navigable ocean entrance and this has altered the geomorphology of the estuary. Directly behind the southern banks are sugar cane farms, upstream of the river are grazing and macadamia farms (Ryder et al., 2015).

2.1.2 Climate

The climate of coastal northern New South Wales is classified as a humid subtropical area with a distinct summer to autumn maximum in rainfall. The regional climate is strongly influenced by the El Niño-Southern Oscillation (ENSO), which results in large interannual variability in rainfall. Mean temperatures in the lower Richmond River catchment, in the vicinity of Ballina, vary from daily maxima of 27–31 °C in January to daily minima of 6– 12 °C in July. Frosts are experienced every winter in the inland parts of the catchment, but are rare at the coast. Mean annual rainfall decreases from over 1400 mm along the coast to 1100 mm in the western parts of the coastal lowlands.

2.1.3 Hydrology, tides and sediment transport

The Richmond River is one of the largest coastal drainage systems of New South Wales, with a catchment area of circa 6900 km² and a mean annual discharge of 1.9210⁶ million m³. Around 40 kilometer upstream from the mouth, the Richmond River increasingly assumes an estuarine character in its hydrology and geomorphology. At its mouth, the Richmond River is joined by North Creek, a southward-trending estuarine tributary, before discharging to the sea. The Richmond River catchment has one of the highest rainfalls in NSW and stream flows fall within the category of 'extreme late summer'. As such, around 90 % of the annual discharge and flood events occur during the summer-autumn wet season. It is during these events that the river may completely freshen to its mouth for periods of up to a few weeks. During dry periods, saline conditions extend considerable distances



(a) Location of Ballina in New South Wales. (Google Earth, 2020)



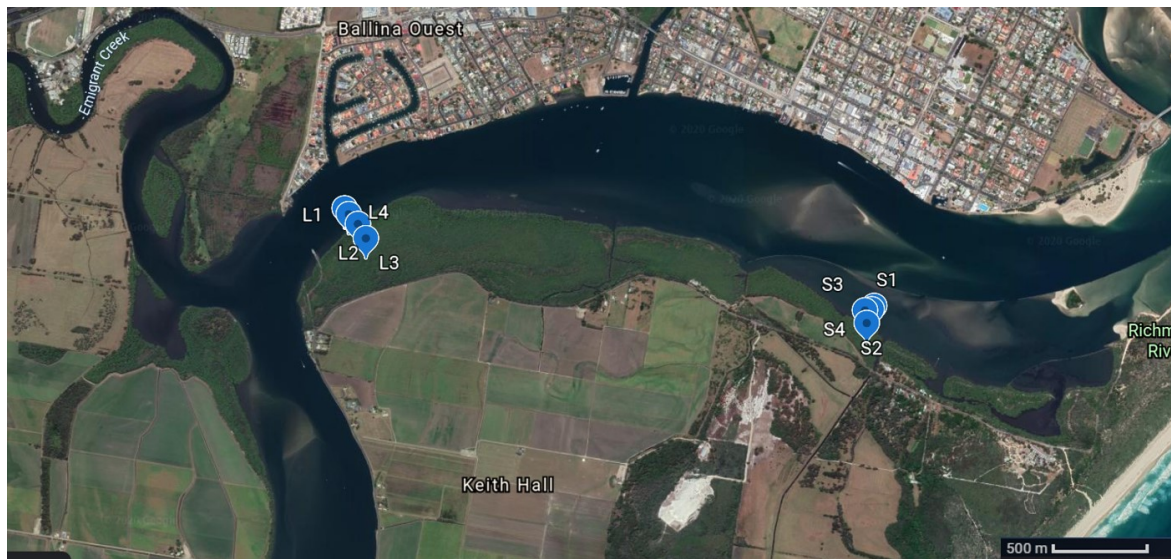
(b) Location of the study area in the Richmond River estuary, enclosed by the red square (Google Earth, 2020)

Figure 8: Location of the study area

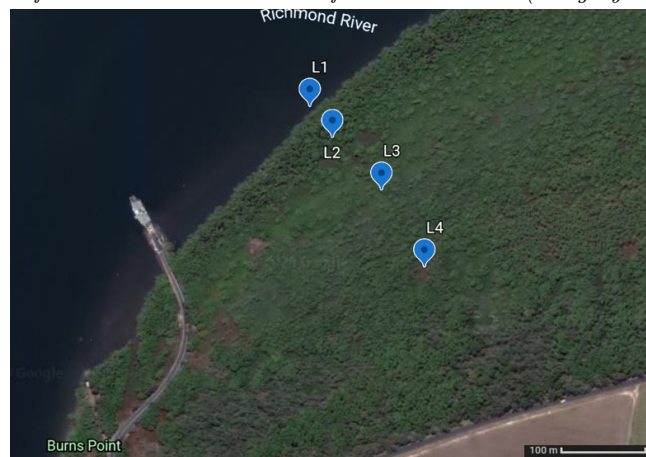
upstream, as evidenced by the occurrence of the species *Avicennia Marina* and *Aegiceras Corniculatum* at a distance of over 40 km from the river mouth. Tidal influence due to the water levels extends along most of the Richmond River low lying areas, reaching 120 km upstream of the mouth along the Wilsons tributary. The tidal range within the channel decreases rapidly with increasing upstream distance, from the open ocean range of approximately 2 m at the mouth to 0.5 – 0.8 m in the upper estuarine areas (Ryder et al., 2015; WBM Oceanics, n.d.). During normal flow conditions, there is little exchange of suspended sediment between the upper and lower estuary because of small freshwater inputs, resulting in a net marine sediment input in the lower estuary (Hossain and Eyre, 2002) due to the dominant ebb tides. The major source of suspended sediment inputs into the Richmond estuary is fluvial inputs from the upper catchment (92% - 99% of the total yearly input), with more than 90% being transported during runoff events (Hossain and Eyre, 2002).

2.1.4 Studied transects

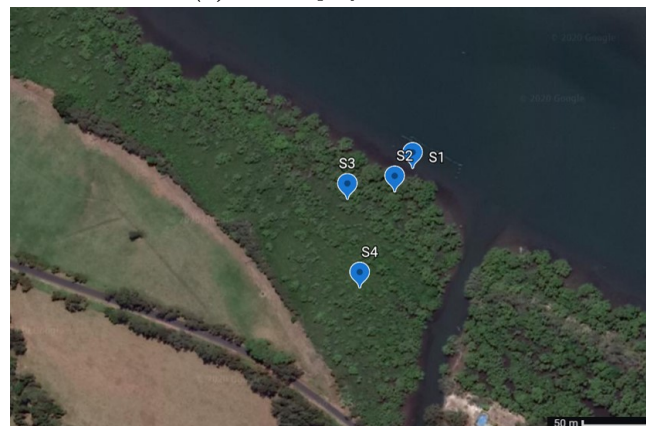
Within the study area, two transects 3km apart and perpendicular to the Richmond River are studied. The two transects are of interest due to the availability of additional data and observations. In this report, a comparison between the two transects is made, where differences in the observed biophysical interactions are analysed. Along the transects, multiple locations have been defined where measurement stations are placed. These locations have been labelled 'L1-4', located on the longer transect near the ferry (see left side of figure 9b), and 'S1-4' corresponding with the shorter transect near the creek (see right side of figure 9c). The transect containing L1-L4 will henceforth be cited as the 'L-transect', while the transect containing 'S1-4' is from now on cited as the 'S-transect'. Each marked location within the transect and its characteristics are elaborated on later in this chapter.



(a) Overview of the measurement stations for both transects (Imagery: *Google Earth*).



(b) Close up of L-transect



(c) Close up of S-transect

Figure 9: (Overview of the measurement locations of (b) the L-transect and (c) the S-transect (Imagery: *Google Earth*))

2.2 Data collection

Each subsection starts with a description of the data collection methodology, followed by the processing steps of the raw data making the data fit for further analysis and implementation.

2.2.1 Elevation profile

A field survey has been executed in order to obtain a detailed elevation profile of both transects. Due to the dense vegetation and weak GPS signal, a traditional water levelling instrument was used (Quartel et al., 2007). This instrument is a section of clear tubing, partially filled with water. The ends are held vertical, and the rest of the tubing lies on the ground or floor. The water level at each end of the tube will be at the same elevation, whether the two ends are adjacent or far apart. In case of a gradient, the result will be a height difference between the two ends. Transforming these height differences between ends over multiple measurement points results in a cumulative elevation profile with L1 and S1 as reference points. The water levelling instrument is lower-tech compared to a laser levelling instrument, but it can be more accurate over long distances. It also works without a sight-line, which makes it highly convenient for surveying irregular paths through vegetated areas. This method appeared to be very effective and is characterised by flexibility and mobility. The water hose can also be equipped with wider sections at each end, in order to make it even more accurate.

Due to the relatively large bed level slope near the fringe, the interval of the readings started at two meters near the fringe, but later increased to five meters. The readings followed the man-made path along the remaining locations up until L4 and S4. As figures 9a and 9b show, the locations S1-4 and L1-4 are not in a straight line and are therefore transposed onto a straight line. Using a linear regression script, the data points of the transect can be transposed to the transect along those lines parallel to the coastline.

2.2.2 Vegetation survey

Vegetation surveys were conducted to quantify the rigid vegetation at the study sites. The survey objective was targeted at the two types of structure that characterize this mangrove forest: (1) The trees and branches and (2) the pneumatophores. The collection of the tree count and distribution data is carried by Draper (2017). Field measurements of the mangrove forest structure were collected in June 2016, within one larger plot and five subplots in the L-transect. The protocol by Boone Kauffman and Donato (2012) was used, which implies the notation of tree height, stem diameter or Diameter at Breast Height (DBH), canopy area and percentage vegetation cover of all living trees within that plot. One large plot of 10x10m (Fringe Plot 1 (FP I)) near the fringe and five additional rounded subplots with a radius of 0.5m (Inner Plots 1-5 (IP I-V)) were marked with flagging tape. DBH measurements within each of the plots were taken at 1.3m, however for tree heights below 1.3m stem girths were measured at 5cm above the substrate. For trees that presented more than one stem, the DBH of each stem was recorded. The locations of the plots are shown in figure 10. Due to the lack of data of the S-transect, tree count are assumed to be similar with the L-transect. The distribution of the tree zones are derived using aerial photos and by indication of D.Stokes.



Figure 10: Location of the L-transect survey plots (Draper, 2017)

Field measurements regarding the pneumatophores were obtained in March of 2020 along both transects. For each location (S2-4 and L2-4) the number of pneumatophores were counted in six 25x25cm subplots. Also, ten random pneumatophores were measured for their diameter at 5cm above the substrate and their total height for each location. Counting the pneumatophore density in multiple subplots accounts for the spatial variability. All vegetation surveys have been conducted once due to the assumption that the vegetation has remained more or less constant during the study period.

2.2.3 Hydrodynamics

In order to qualitatively compare both transects and in order to accurately model the hydrodynamics in Delft-3D, information about the, tidal wave, velocities and directions of the currents is required.

Pressure gauges

Knowledge about the height of the tidal wave is obtained using two HOBO Water Level data loggers. These sensors are robust and the internal memory and battery housing facilitates autonomous data collection for periods of up to several weeks, depending on sampling frequency and battery quality. These devices measure the total pressure of the vertical column directly above the gauge. During inundation periods, this results in the pressure due to the water column and air pressure, and during dry periods the air pressure is measured. Samples were taken with a fixed interval each five minutes. Data collection by all sensors started simultaneously for every deployment, as seen in table 1. Continuous sampling is done every 5 minutes for 14 days. To start data collection at shallow water depths, the instruments were attached to a perforated tube attached to bricks, see figure 11. The sensors were levelled at 5–7 cm above the bed as can be seen in figure 11b.

After deployment, the retrieved data needs to be processed before further analysis. First, a correction for the atmospheric pressure is applied by averaging the measured pressures during 'dry' periods (e.g. not inundated). The device measures pressure in kPa , this is transformed to water depth by multiplying the pressure with 0.1 when assuming a water density of 1000 kg/m^3 and a specific gravity of 9.81 m/s^2 . Finally, the water depths are corrected for the sensor height above the bed.



(a) Close up of one pressure gauge attached to the anchors (b) Placement of the pressure gauges and conductivity sensor in the field

Figure 11: Overview of the set-up of a pressure gauge and conductivity sensor pair.

Tilt Current Meters

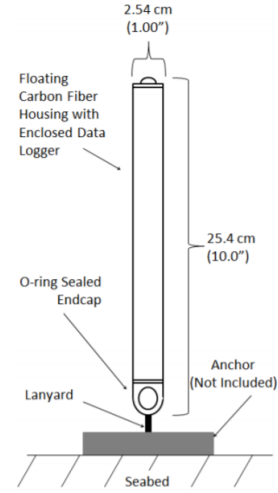
In order to measure the current velocities at the fringe and within the forest, two **TCM-4**'s were used. The **TCM** measures current using the drag-tilt principle. The logger is buoyant and is anchored to a tile via a short flexible rope. Moving water tilts the logger in the direction of flow. The **TCM** contains a 3-axis accelerometer and 3-axis magnetometer for measuring tilt and bearing. The resulting orientation data is converted to current by applying calibration coefficients which depend on the position relative to the magnetic north. This is done using the open software 'Domino' by **Lowell Instruments**. Furthermore, the instrument registers flow velocities continuously. Meaning a dry period will result in the **TCM** laying down sideways and registering a large hypothetical velocity. Only two **TCM**'s were available during the fieldwork, these were deployed during two subsequent periods at locations L1, L3, S1 and S3 during low-tide (see table 1) The **TCM**'s were deployed to sample at a 15 minutes burst interval. Data collection by all sensors started simultaneously for every deployment. The instruments with their anchors were placed on the substrate resulting in a actual sensor height of about 5–7 cm above the bed. Also, to be able to link the velocity readings with the pressure data and RSET's, the **TCM** were placed next other equipment without interfering with those readings.

Since the **TCM**'s cannot measure flow speeds when they are not fully submerged, the data needs some processing. The set-up of the **TCM** has a total height of around 30cm when submerged. Including a safety-margin as well as the anchor height gives an approximate height of 40cm. This means that measurements are affected or not credible with water depths lower than 40cm. Data points corresponding with a measured water level $< 40\text{cm}$ are therefore filtered out. After this step, the data still showed some extreme velocities which are filtered out. In order to observe the direction of the currents over time, the velocities are split into 'landward' and 'seaward' directed velocities by means of their angle. Velocities with angles larger than 210° and smaller than 30° are labelled as landward

for the S-transect. For the L-transect the landward velocity angles are larger than 135° but smaller than 315° . These angles correspond with an hypothetical line perpendicular to the fringe. Finally, a moving average of 60 minutes is imposed to smooth fluctuations.



(a) TCM with anchors as used in the field



(b) Schematic view of the TCM. Source: Lowell Instruments

Figure 12: Set-up and schematic overview of the used Lowell TCM's

Table 1: Overview of equipment deployment including observed parameters, positioning, instrument settings and deployment duration

Parameter observed	Equipment	Location	Elevation [m above local bed level]	Sampling Frequency [Hz]	Samples per burst; burst interval [s]	Deployment duration per position
Flow velocities (vx, vy, vz) [m/s]	TCM	S1, S3	0.07-0.09	2	120; 900	9 days
Flow velocities (vx, vy, vz) [m/s]	TCM	L1, L3	0.07-0.09	2	12; 900	
Temperature [C]	TCM	S1, S3	0.05-0.07	2	12; 300	9 days
Temperature [C]	TCM	L1, L3	0.05-0.07	2	12; 300	40 days
Pressure [mBar]	HOBO Water Level Data Logger	S1, S3	S1: 0.06 S3: 0.07	1/300	(continuous)	14 days
Pressure [mBar]	HOBO Water Level Data Logger	L1, L3	S1: 0.05 S3: 0.06	1/300	(continuous)	40 days
Conductivity	HOBO Salt Water Conductivity Logger	S1, S3	S1: 0.07 S3: 0.08	1/300	(continuous)	14 days
Conductivity	HOBO Salt Water Conductivity Logger	L1, L3	S1: 0.06 S3: 0.07	1/300	(continuous)	40 days

Other stations

Since the TCM's and pressure gauges only cover a small study period, additional data from calibrated stations owned by the NSW government has been requested. This data is used to filter out any influences by the Richmond River, but it also provides information about the complete tidal waves since these stations are always submerged. Information regarding the water levels calibrated against Australian Height Datum (AHD) is requested from three different stations; Byrnes Point which is located near the L-transect, Missingham Bridge which is situated near the breaker walls in the estuary,

and Brunswick Heads, a station 100km in the sea south of Ballina.

2.2.4 Total Suspended Solids

Total Suspended Solids (TSS) were sampled during four moments in a spring-neap cycle for both transects, see figure 13 and table 4. During one neap tidal cycle and one spring tidal cycle samples were taken at exact high and low tide according to NSW Government (2020). Sampling at high tide took place with a boat as close as possible to S1 and L1 at a depth of ± 30 centimetre above the bed. Location S1 was hard to reach with a boat due to wooden floaters in front of the transect. Therefore samples were taken at around the same cross-shore position as S1, but further downstream near the creek. Sampling at low tide was performed on foot, taking samples four meters further offshore than S1 and L1 at a depth of ± 15 centimetres above the bed. The analysis of these sediment samples was performed according to the APHA (2017) 2540-D method. The basic principle of this method is the filtration of a well-mixed sample through a weighed standard glass-fibre filter. The residue retained on the filter is dried to a constant weight at 103 to 105°C. The increase in weight of the filter represents the total suspended solids. This study filtered the samples with pre-weighted filters (0.45 μm Whatman GF/F), which were dried in the oven (24 h at 105°) and weighted again. Next, the filter was wetted with a small volume of reagent-grade water to seat it in the filtering apparatus. Samples were stirred to shear larger particles and obtain a homogeneous sample without leaving solids in the bottles. Beakers were used to put a measured volume of the sample onto the suction filter apparatus. This was repeated until the sample was entirely filtered. Finally, the filter is carefully removed from the apparatus and transferred to an aluminium weighing dish and placed in the oven.

After weighing the dried filters, the TSS can be determined with the following formula (APHA, 2017):

$$\text{mg total suspended solids/L} = \frac{(A - B) \cdot 1000}{\text{sample volume, mL}} \quad (2.1)$$

where:

A = weight of filter + dried residue in mg

B = weight of filter in mg

The first sampling day, three bottles of 1000 mL were taken from both transects. These sample volumes were chosen to yield between 2.5 and 200 mg dried residue. However, the first iteration took more than 10 minutes to complete, so a smaller sample size (500 mL bottle) was chosen for the following sample day (APHA, 2017). Also, the first analysis showed great similarities between the samples. Therefore the number of samples was reduced from three to two samples.

2.2.5 Sediment deposition

To determine sediment deposition patterns within a mangrove forest, multiple tools are mentioned in literature.

Tiles

Sediment deposition rates at both transects were measured using 0.04 m^2 acrylic sediment traps ,

Table 2: Sampling schedule TSS

Sampling schedule	Date & Time	Sample volume (# of samples) [mL]
<i>Neap</i>	<i>Low tide</i>	28-04-2020 05:50 500 (2)
	<i>High tide</i>	28-04-2020 11:50 500 (2)
<i>Spring</i>	<i>Low tide</i>	10-03-2020 09:37 1000 (3)
	<i>High tide</i>	10-03-2020 16:03 1000 (3)

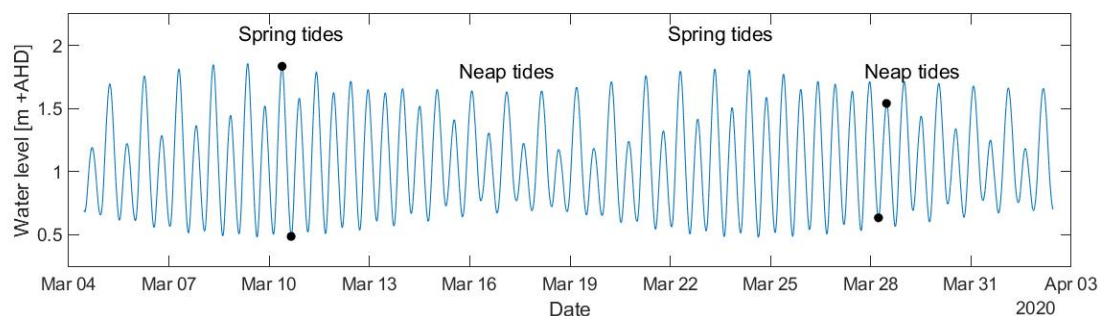


Figure 13: Visualisation of TTS sampling moments (black dots) during multiple spring-neap cycles.

with a rough side in order to mimic the natural bottom roughness in the mangrove. These traps are comparable with the traps used by [Willemssen et al. \(2016\)](#) and [Horstman et al. \(2015\)](#). The traps were placed with the smooth side facing down, in order to prevent sediments from sticking to the bottom when retrieving the tiles. These traps were installed flush with the surrounding bed and secured with wooden pins. Three replicates per location were deployed, resulting in a total of 18 tiles for the two transects. The tiles remained in the field for 48 hours, they were placed on the 10th of March and retrieved on the 12th of March during low-tides at locations S2-S4 and L2-L4. This was during a spring tide. The bottoms of the tiles were rinsed in order to remove residual sediment not originating from sedimentation. Next, the tiles were placed in zip-lock bags and transported to the laboratory. Next, the tiles soaked and cleaned with sterile water. The residue was captured in pre-weighed oven trays and oven dried at 105° until a constant dry weight was obtained. Next, the dry weight were divided by the number of days the sediment traps were submerged and the surface area of the traps in order to obtain the sedimentation rate per 24h.

RSET

To determine surface elevation patterns within a mangrove forest, multiple tools are mentioned in literature. According to [McIvor et al. \(2013\)](#), surface elevation change is standardly measured using the **RSET** method, this is also known as the Rod Surface Elevation Table Horizon. The **RSET** methodology uses a measurement of the height of the surface above a base layer underground, which is usually a layer of consolidated material that a rod or pipe is driven into until the point of refusal. This method is thus useful to determine the surface elevation change relative to the bedrock or consolidated layer. The combination of surface elevation change and accretion measurements allows the magnitude of

sub-surface change to be calculated. However, during this study the marker horizon was not available, the obtained data therefore only provides insight in the total surface elevation change. A schematic overview of the apparatus can be seen in figure 14.

In December 2015 and January 2016, three RSET's per transect have been installed at S2, S3, S4, L2, L3 and L4. Readings from this RSET have been taken mid-2016, 2018 and during the fieldwork campaign in 2020. Due to the longevity of these apparatus, the readings can provide insight in the behaviour of the change in elevation over the years. Due to small yearly variations in the readings and to be able to see a more general trend over the years, the difference between the installation in 2016 and the latest reading in 2020 are of interest. These are obtained by converting the observed differences to mm/yr .

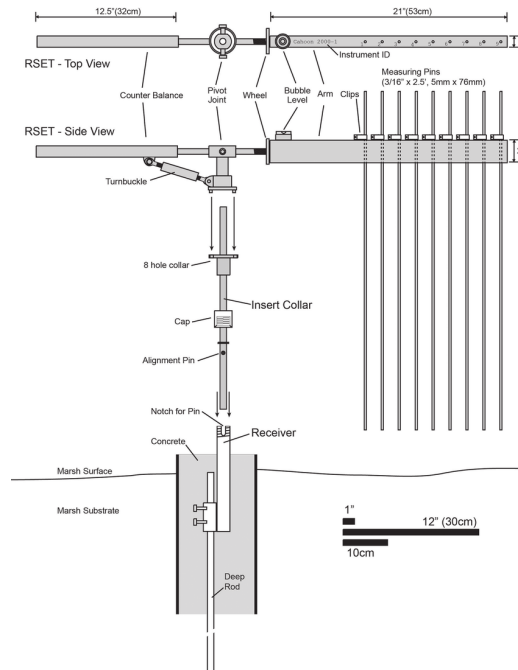
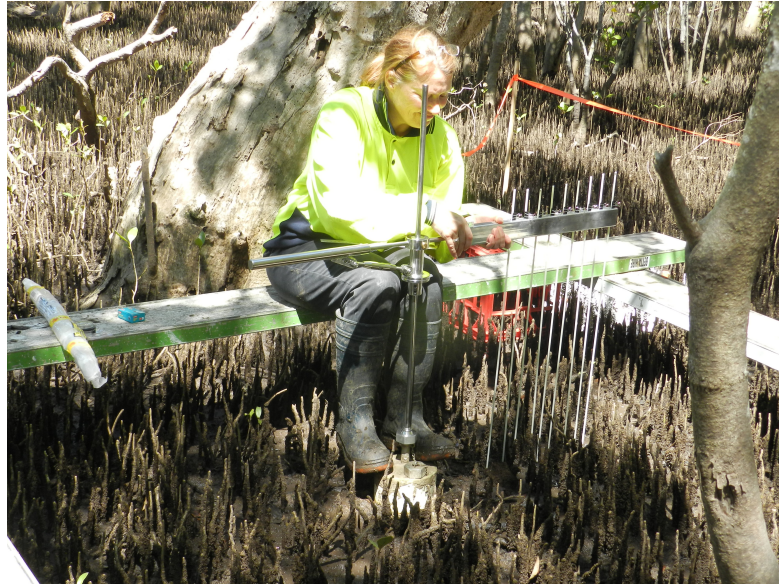


Figure 14: The RSET apparatus, shown schematically (Callaway et al., 2015)

2.2.6 Sediment characteristics

In addition, sediment characteristics were analysed for samples from the mobile top layer (<20 mm) at L2-L4 and S2-S4. Three undisturbed samples were retrieved from each location. Samples were freeze-dried and sieved over a 1 mm-sieve. The particle size is determined by laser diffraction (Malvern Mastersizer), which is applicable for sediment in the range 0.02 - 2000 μm .



(a)



(b)

Figure 15: (a) Set-up of the RSET in the field including sampling platforms and boardwalk (b) Close up of the RSET and measuring pins in order to map the height differences.

3 Fieldwork results

This section presents the observed dynamics in the South Ballina mangrove system at the L- and S-transects. This section elaborates on the the elevation profiles, the vegetation survey, the hydrodynamic results, the TSS and the sediment deposition results.

3.1 Elevation profile

Elevation data of the study area has been obtained as described in section 2. The resulting elevation profiles are shown in figures 16 and 17. These figures also show the instrument positions as well as the different vegetation zones. The cross-shore distance has been set relative to the pneumatophore fringe. The elevation has been calibrated against measured water levels at Byrnes Point and S1 and L1.

S4 was unable to be reached during the elevation survey. The L-transect showed little increase in elevation in cross-shore distance after L3. Therefore, linear extrapolation is used to obtain the cross-shore profile after S3. The S-transect profile shows a more or less smooth line starting at the mudflat and ending at the back of the forest at S4. However, there is a small bump to be seen between S1 and S2. This bump corresponds with the height of the high tide water levels during spring tides (figure 20). The relative small increase in elevation between S2 and S3 results in a justifiable extrapolation of the profile between S3 and S4. The difference in elevation between S1 and S3 is around 0.88 cm. When combining figures 20 and 16, it can also be seen that S4 gets inundated during peak spring tides. This aspect is further discussed in section 3.5.

The L-transect profile shows relatively more variance compared to the S-transect profile. two small bumps between L1 and S3 can be seen in the profile in figure 17. These bumps are due to local variations in bed level. The difference in elevation between L1 and L3 is around 1.4 meter. From this figure it can be seen that L3 barely inundates, since only the highest high water levels are likely to reach this station. Figure 17 also shows the cross-shore positions of the Fringe Plot (FP I) and Inner Plots (IP I-V), where the tree characteristics have been mapped.

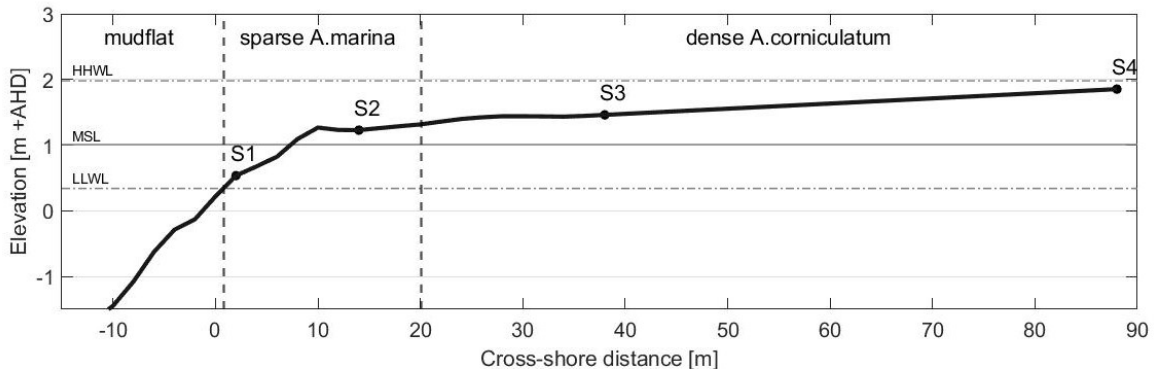


Figure 16: Elevation profile with respect to AHD of the S-transect, including instrument positions. Vegetation zones along the transect are demarcated by dashed lines. Characteristic tidal water levels are indicated near the left axis (HHWL = highest high water level; MSL = Mean Sea Level; LLWL = lowest low water level)

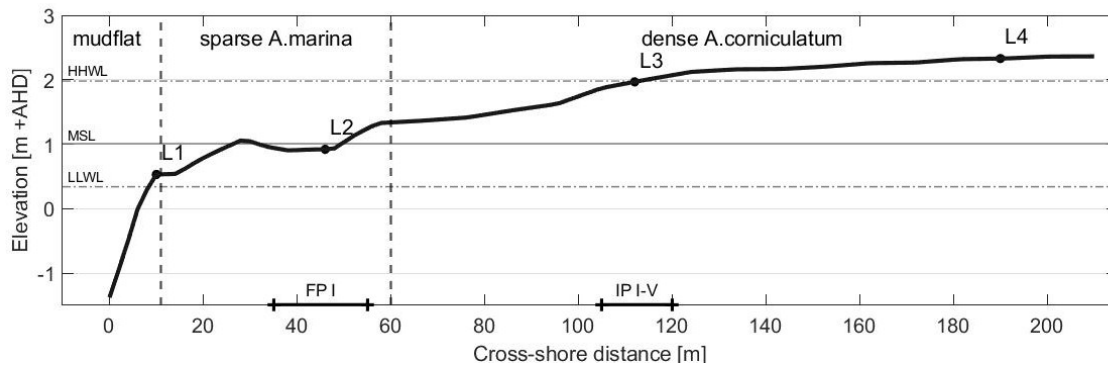


Figure 17: Elevation profile with respect to AHD of the L-transect, including instrument positions. Vegetation zones along the transect are demarcated by dashed lines. The locations of the vegetation survey plots are located at the bottom of the graph (Fringe Plot I; Inner Plot I-V). Characteristic tidal water levels are indicated near the left axis (HHWL = highest high water level; MSL = Mean Sea Level; LLWL = lowest low water level)

3.2 Vegetation survey

3.2.1 Trees and distribution

Three species have been identified at the L-transect by Draper (2017), e.g. *Avicennia marina*, *Aegiceras corniculatum* and *B.gymnorhiza*. *A.marina* was the most dominant species within the seaward fringe area with a few scattered young *B.gymnorhiza*, *A.corniculatum* is inland the dominant species alongside few scattered *A.marina*, see figure 18. A similar spatial distribution was also found for tree height and DBH, as the largest amounts of *Avicennia marina* were found near the fringe (see figure 18). This implies that the most mature trees are positioned near the seaward fringe, dominated by *A.marina*. In the inner plots however, small isolated *A.marina* were found amongst dense *A.corniculatum* shrubs. Due to the absence of tree data at the S-transect, tree characteristics as shown in table 3 are assumed to be similar for both transects. The vegetation zones have been determined on advice of D. Stokes and Google Earth imagery. The zones are further elaborated later in this chapter and shown in figures 19, 16 and 17.

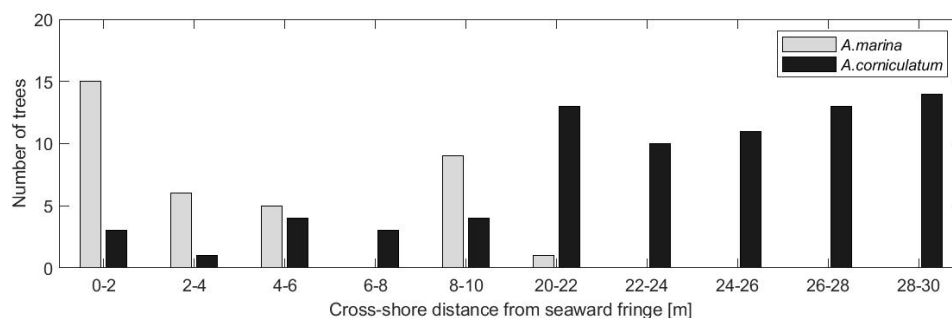


Figure 18: Tree count and species distribution with distance from the seaward fringe at the L-transect (after work by Draper (2017))



Figure 19: Location of the two different vegetation zones per transect

3.2.2 Pneumatophores

In order to gain insight in the characteristics of pneumatophores, the density of these roots was determined. Additionally, ten roots per location were measured for their height and diameter 5cm above the bed, the results of which are shown in table 3. Dense finger-like pneumatophores were found near the fringe (S2 and L2). With a density of 544 and 496 pneumatophores per m^2 , these sites almost have twice as much pneumatophores compared to S3, S4, L3 and L4. L2 has by far the tallest pneumatophores, while at the S-transect the tallest pneumatophores are found at the back of the forest near S4. The middle sample locations L3 and S3 are quite similar in results (9.3 and 9.7 cm), and contain the shortest root structures. The average diameter appears to be quite constant between all sites.

Table 3: Average tree and pneumatophore characteristics for all locations.

Location	Height [cm]	Diameter DBH [cm]	Diameter 5cm above bed [cm]	Total count (n)	Density [n/m^2]
<i>Trees</i>					
S2	446.2	5.1	-	-	0.5
S3	294.8	3.3	-	-	16
S4	294.8	3.3	-	-	16
L2	446.2	5.1	-	-	0.5
L3	294.8	3.3	-	-	16
L4	294.8	3.3	-	-	16
<i>Pneumatophores</i>					
S2	11.9	-	0.7	34	544
S3	9.3	-	0.9	14	224
S4	12.7	-	0.9	14	224
L2	15.2	-	0.8	31	496
L3	9.7	-	0.6	20	308
L4	10.9	-	0.6	14	224

3.3 Hydrodynamics

The results for the water levels, current velocities and current orientations are elaborated in this section.

3.3.1 Water levels

The water levels are measured at two different measurement locations, and calculated with the data collected by the pressure gauges. The pressure gauges have been placed at the forest fringe (L1 and S1) and halfway the transect, near L3 and S3.

Short transect

The absolute water levels at S1 and S3 are shown in figure 20. The tidal wave can be classified as a 'mixed semi-diurnal tide', meaning that there are two high tides and two low tides per day, but the heights of each consecutive tide differ; the two high tides are of different heights, as are the two low tides. The tidal amplitude at S1 during spring tides is no more than 1.4 meters, this is likely to be higher in reality since the minimum water level at spring tide is not known. During neap tide the amplitude is around 0.7m. It can be noticed that S3 hardly inundates during the period of deployment. 'Only' seven peaks in water level are observed, mainly referring to the spring tides. This implies that water levels during neap tide are not high enough to reach the inland locations. The end of the deployment period shows a constant inundation for both S1 and S3. This can either be due to the tidal components, or due to an increase in river discharge which was also observed during the field campaign, resulting in a constant higher water level. Another explanation could be the fluctuations in atmospheric pressure. Since only the average atmospheric pressure is subtracted, fluctuations with increasing pressures are not accounted for. The difference in water depth during inundation periods between S1 and S3 is around 85cm. With the assumption that there is no phase difference in the tidal wave entering the mangrove forest, the elevation difference between S1 and S3 also comes down to 85cm. This implies a good accuracy of the elevation survey for the S-transect, since the observed elevation difference by the survey came down to 0.88 cm.

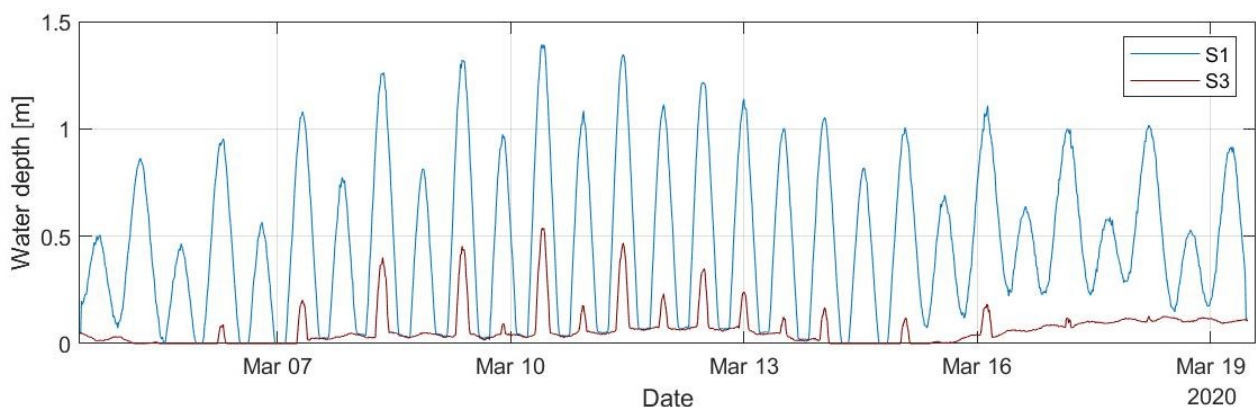


Figure 20: Water level at the S-transect measured between 4 and 19 of March. The blue line indicates S1, red is the station at S3.

Long transect

The period of deployment at L1 and L3 are significant longer compared to S1 and S3, namely between the 19th of March and 28th of April. This covers around one entire spring-neap cycle. The blue line in figure 21 shows the absolute water depth at L1, and the red line corresponds with L3. The tidal amplitudes during spring and neap tides are in line with the short transect. One important aspect that can be seen in figure 21 is the fact that L3 hardly inundates. The measured water level fluctuates around $\pm 10\text{cm}$, and shows almost no significant peaks. This means that the relative elevation between L1 and L3 cannot be accurately derived. The shown water depths at L3 could again be due to fluctuations in atmospheric pressure.

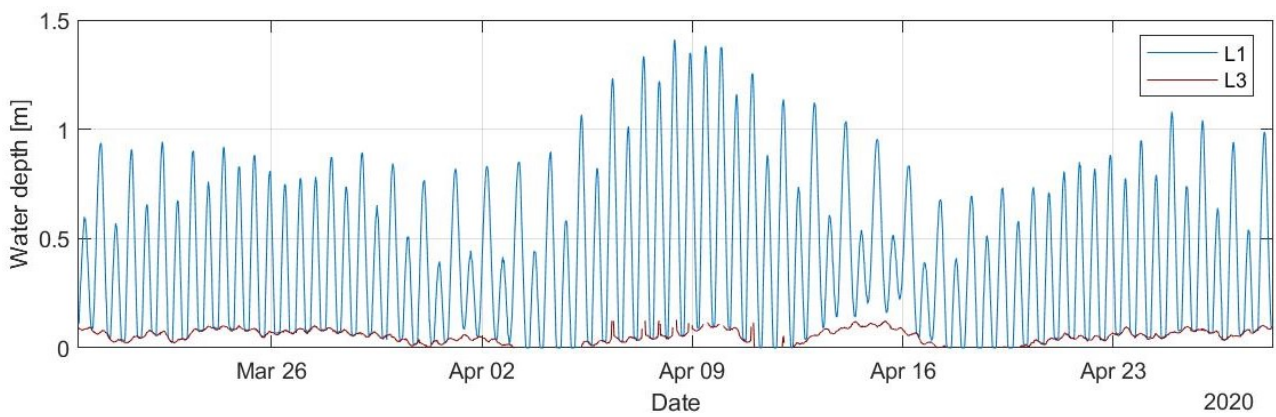


Figure 21: Water level at L1 measured between 19 of March and 28 of April. The blue line indicates L1, red is the station at L3.

3.3.2 Flow characteristics

This section elaborates the results of the TCM's after the data processing as described in chapter 2.

Short transect

Two TCM's were deployed at S1 and S3 between the 10th and 20th of March. Data points corresponding with a water level lower than 0.4m and extremes have been removed from the dataset. With the prerequisite that the TCM's only function properly when they are submerged at a water depth of 0.4m, it can be concluded that the data coming from S3 is not usable. Figure 21 shows that there are only three small windows during the sampling period where the water depth exceeds 0.4m. Flow velocity results from S3 are therefore not included in this analysis.

The result of the data processing for S1 is shown in 22, where the red dots are data points, and the orange line represents the 60-minute-moving average. Figure 23 shows two close ups of the flow velocities during spring and neap tides in combination with the measured water level. Velocities are mostly within the range of 0 - 15 cm/s, and are usually larger at the beginning of the inundation period. After the flood tides, the velocity becomes negative and seaward directed. There are however some exceptions, as seen in the bottom plot of figure 23. During neap tides, consecutive high and low

peak water levels are observed. During the relatively lower water levels, the velocity profile is shaped differently. These profiles are characterised by weak inflow compared to the outflow which results in no pronounced slack tide. The occurrence of this flow characteristic is due to the combination of a high river discharge and weak tidal back-push.

The direction of flow during spring and neap tides at S1 are visualised in figure 24, where the black line indicates the position of the shoreline. Both figures show the dominant flow direction being west-south-west, which corresponds with the rising tide since its directed upstream and into the forest. The second dominant flow direction is east-south-east which is about parallel with the shoreline. Since the direction of flow is directed towards the mouth of the river, this direction corresponds with the ebb-tide. The flow directions and magnitude correspond with the observation made that the velocities during rising tide are generally larger. The effect of the weak tidal back-push as discussed in the paragraph above, is observed in the left plot of figure 23. The maximum flow velocities are lower compared to the spring tide currents, also a more pronounced (weak) inflow in the southern direction is observed.

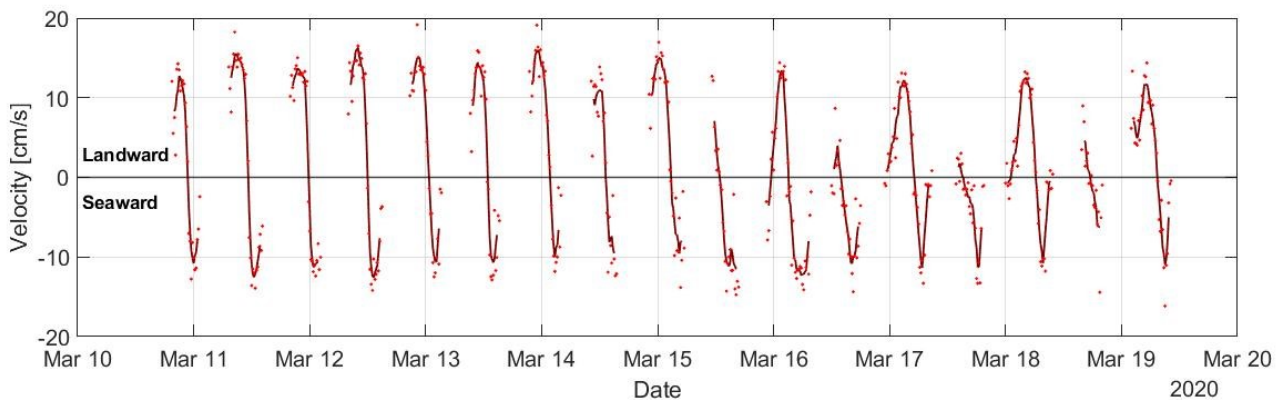


Figure 22: Measured flow velocities S1. Red dots indicate the data points, the orange line is the moving average of these data points.

Long transect

Two TCM's were deployed at L1 and L3 between the 19th of march and the 28th of April. The preparation of the TCM data followed the same methodology as described in chapter 2 and the section above. L3 is also subject to low water levels during the sampling period, as seen in 21. The dataset from L3 is therefore also discarded and not included in further analysis.

Figure 25 show the collected data points in red dots, with a moving average of 60 minutes shown with a orange line. A close up of the flow velocities during spring and neap tides are shown in figure 26 along with the water levels at the same moment. Flow velocities during spring tides are generally between the 2 and 20 cm/s. Remarkably, the ebb currents appear to be generally larger compared to the currents induced by the rising tide. This is also acknowledged by the left plot of figure 27, where the direction and magnitude of the flow over the same period are visualised. This plot shows that the out-flowing velocities, which are directed east-north-east, are generally larger compared to the in-flowing

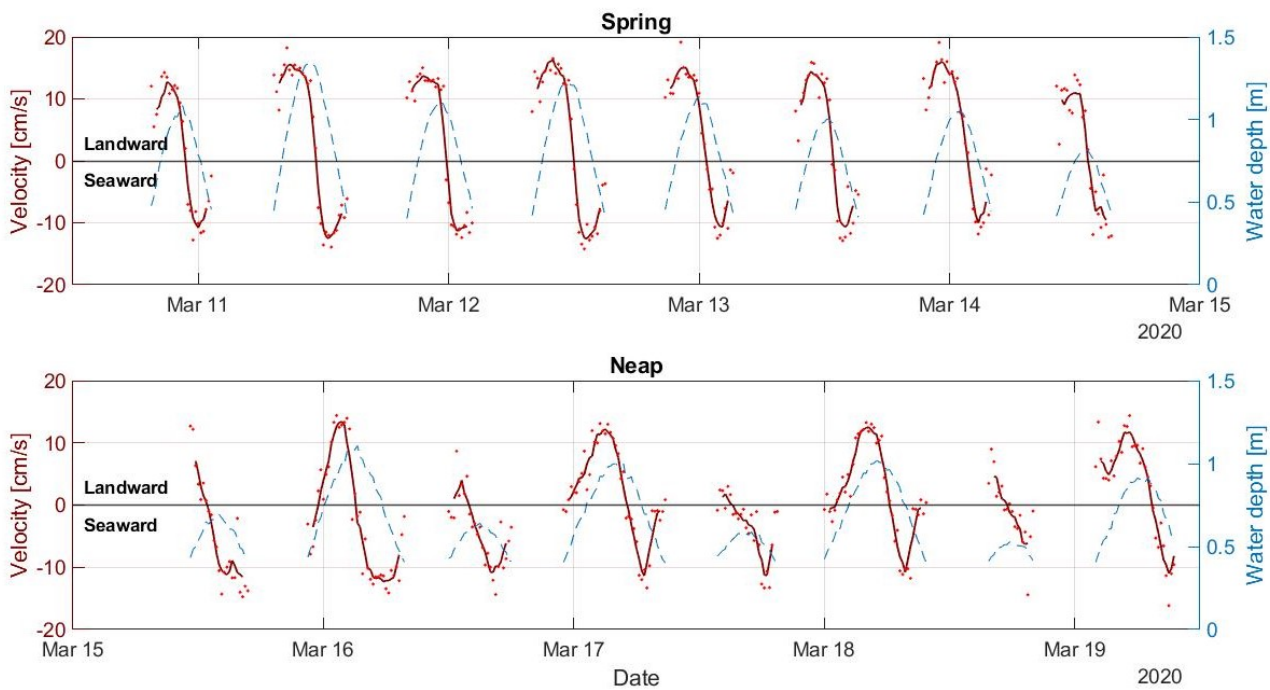


Figure 23: Close up of the flow velocities $S1$ during spring (top) and neap (bottom) tides. Red dots indicate the data points, the orange line is the moving average of these data points. The dashed blue line is the observed water level.

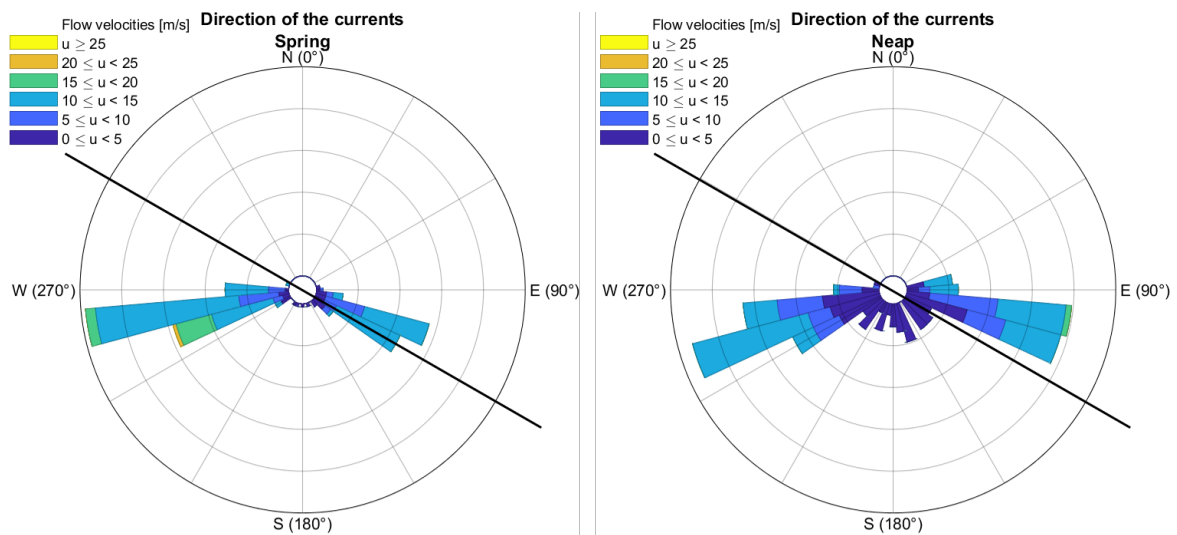


Figure 24: Direction of flow during spring tides (left) and neap tides (right) at $S1$ in cm/s . The black line indicates the relative position of the forest fringe. Inner circles represent the degree of occurrence.

velocities, which are directed south-west. The observations at neap tides differ substantially compared to the observations during spring tides. The bottom plot of figure 26 shows a constant outflow. The weak inflow during neap tides is also shown in the right hand plot of figure 27, where it appears that the majority of the flow is directed seawards. An explanation for this is that the river discharge is in the same direction as the ebb-tide, resulting in a increased tidal outflow. The combination of weak tidal back-push and high river discharges is more pronounced compared to the S-transect, and can be attributed to the relative location within the estuary.

Both transect show similarities in flow characteristics during spring tides. The order of magnitude of the flow show good resemblance, the flood tides are on the other hand more pronounced near S1. Also, the inflow at S1 is directed more land inward compared to L1. Differences during neap tides between the two transects are very noticeable. Neap tides are alternately pushed back by the river at S1, while at L1 the flood tides are pushed back constantly resulting in a weak inflow.

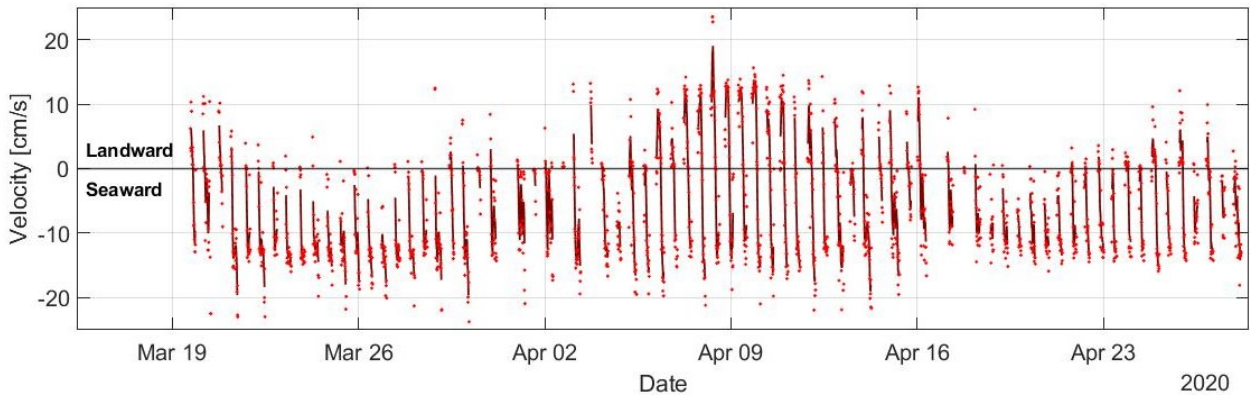


Figure 25: Flow velocities L1. Red dots indicate the data points, the orange line is the moving average of these data points.

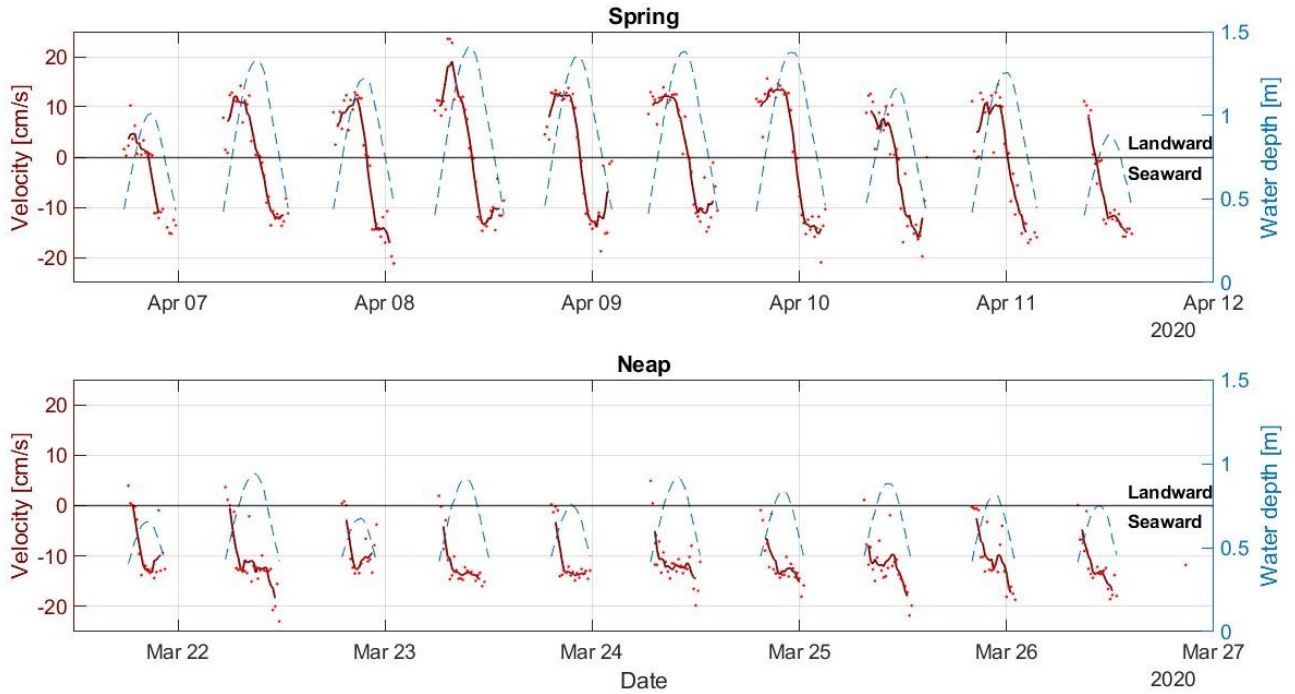


Figure 26: Close up of the flow velocities L1. Red dots indicate the data points, the orange line is the moving average of these data points. The dashed blue line is the observed water level.

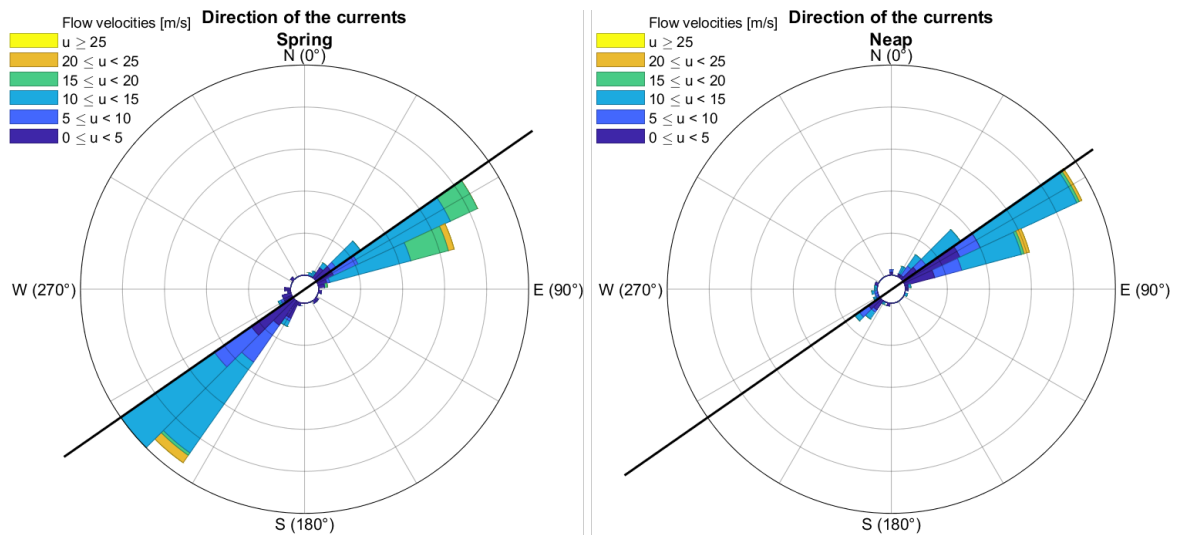


Figure 27: Direction of flow during spring tides (left) and neap tides (right) at L1 in cm/s. The black line indicates THE relative position of the forest fringe. Inner circles represent the degree of occurrence.

3.4 Total suspended solids

In order to assess the amount of sediment available for sedimentation, the TSS concentrations were measured at each site. Figure 28 shows the results of the sampling, and table 4 shows the mean \pm standard error of the observations. A few observations can be made based on these results. First, the TSS tend to be larger near the L-transect in comparison to the S-transect. This holds for both the spring and neap tide measurements, while the difference is larger during spring tide. Also, an interesting observation can be made about the high and low tide TSS. In mangrove systems is the TSS usually larger during high tide compared to low tide due to resuspension of sediments. However, these field observations show a larger TSS during low tide compared to high tide. The reason for these two observed differences is likely due to the fact that this system is characterised by fluvial sediment inputs. Alongshore sediment transport does not find its way into the estuary due to the breaker walls erected by the river mouth. This results in a tidal wave with low TSS entering the estuary. In addition, the L-transect is positioned more upstream in the estuary. The tidal wave entering the estuary will thus have a smaller influence on the TSS characteristics compared to the S-transect.

Second, the difference in TSS during one idal cycle (12h) is relatively large at the L-transect during spring tide (around 41 mg/L). The difference at the S-transect is at the same moment around 26.6 mg/L. Differences between high and low tide in a neap cycle for the L- and S-transect are respectively 5.0 and 3.8 mg/L. As figure 13 shows, the difference in water levels during spring tide, are significantly larger than the differences in water levels during neap tide.

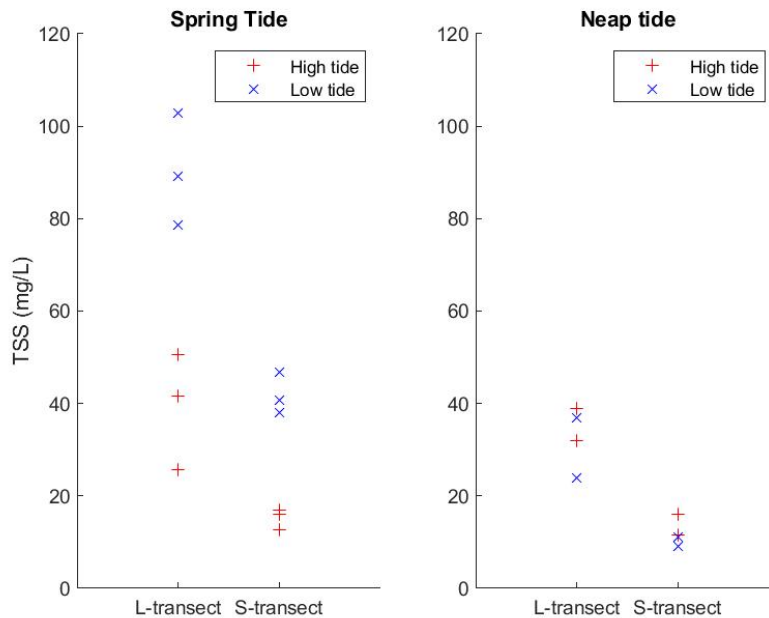


Figure 28: Total suspended solids (TSS) (mg L^{-1}) at both sites, during high- and low-tide in the spring-neap cycle. Each '+' represents one measurement

Table 4: Averaged Total suspended solids (TSS) [$mg L^{-1}$] at both sites, during high- and low-tide in the spring-neap cycle.

		Total suspended solids (standard error) [$mg L^{-1}$]	
		L-transect	S-transect
Spring	<i>High-tide</i>	39.2 (1.3)	15.2 (7.2)
	<i>Low-tide</i>	90.2 (7.0)	41.8 (2.6)
Neap	<i>High-tide</i>	35.5 (3.5)	13.8 (2.3)
	<i>Low-tide</i>	30.5 (6.5)	10.0 (1.0)

3.5 Sediment deposition

Sediment trap yields were analysed for one time interval: 10-12 March, covering 4 tidal cycles. The observed sediment deposition showed a cross-shore decrease into the mangroves, comparable to the gradient in water levels, with the largest deposition observed at both transects near the fringe, i.e. $4.6 \cdot 10^{-2} kg m^{-2}$ (see table 5). For the L-transect, this is an order of magnitude larger than the deposition rates observed at the back of the mangroves. The deposition rates at the S-transect are of the same order of magnitude compared to the L-transect. The standard error showed similarity for all locations, with the fringing locations having the largest standard error. This is possibly due to the larger variability in elevation near the fringe compared to the more inland locations. This spatial variability is due to the formation of flow channels during in- and out-flowing tides. This results in local variations in erosion or deposition, which explains the relatively larger variation between tiles near the fringe in comparison to the back of the mangrove. Converting the deposition rates in $kg m^{-2} day^{-1}$ to $mm yr^{-1}$ gives an sedimentation rate of $6.4 mm yr^{-1}$ for L2 and S2, and a rate of 3.7 and 1.1 for S3 and L3 respectively.

The sediment characteristics per location are also shown in table 5. The mean grain size of the L-transect is generally speaking a factor ten smaller compared to the S-transect. The S-transect is characterised by a cross-shore increase in mean grain size. L2 and L3 show similar results, but towards L4 there is again a cross-shore increase observed. The difference in mean grain size between both transects is related to their position in the estuary and due to the hydraulic radius of the river. The L-transect is situated in the inner bend of the river, where mostly fine sediments are transported. The S-transect is on the other hand located in the outer bend of the river, where coincidentally coarser sediments are transported. The hydraulic radius is at the S-transect significantly larger, which in turn decreases the flow velocity and allows finer sediments to settle.

Table 5: Observed averaged sediment deposition rates and characteristic sediment properties at each of the monitoring locations

Location	Deposition (standard error) [mm/day]	Mean grain size D_{50} [μm]	Silt/clay fraction, $<63 \mu m$ [%]
L2	$1.7 \cdot 10^{-2}$ ($3.3 \cdot 10^{-3}$)	$3.7 \cdot 10^1$	67.3
L3	$0.3 \cdot 10^{-2}$ ($0.4 \cdot 10^{-3}$)	$3.4 \cdot 10^1$	72.4
L4	$0.2 \cdot 10^{-2}$ ($0.6 \cdot 10^{-3}$)	$4.5 \cdot 10^1$	65.3
S2	$1.8 \cdot 10^{-2}$ ($4.7 \cdot 10^{-3}$)	$1.4 \cdot 10^2$	29.2
S3	$1.0 \cdot 10^{-2}$ ($2.7 \cdot 10^{-3}$)	$2.0 \cdot 10^2$	12.5
S4	$0.3 \cdot 10^{-2}$ ($1.3 \cdot 10^{-3}$)	$3.9 \cdot 10^2$	64.4

Table 6 shows the average change of the surface elevation in $mm yr^{-1}$ for each location as determined with the RSET's between 2016 and 2020. Multiple readings took place within this period, by averaging the sample points, a long-term trend can be observed. The table shows results, which are somewhat in line with the deposition samples of the tiles. The observed elevation change showed again a cross-shore decrease into the mangroves, comparable to the gradient in water levels, with the largest elevation change observed near the fringe (S2 & L2), where an increase in elevation of 1.1 and 1.3 $mm yr^{-1}$ has taken place. S3 and L3 show a significant lower increase in surface elevation, while L4's surface elevation appears to be decreasing since 2016. During the fieldwork period, results could not be obtained from S4. Also, S4 contains very few historical data samples so it is therefore not included in the results.

Table 6: Observed average elevation change in mm/yr between 2016-2020.

	S2	S3	S4	L2	L3	L4
Elevation change RSET's [mm/yr]	+1.1	+0.4	n.a.	+1.3	+0.6	-0.3

4 Model methodology

This chapter describes the methodology of the numerical simulation of the dynamics observed in the field. First a brief overview of the functioning of the numerical model and its controlling formula's and parameters are explained. Second, the set-up of the models regarding the model domain, vegetation, hydrodynamics and sediment dynamics are elaborated on. Next the calibration methodology as well as the model run scenarios are explained.

4.1 Model description

Similar to previous studies modelling the development of mangroves and salt marshes (e.g. [Temmerman et al. \(2005\)](#); [Willemsen et al. \(2016\)](#)), this study used a Delft-3D Flexible Mesh (DFM) model to describe and analyse the hydrodynamics, sediment transport and morphodynamics. The DFM modelling package combines a flow model, a wave model and a vegetation model in order to determine the sediment transport and the morphodynamics. The system of equations consists of the horizontal momentum equations, the continuity equation, the sediment transport equation, and a turbulence closure ([Lesser et al., 2004](#))

4.1.1 Hydrodynamics

Delft-FM describes the hydrodynamics determined in the D-Flow FM module, and are based on the unsteady shallow-water equations in (depth-averaged) 2D or 3D. For every time step, D-Flow FM calculates the water depth, flow velocities and direction, turbulence characteristics and the bed shear stress, by solving the depth-averaged unsteady shallow water equations:

$$\frac{\delta h}{\delta t} + \frac{\delta hu}{\delta x} + \frac{\delta hv}{\delta y} = Q \quad (4.1)$$

With u and v being the depth averaged velocities [m/s]. Q represents the contributions per unit area due to a source or sink term [m^3/s]. The momentum equations in x - and y -direction are given by

$$\frac{\delta u}{\delta t} + u \frac{\delta u}{\delta x} + v \frac{\delta u}{\delta y} - fu = -\frac{1}{\rho_0} P_x - \frac{gu\sqrt{u^2 + v^2}}{C_{2D}^2 h} + F_x + F_{sx} + M_x \quad (4.2)$$

$$\frac{\delta v}{\delta t} + u \frac{\delta v}{\delta x} + v \frac{\delta v}{\delta y} - fv = -\frac{1}{\rho_0} P_y - \frac{gv\sqrt{u^2 + v^2}}{C_{2D}^2 h} + F_y + F_{sy} + M_y \quad (4.3)$$

Where f is the Coriolis force, which is a function of the geographical latitude ϕ and the angular speed of the rotation of the earth Ω . ρ_0 is the density of water [kg/m^3] and g the gravitational constant [m^3/s^{-2}]. Variations in density are neglected in these formula's, except in the baroclinic pressure terms $\frac{\delta P}{\delta x}$ and $\frac{\delta P}{\delta y}$. F_x and F_y are Reynolds stresses, F_{sx} F_{sy} are stresses due to secondary flow, M_x and M_y are forces due to external sources and finally C_{2D} is the roughness coefficient.

For 2D depth-averaged flow the bed shear-stress at the bed induced by a turbulent flow is assumed to be given by a quadratic friction law [Deltares \(2020a\)](#):

$$\tau_b = \frac{\rho_0 g U |U|}{C_{2D}^2} \quad (4.4)$$

Where $|U|$ is the magnitude of the depth-averaged horizontal velocity and C_{2D} is the Chézy coefficient. This coefficient is expressed by the Gauckler-Manning-Strickler formulation $C = \sqrt[6]{h/n}$. The hydraulic radius R is typically equivalent to the water depth H in 2D.

4.1.2 Morphodynamics

The three dimensional suspended sediment dynamics is determined in Delft3D by solving the three dimensional advection-diffusion equation for sediments:

$$\frac{\delta c^l}{\delta t} + \frac{\delta u c^l}{\delta x} + \frac{\delta v c^l}{\delta z} + \frac{\delta(w - w_s^l) c^l}{\delta y} - \frac{\delta}{\delta x} \left(\varepsilon_{s,x}^l \frac{\delta c^l}{\delta x} \right) - \frac{\delta}{\delta y} \left(\varepsilon_{s,y}^l \frac{\delta c^l}{\delta y} \right) - \frac{\delta}{\delta z} \left(\varepsilon_{s,z}^l \frac{\delta c^l}{\delta z} \right) = 0 \quad (4.5)$$

Where:

- $c^{(l)}$ = mass concentration of sediment fraction [kg/m^3]
- u, v, w = flow velocity components [m/s]
- ε = eddy diffusivities of sediment fraction [m^2/s]
- w_s^l = (hindered) sediment settling velocity of sediment fraction [m/s]

The settling velocity is defined as:

$$w_s^l = \left(1 - \frac{c_s^{tot}}{C_{soil}}\right)^5 w_{s,0}^l \quad (4.6)$$

In which C_{soil} is the reference density [mg/l], $w_{s,0}^l$ is the sediment fraction specific settling velocity [m/s] and c_s^{tot} the sediment mass concentration [mg/l]. Sedimentation and erosion of mud are calculated by the Partheniades-Krone formulations (Deltares, 2020b):

$$E^{(l)} = M^{(l)} S_{(\tau_{cw}, \tau_{cr,e}^{(l)})} \quad (4.7)$$

$$D^{(l)} = w_s^{(l)} c_b^l S_{(\tau_{cw}, \tau_{cr,d}^{(l)})} \quad (4.8)$$

$$c_b^{(l)} = c^{(l)} \left(z = \frac{\Delta z_b}{2}, t \right) \quad (4.9)$$

Where $E^{(l)}$ is the erosion flux [$kgm^{-2}s^{-1}$], $M^{(l)}$ the user-defined erosion parameter [$kgm^{-2}s^{-1}$], $S_{(\tau_{cw}, \tau_{cr,e}^{(l)})}$ and $S_{(\tau_{cw}, \tau_{cr,d}^{(l)})}$ the erosion and deposition step functions, $D^{(l)}$ the deposition flux [$kgm^{-2}s^{-1}$], $w_s^{(l)}$ the fall velocity (hindered) [m/s] and $c_b^{(l)}$ the average sediment concentration near the bottom [mg/l].

4.1.3 Vegetation

In order to accurately represent the vegetation exerted shear stresses, Delft-FM allows the user to define vegetation characteristics for different areas within the model. Delft-FM then uses the formula of [Baptist \(2005\)](#) to calculate the exerted shear stresses, which is based on the concept that vegetation can be modelled as rigid cylinders characterised by height h_v , density n and drag coefficient C_D . Combined with the alluvial bed roughness C_b , these four input parameters are converted by Delft-FM into a representative bed roughness at every time-step ([Deltares, 2020a](#)). The drawback of this method is that they parameterise the flow resistance by means of the bed roughness. Consequently, the presence of vegetation will lead to a higher bed roughness and thus to a higher bed shear stress and larger sediment transport rates in case of morphological computations. To account for this, a $-\frac{\lambda}{2}u^2$ term has been included in the momentum equations where λ represents the flow resistance of the vegetation. [Baptist \(2005\)](#) considers two cases; submerged and non-submerged vegetation. In the case of non-submerged vegetation $h < h_v$ the flow resistance and bed roughness C are strictly separated :

$$C = C_b \quad \text{and} \quad \lambda = C_D n \quad (4.10)$$

In case of submerged vegetation $h > h_v$ the two terms can't be split in an equally clean manner. However, [Baptist \(2005\)](#) proposes a split in the terms in such a way that the bed shear stress computed using the depth averaged velocity u and the net bed roughness C equals the bed shear stress computed using the velocity u_v within the vegetation layer and the real bed roughness C_b . This can be written as:

$$\frac{u^2}{C^2} = \frac{u_v^2}{C_b^2} \quad (4.11)$$

With this requirement, the bed roughness can be written as:

$$C = C_b + \frac{\sqrt{g}}{\kappa} \ln\left(\frac{h}{h_v}\right) \sqrt{1 + \frac{C_D n h_v C_b^2}{2g}} \quad (4.12)$$

and

$$\lambda = C_D n \frac{h_v}{h} \frac{C_b^2}{C^2} \quad (4.13)$$

This formulation of the bed roughness and flow resistance requires the vegetation height h_v , density n , drag coefficient C_D and alluvial bed roughness C_b as input parameters [Deltares \(2020a\)](#). The determination of n is done via $n = mD$, where m is the number of stems per square metre and D is the stem diameter.

4.2 Model set-up

The numerical models are used to observe the effects of mangrove width on the biophysical interactions in the South Ballina mangrove system. In order to qualitatively investigate this effect, two different models have been set up, representing the L- and S-transect. The stand-alone models have an idealised set-up, with a simple grid, bathymetry and hydrodynamic forcings. Both models are based on the

measured situation at the transects. In this research, the two-dimensional horizontal (2DH) model is used, which limits the computation time. Also, previous research indicates that this is a reasonable assumption since the differences in results between 2DH and 3D modelling are small, while the difference in computational time is significant (Horstman et al., 2015).

4.2.1 Model domain

A schematic representation of the area of interest and the model domain and boundary conditions of the S- and L-transect are shown in figures 29 and 30. The model of the short transect in the South Ballina mangrove forest has a flow domain of 800 meters in cross-shore direction, and 300 meters in along-river direction. The grid consists of two parts; the northern half of the river being one part, and the southern half of the river and the forest being the other part. The northern half of the river has a resolution of 3 by 10 meters, which has been chosen in order to decrease the computational time. For the rest of the domain a grid size of 3 by 2 meters is applied up until the middle of the river. The choice for a grid size of 2 meters in the cross-shore direction is due to the resolution of the elevation profile survey. This results in a grid of 100 by 272 cells. The L-transect model has a domain of 600 meters in cross-shore direction, and 300 meters in along-river direction. The grid is again split up in two sub-grids; the northern half of the river and the rest of the domain. These sub-grids have the same cell sizes as discussed for the S-transect. This results in a grid of 100 by 228 cells. While the 'Long' transect implies to be the longest transect, this is not the case when looking at the flow domain. This is due to the width of the river at the transect and the resulting boundary condition. This is further elaborated in section 4.2.5. There are two closed land boundaries at the North and South side of the models. The Northern boundary corresponds with the embankments of Ballina's township. The southern boundary represents the end of forest due to a road situated there. Two open boundary conditions are defined; a discharge boundary at the western boundary imposed by the Richmond River and a water level boundary at the eastern boundary representing the tides. Both hydrodynamic boundaries are imposed on the entire river width. They start at the upper part of the domain and end at the forest fringe ($\Delta y = 350m$ (L) and $\Delta y = 650m$ (S))



Figure 29: Location of the domain of both models within the estuary.

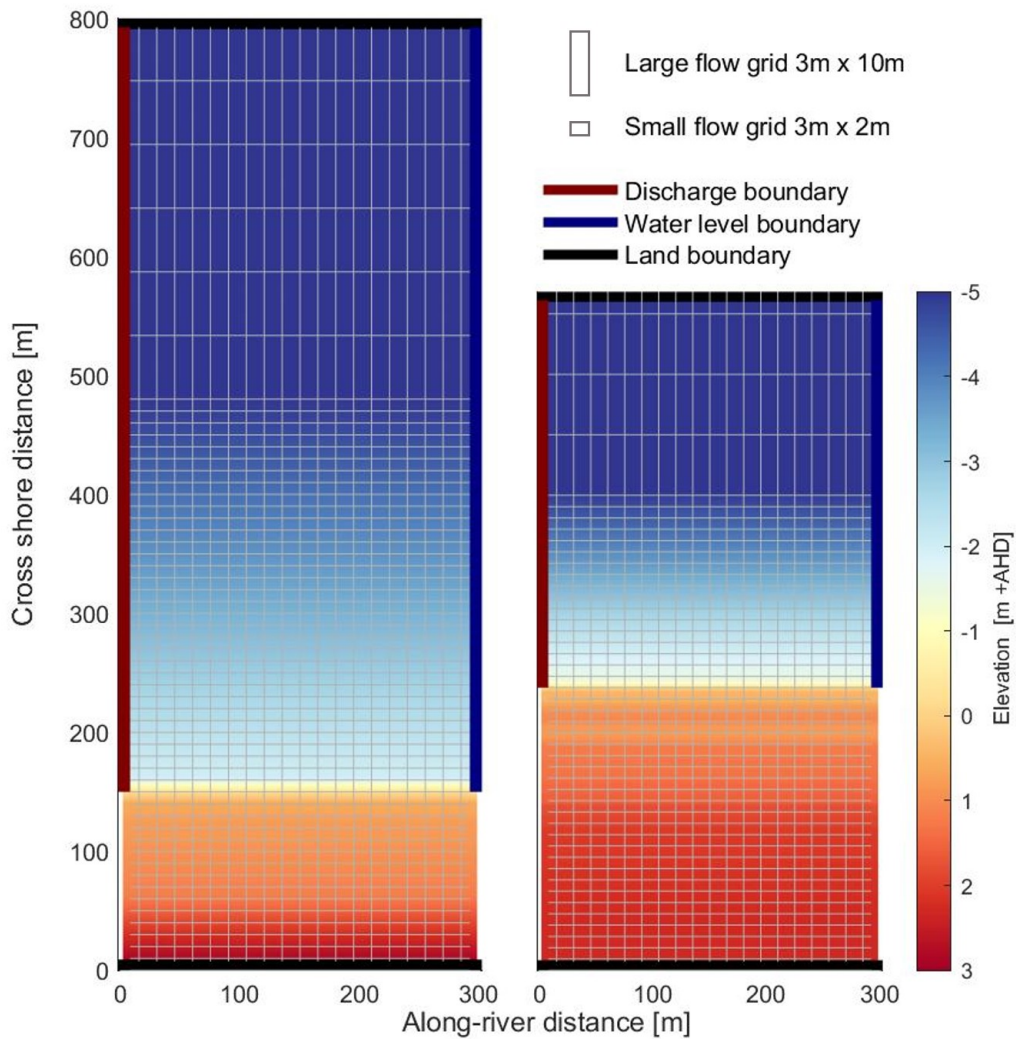


Figure 30: A schematisation of the domain for the S-transect (left) and L-transect (right), along with the different grid sizes and boundaries.

4.2.2 Time frame

The models run for a period of 10 days, which cover both spring and neap tides. The start-date for the S-transect is set at the 12th of March 2020 15:00. The L-transect start-date is set at the 9th of April 2020 11:00. Both start dates coincide with the hydrodynamic measurements. At the start of the model runs, the system will not be in equilibrium. A spin up time of one day is used to let the hydrodynamic boundaries get in an equilibrium and to prevent initial bed level changes impacting the results. The remainder of the run-time is used to investigate the biophysical interactions at both transects.

4.2.3 Bathymetry

The bed level ranges from 3 m +AHD at the back of the forest to around -5 m +AHD in the deepest part of the river (Hashimoto et al., 2006), see figure 31. The linear slope of the foreshore towards the river is equal for both models and is set at 0.01 m/m. In the along-river direction the (initial) bed level is uniform. A white noise perturbation between 0 and 3 cm was superimposed on the bottom elevation to simulate the natural variability of the substrate (Bryan et al., 2017; Willemsen et al., 2016). For the horizontal eddy viscosity and diffusivity values of $10 \text{ m}^2/\text{s}$ are used. This is a typical (default) value for the grid cell size used (Deltares, 2020a) and similar to what Willemsen et al. (2016) and Poppema (2017) used for a model study of mangroves and salt-marshes respectively.

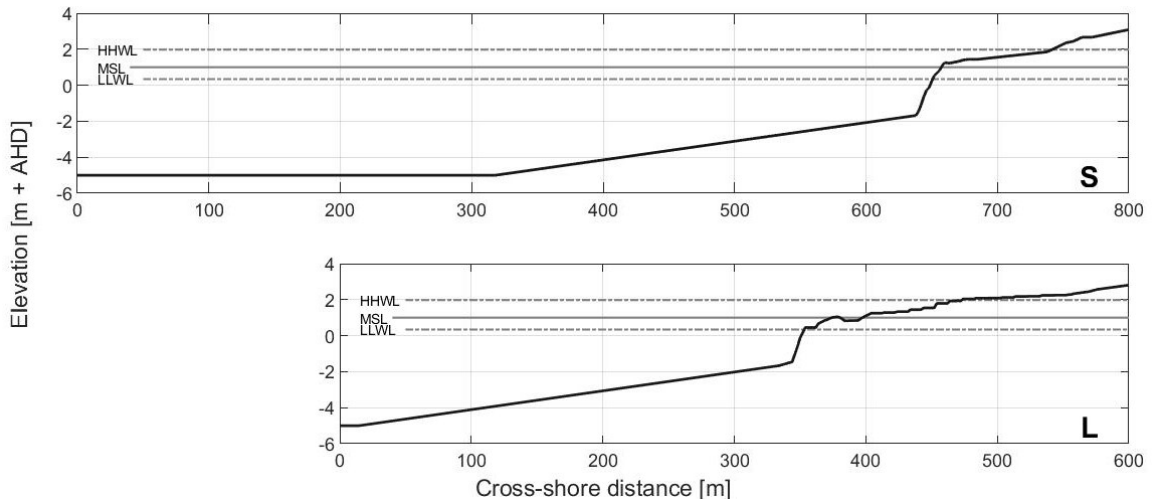


Figure 31: Initial elevation of both models in cross-shore direction. The initial profile is uniform in along-river direction. Characteristic tidal water levels are indicated near the left axis (HHWL = highest high water level; MSL = Mean Sea Level; LLWL = lowest low water level)

4.2.4 Vegetation cover and bed roughness

Both the pneumatophores and trees influence the hydrodynamics within the system, however the parameterisation of vegetation only allows one input per cell. Averaging the trees and pneumatophores per m^2 gives a distorted representation of reality due to the relative large difference between tree and pneumatophore height and diameter. Therefore, the flow resistance due to the pneumatophores is taken into account via the Manning bed roughness, which has to be calibrated. The flow resistance exerted by the trees is then taken into account by Baptist's formulation, through pre-defined polygons. The formulation of the bed roughness and flow resistance requires the vegetation height h_v , density n , drag coefficient C_D and alluvial bed roughness C_b as input parameters Deltares (2020a). The determination of n is done via $n = mD$, where m is the number of stems per square metre and D is the stem diameter. The average vegetation characteristics and density follow from table 3, C_D is set to 1. The Manning coefficient or alluvial bed roughness of the foreshore and river is calculated by rewriting the White-Colebrook formula and is set to $0.01 \text{ s}/\text{m}^{1/3}$.

Two different vegetation zones (see figures 16 17) are imposed in the model domain, representing the sparse *Avicennia marina*, and the dense *Aegiceras corniculatum* as shown in figure 32. The interval for updating the water depth-dependent bottom roughness due to the vegetation is set to 120 seconds. Input values are shown in table 7



Figure 32: Front view of the sparse *Avicennia marina* (left) and dense *Aegiceras corniculatum* (right).

Table 7: Vegetation density n , diameter D and vegetation height h_v for the two vegetation zones.

Sparse			Dense		
$n [m^{-2}]$	$D [m]$	$h_v [m]$	$n [m^{-2}]$	$D [m]$	$h_v [m]$
0.0255	0.051	4.46	0.528	0.033	2.94

4.2.5 Hydrodynamic boundary conditions

As stated before, both models contain two open boundaries: the river (western) boundary and the estuarine (eastern) boundary. The later simulates the tidal wave entering the system. These water levels were monitored throughout the field campaign by pressure gauges at L1 and S1. However, these obtained time series did not give a continuous tidal signal. Also, the water level data near Byrnes Point and Missingham Bridge, which are located upstream of both models, show small disturbances in tidal signal due to river discharge variations. A pure tidal signal is desired, since river discharge peaks are of particular interest in the model scenarios. These scenarios are explained later in this section. In order to generate a pure tidal signal, the obtained water levels at Byrnes Point were ran through the UTide Matlab function by Codiga (2011). This resulted in a very similar tidal signal compared to Byrnes Point, but with no fluctuations due to the river (see figure 33)

The discharge boundary is required to model the flow velocities and behaviour of the tidal wave correctly. During flood tides, the tidal wave propagates through the estuary up to 40 km upstream

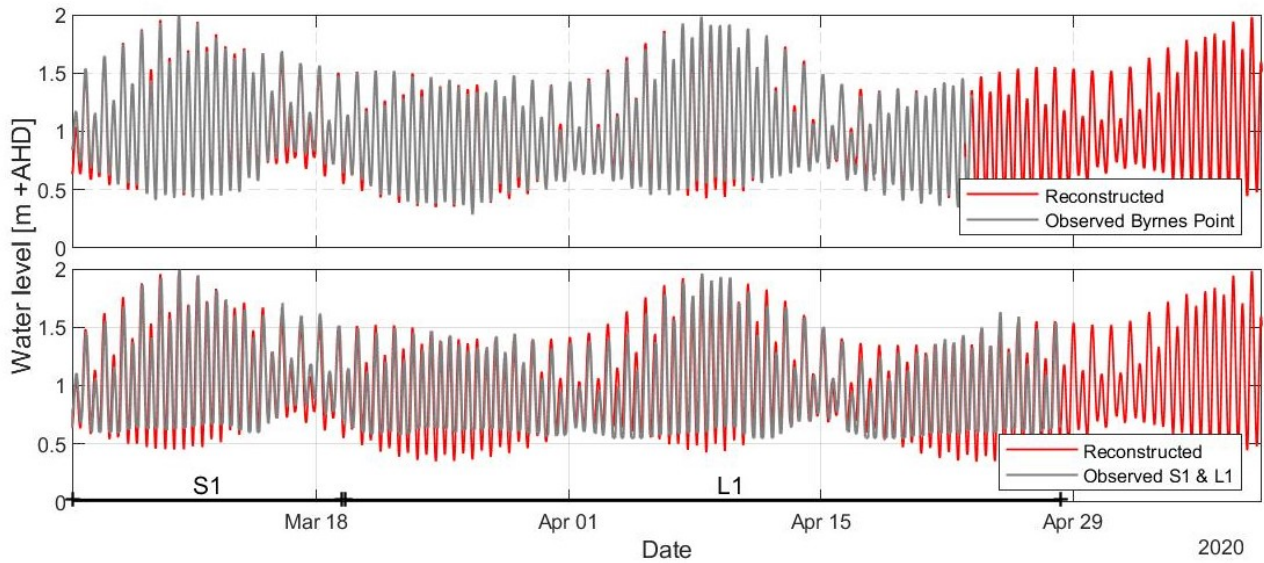


Figure 33: Reconstruction of the tidal signal along with observed water levels at Byrnes Point (top) and S1 and L1 (bottom).

of the estuary mouth Hashimoto et al. (2006). During normal flow conditions of the river, the river's discharge is forced back into the estuary during the flood phase of tide, resulting in an accumulation of water upstream. After the time of maximum high tide, the accumulated water front will travel downstream and out of the estuary's mouth until the end of the ebb tides. The models represent only a small section within the estuary, so these complex dynamics have to be translated into one variable boundary condition. Theoretically, flood tides entering the system at the eastern boundary will travel through the domain and exit the system at the western boundary resulting in an accumulation of water upstream of the river and outside the domain. During ebb-tides, the direction of flow is reversed, and the upstream accumulated water re-enters the system at the western boundary and exits the domain at the eastern boundary. This water body consists of a mixture of fresh and salt water. The maximum rate of discharge into the model from the upstream part of the river is therefore observed at mid tide during ebb, when the flow velocities will also be the highest. The maximum rate of discharge out the model into the upstream part of the river is around the middle of flood tide. The discharge boundary can therefore be seen as a function of the tidal wave. Due to the lack of available data regarding the temporal variability in discharge of the Richmond River, this boundary has to be constructed. The constructed discharge boundary is set-up based on the reconstructed tidal boundary but with a delay in period of around 1/4 the tidal period. This is also visualised in figure 35, where the top plot shows the reconstructed tidal boundary condition and the constructed discharge boundary. The bottom plot is a close-up of the marked grey area in the top plot. This plot also shows the base discharge Q_{base} , representing the mean river discharge. In other words, this is the amount of water that is effectively being discharged over time. The maximum discharge Q_{max} equals the maximum amount of water that is being discharged at a certain moment.

Figures 24 and 27 showed that during spring tides the flow is directed both downstream (ebb tide) and upstream (flood tide), indicating a reversal of flow within the domain. This implies that during flood tides, the flow velocities and discharge have to become negative and directed upstream. These figures show on the other hand that during neap tides the flows are predominantly directed downstream. At the L-transect, flood tides are constantly being repressed, while at the S-transect every other flood tide is repressed. It is therefore concluded that both transects are situated closely towards the turning point where no flow reversal during neap tides occurs. Following from this, it is assumed that during neap tides $0 \text{ m}^3/\text{s}$ is being discharged. With this assumption, the directions of flow are in line with the field observations.

Figure 34 shows the steps which are taken to come to the constructed discharge boundary. In the asymmetrical sinusoidal shaped function of the reconstructed tides, the mean water level has a value of ≈ 0.4 of the amplitude A (top plot). Furthermore, analysing the fraction between spring low tide and neap low tide gives a proportion of $\approx 0.25A$. This also gives a proportion of $\approx 0.15A$ between the neap low tides and the mean. As concluded above, the discharge boundary is a function of the tidal boundary but is scaled accordingly. Scaling the function does not affect the proportions, so the ratio between the Q_{base} and Q_{max} is also $\approx 0.4A$ (middle plot). When the discharge at neap tide is placed at $0 \text{ m}^3/\text{s}$, the difference between zero discharge and Q_{base} then becomes $\approx 0.15A$. After this, Q_{base} becomes $\approx 0.15A$ and Q_{max} becomes $\approx 0.75A$. By getting rid of the amplitude A , this can be rewritten to; $Q_{base} = Q_{max}/5$. Since Q_{base} and Q_{max} highly influence the direction and magnitude of the currents in the model domain these are being calibrated. This is explained later on this chapter.

No wave conditions are imposed on the boundaries due to multiple reasons. First, the wind conditions are predominantly originating from the South and West (Meteorology, 2020). This results in a limited fetch and no wind induced waves. Secondly, during the fieldwork period, no significant waves entering the mangroves were observed. Analysis of the pressure gauge data for variations due to waves is inconclusive due to the resolution of the sampling period being too large. Lastly, due to the breaker walls and the shape of the mouth of the estuary, no waves originating from the sea can enter the system.

4.2.6 Sediment dynamics

Since flow velocities in the study area are too small to transport (substantial amounts of) sands in suspension, only 1 sediment type is used per model; (cohesive) mud. Also, the addition of an extra sediment boundary significantly increases the run-time. Default values are used for the density and dry bed density of the sediment, which are $2650 \text{ kg}/\text{m}^3$ and $500 \text{ kg}/\text{m}^3$ respectively. The initial thickness of the sediment layer is set at 5 metres up until $y = 250\text{m}$ (S) and $y = 350\text{m}$ (L). For larger y values the layer thickness is set to 0. This is done to prevent the occurrence of erosion in the channel and resuspension of additional sediments. (Poppema, 2017; Willemsen et al., 2016). The value for critical bed shear stress for erosion is set at the value of $0.15 \text{ N}/\text{m}^2$ (Horstman et al., 2013b). The value for critical bed shear stress for sedimentation is set at $1 \text{ N}/\text{m}^2$. Lastly, the erosion parameter M is set to $0.1 \text{ mg}/\text{m}^2/\text{s}$, which is the default value of Delft-FM (Deltares, 2020a).

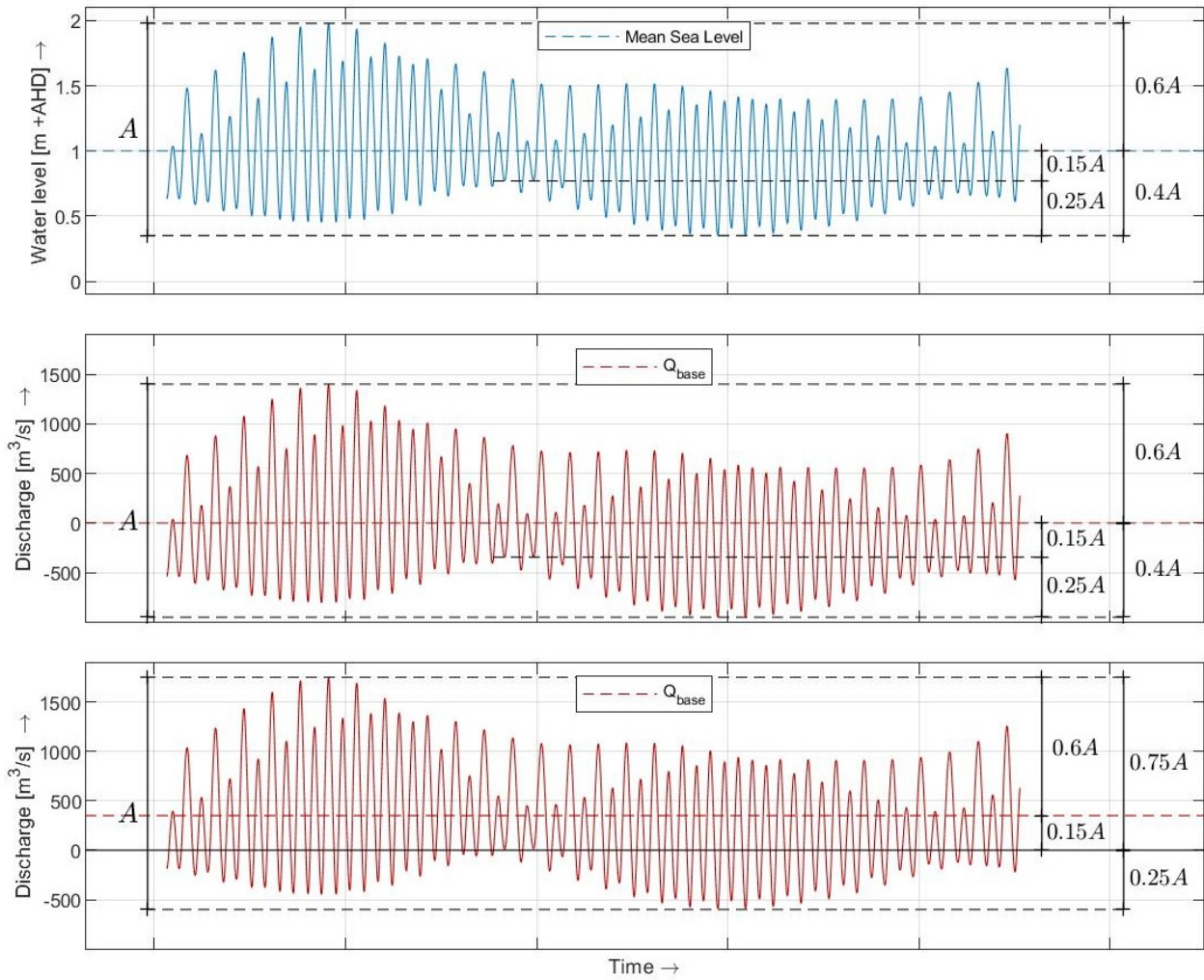


Figure 34: Scaling and transformation of the discharge boundary based on ratios in the water level boundary.

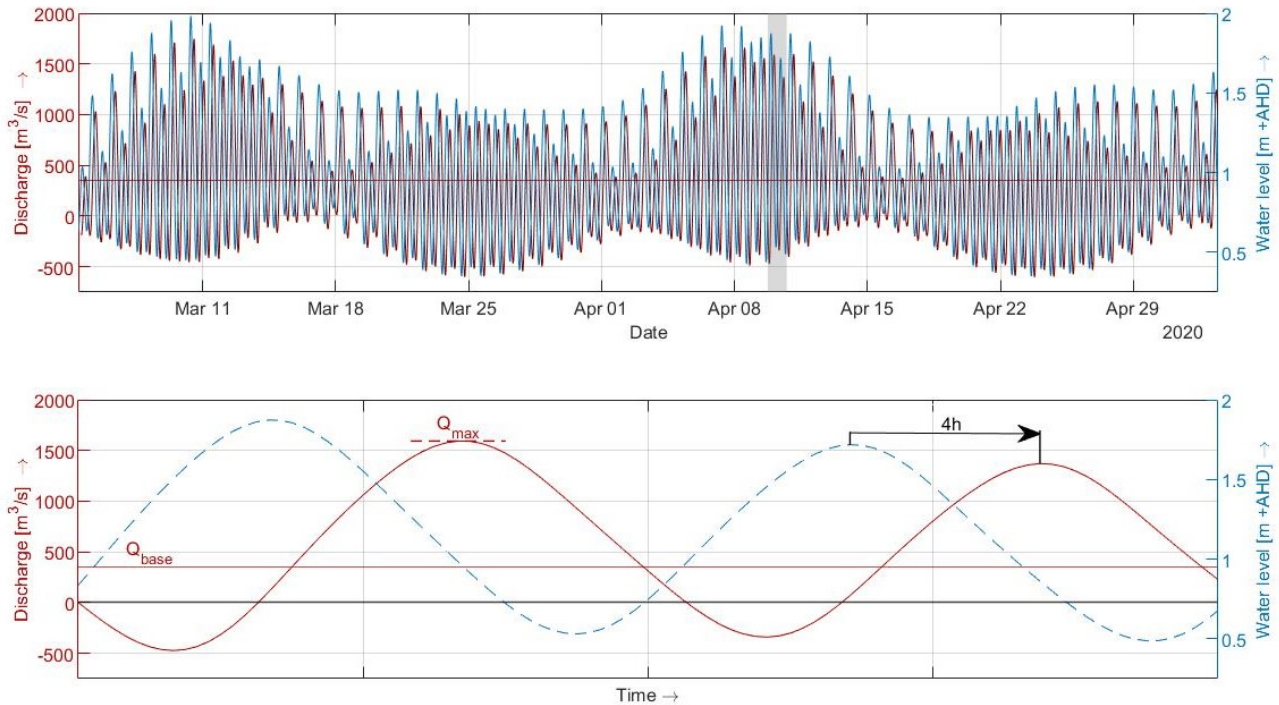


Figure 35: Constructed discharge and reconstructed tidal boundary conditions (top). The marked grey area indicates the time period of the bottom plot, where a close up of the discharge and tide set-up is shown.

At the seaward side the sediment concentration is initially set at zero. This implies that no sediment will enter the domain during flood tide initially, whereas sediment may leave the domain during ebb tide. Furthermore, at both hydrodynamic boundaries the bed level is set to be constant. Physically, this can be explained by the fact that South Ballina mangrove system is located within a larger system (i.e. Ballina’s estuary), which remains mostly constant. And numerically, it has the advantage that it prevents the occurrence of instabilities at the boundaries. To prevent discontinuity in the concentrations at the turn of the flow, the model applies a so-called ‘Thatcher-Harleman’ time lag at the boundaries of 120 min. This time lag is the return time for concentration from its value in the outflow relative to its value specified in the inflow. This implies that sediment concentration entering the model domain during flood is determined during the time lag by the concentration leaving the model domain during ebb by means of a temporary storage of concentration data [Deltares \(2020b\)](#). The sediment concentration at the landward side is being calibrated, and explained later in this chapter.

4.2.7 Set-up summary

A summary of the set-up of both models can be seen below in table 8.

Table 8: Set-up overview for both transects.

Parameter	Value		Meaning	Source/remarks
	<i>S-transect</i>	<i>L-Transect</i>		
Grid and bathymetry				
M	100	100	# cells in x-direction	
N	272	228	# cells in y-direction	
Δx	3 m	3 m	Grid resolution in x-direction	
Δy	2 m	2 m	Grid resolution in y-direction	Applies until y = 420 (L) and y = 480 (S)
Δy_{river}	10 m	10 m	Grid resolution of the river in y-direction	
$y_{mangrove}$	150 m	250 m	Mangrove width	
y_{open}	650 m	350 m	Open boundary width	
δt	120 s	120 s	Time step of model	
δt_n	180 s	180 s	Time step of updating bottom roughness	
MorStt	86400 s	86400 s	MorFac spin-up time	
z_{min}	-5 m	-5 m	Minimum elevation bed	
z_{max}	2.50 m	2.30 m	Maximum elevation bed	
Roughness and viscosity				
C_b	0.01	0.01	Alluvial bed roughness	
m	0.02	0.02	Manning coefficient	To be calibrated
Γ	10 m^2/s	10 m^2/s	Horizontal eddy viscosity	Willemsen et al. (2016); Poppema (2017)
K	10 m^2/s	10 m^2/s	Horizontal eddy diffusivity	
Sediment dynamics				
ρ_{sed}	2650 kg/m^3	2650 kg/m^3	Specific density sediment	Deltares (2020b)
P_{sed}	500 kg/m^3	500 kg/m^3	Dry bed density	Deltares (2020b)
w_s	0.5 mm/s	0.5 mm/s	Settling velocity	To be calibrated
$\tau_{cr,e}$	0.1 N/m^2	0.1 N/m^2	Critical bed shear stress erosion	Horstman et al. (2013b)
$\tau_{cr,s}$	1000 N/m^2	1000 N/m^2	Critical bed shear stress sedimentation	Deltares (2020b)
M	0.1 $mg/m^2/s$	0.1 $mg/m^2/s$	Erosion parameter	Borsje et al. (2008); Deltares (2020b)
C_{mud}	0.03 kg/m^3	0.015 kg/m^3	Mud concentration at boundary	To be calibrated

4.3 Model calibration

In order to accurately simulate the dynamics in the mangrove system, the models first need to be calibrated. The calibrated model of the current situation also functions as the base for the applied scenarios, where seasonal variations are compared with the current situation. Calibration runs were executed during consecutive spring tides, in order to compare the model predictions with the field observations. The time frame for these runs is three days, and is shown in figure 36

4.3.1 Current velocities

The discharge appears to be a major driver on the modelled flow velocities. Both the base discharge as the maximum discharge play a major role in the behaviour of the hydrodynamics within the model. In section 4.2 the ratio between the maximum discharge Q_{max} and base discharge Q_{base} is already set at 5, but now the value of the maximum discharge is being determined. The main goal of calibrating this parameter is to correctly model the direction of flow during flood and ebb tides. The magnitude of flow is also of interest, but this is being fine-tuned by the Manning's coefficient calibration.

Five runs with varying maximum discharges of $750 \text{ m}^3/\text{s}$, $1000 \text{ m}^3/\text{s}$, $1250 \text{ m}^3/\text{s}$, $1500 \text{ m}^3/\text{s}$ and $1750 \text{ m}^3/\text{s}$ were executed. The mean value of $1250 \text{ m}^3/\text{s}$ is based on work by Hossain et al. (2001), where they state that the average water exchange through the mouth of the river lies around $1400 \text{ m}^3/\text{s}$. This is however a summation of the Richmond River and North Creek, and therefore the mean value is chosen slightly smaller. The lower limit of $750 \text{ m}^3/\text{s}$ is based on work by Hossain et al. (2001), corresponding with measurements taken upstream of the Richmond River. where it represents a mean annual discharge. However Hossain et al. (2001) also state that most of the flow from the Richmond River catchment is generated during the wet season (89–94%). The fieldwork period, and therefore also the simulation period, took place during the wet season, so relative high discharges apply. Based on this, no discharge lower than $750 \text{ m}^3/\text{s}$ is considered.

Secondly, the magnitude of the flow velocities is being calibrated by means of the bed roughness. This roughness parameter is representative of the bulk effect of momentum losses by bed friction, pneumatophores friction, discontinuities in elevation, and any other momentum loss (Baptist, 2005). As equation 4.4 shows, the bed shear stress is being determined by the Chézy coefficient C_{2D} . This coefficient is expressed by the Gauckler-Manning-Strickler formulation $C = \sqrt[6]{R}/n$. The hydraulic radius R is typically equivalent to the water depth h in 2D. Manning's coefficient is being calibrated in the range $0.02 - 0.05 \text{ s}/\text{m}^{-1/3}$, this is a roughness similar to previously applied roughness coefficients in mangrove studies by e.g. Horstman et al. (2015); Mazda et al. (1995); Furukawa et al. (1997). Three runs with the following roughness coefficients are executed; 0.02 , 0.035 and $0.05 \text{ s}/\text{m}^{-1/3}$.

In order to determine the optimal discharge and Manning's coefficient, the model accuracy coefficient, MA, was expressed through the Nash-Sutcliffe (Horstman et al., 2015; Temmerman et al., 2005):

$$NSE = MA = 1 - \frac{\sum(\overline{SIM} - \overline{REF})^2}{\sum(\overline{SIM} - \overline{REF})^2} \quad (4.14)$$

In equation 4.14, the overlines indicate time-averaged values of the flow velocities. The closer MA

approximates 1, the better the model simulates the observations. According to [Moriassi et al. \(2007\)](#), $NSE = 1.0$ is the perfect fit, $NSE > 0.75$ is a very good fit, $NSE = 0.64$ to 0.74 is a good fit, $NSE = 0.5$ to 0.64 is a satisfactory fit and $NSE < 0.5$ is an unsatisfactory fit. MA calculations were performed for time-steps where there were both observed as modelled flow velocities data points.

4.3.2 Sediment deposition

As stated before, the sediment fluxes are calculated with the Partheniades-Krone formulations (equations 4.7 - 4.9). Important parameters of these formulations are amongst others the fall velocity w_s , the critical erosion shear stress $\tau_{cr,e}^{(l)}$, the average sediment concentration $c_b^{(l)}$ and the critical deposition shear stress $\tau_{cr,d}^{(l)}$. Initial runs showed the sensitivity of the models to the settling velocity and the sediment concentration used as input. No unambiguous data from the field are available regarding these parameters and therefore the models are being calibrated in these parameters.

The sediment concentration as defined by the boundary conditions are being calibrated. Water sample analysis was performed during the fieldwork period. Samples were taken during four moments in the spring and neap cycle and showed distinctive results between the transects (see table 4). Two representative values were chosen for each transect, corresponding with values measured at high and low tide during a spring and neap tide. The values are 30 mg/l and 90 mg/l for the L-transect, and 15 mg/l and 30 mg/l for the S-transect. In addition to the sediment concentration, the settling velocities are calibrated. Settling velocities of cohesive sediment in shallow tidal waters generally range between 0.1 and 1 mm/s ([Wolanski, 1992](#)). Therefore, four runs with the following values are executed: 0.25 mm/s , 0.5 mm/s , 0.75 mm/s and 1.0 mm/s . A summary of the calibration parameters and their range is shown in table 10.

4.4 Validation

In order to assess the accuracy of both models outside the calibration time frames, a validation run per model is executed. Both models are calibrated for spring tides due to the availability of the deposition data. So, the validation runs are chosen during neap tides. The aim of the validation runs is also to see whether the models can predict the flow characteristics as observed in the field accurately. The validation runs are again three days, and shown in figure 36. For the validation runs, the model accuracy coefficient is also explained by the MA.

4.5 Scenarios

Sediment transport in the Richmond's River estuary is controlled by both periodic fortnightly tidal variation, and a-periodic floods [Hossain et al. \(2001\)](#). During aperiodic events many estuaries can carry high suspended sediment loads, and this can drastically change the pattern of sediment transport and deposition within the mangrove system ([Hossain et al., 2001](#)). Three different scenarios were designed to investigate the impact of variations and conditions on the biophysical interactions in the mangrove system on a seasonal scale. The scenarios are run for 10 days. the start and stop date and time for both transects is shown in table 9. All scenarios and their settings are discussed below.

Table 9: Time frame of the runs

	S-transect	L-transect
Start time	12-03-2020 15:00	11-04-2020 11:00
Stop time	22-03-2020 15:00	21-05-2020 11:00

4.5.1 Reference

A reference scenario is used in order to accurately observe the effects of the other scenarios. The reference scenario is based on the calibrated models. The models have been calibrated for spring tides, so the aim of this scenario run would not only be to for comparison, but also to validate the performance during neap tides. The imposed boundary conditions are shown in figure 36.

4.5.2 Low flow

The second scenario represents the conditions during low flow, when the river discharge as well as the sediment supply is restricted. In this scenario the water level boundary remains the same as the reference scenario. According to Hossain et al. (2001), during low flow conditions the base discharge Q_{base} nearly becomes zero. However, tidal waves still cause a displacement of water in and out the model. Under normal conditions, this water exchange varies between 1400-1600 m^3/s during ebb and flood tides Hossain et al. (2001). Q_{max} is therefore set at 1400 m^3/s . A constant discharge Q_{base} of 10 m^3/s is used, based on measurements taken from Hossain et al. (2001). The constructed discharge boundary is shown in figure 36. The sediment concentration during low flow is set at 10 mg/s for both transects Hossain et al. (2001).

4.5.3 River flood

Little recent quantitative data is available regarding river discharges and sediment concentrations during floods, although they occur occasionally (Ryder et al., 2015). The river flood scenario is based on work by Hossain et al. (2001) and Hossain and Eyre (2002). Statistical analysis by Hossain et al. (2001) showed that the Richmond River was subjected to two minor floods (1 in 2 year return period) during the 1994-1995 hydrological year. Whereas, during the 1995-1996 hydrological year the catchment produced one moderate flood (1 in 5 year return period). Since more data is available regarding the minor floods, these are used as the basis for this scenario.

The maximum observed discharge rate during one of these floods was about 2670 m^3/s (Hossain et al., 2001). If a constant discharge boundary would be considered, then fluctuations in flow velocity due to the flood tides pushing back would not be taken into account. So the flood discharge needs to have the same shape as the reference situation, but with higher base and maximum discharges. Therefore the 2670 m^3/s is used as the Q_{max} of this scenario. The base discharge is then determined by calculating the difference between the maximum discharge after calibration and the 2670 m^3/s . This difference is then added to the base discharge, since it represents the additional discharge by the river flood. Also, to mimic the increased water levels during a flood, the tidal signal has been altered and is shown in figure 36. The size of the domain in along-river direction is small, which results in

a uniformly increase or decrease in water levels. The water levels due to the floods can therefore be imposed on the seaward boundary and are constantly $2 \text{ m} + \text{AHD}$ based on measurements by (Hossain et al., 2001). Finally, sediment samples taken by Hossain et al. (2001) during river floods yielded values of around 300 mg/L , this is used as an constant input.

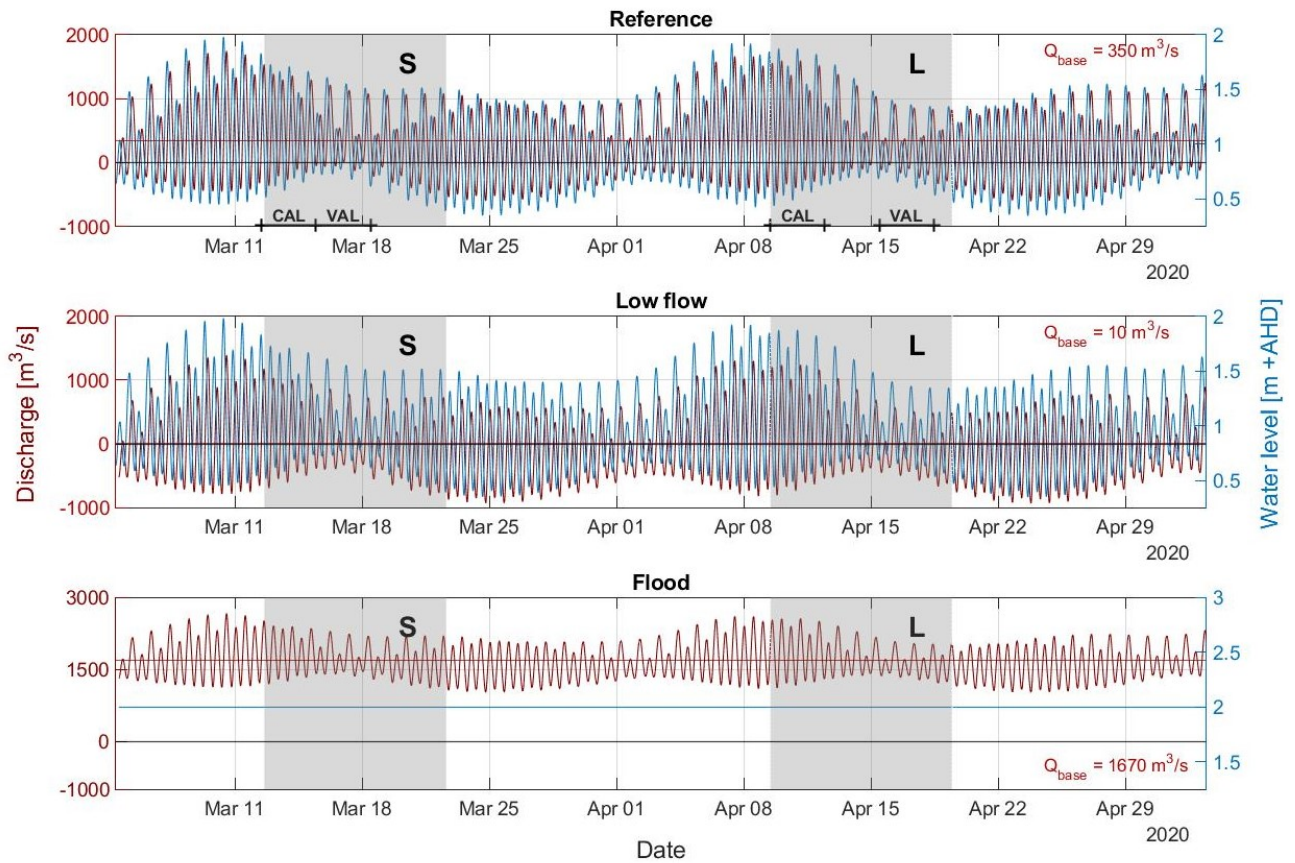


Figure 36: Tidal and discharge boundary settings for all scenarios. The marked areas indicate the modelled period for the S-transect (S) and L-transect (L). Calibration (CAL) and validation (VAL) time frames are indicated in the top plot.

4.6 Calibration and scenario summary

A summary of the calibration runs can be seen below in table 10. A summary of the altered parameters for the scenario runs is given after the calibration results in table 12 in chapter 5.

Table 10: Overview of the calibration runs

Calibration	Parameter	Range	Unit	# of runs per model
Flow velocities	n	0.02 - 0.05	$s/m^{-1/3}$	3
	$Q_{max,s}$	1250 - 1750	m^3/s	3
	$Q_{max,l}$	750 - 1750	m^3/s	5
Sediment deposition	w_s	0.25 - 1.0	mm/s	4
	$C_{discharge,S}$	15 - 30	mg/l	2
	$C_{discharge,L}$	30 - 90	mg/l	2

5 Model results

This chapter presents the results of the model study. First, the results of the calibration are presented, and elaborated extensively. This subsection will conclude with a summary in which the final calibration choices are being summarised. Then, the results of the three modelling scenarios compared to the reference situation are shown.

5.1 Calibration

In order to obtain a model representation of the processes that are of interest, model parameters have been adjusted within the margin of their uncertainties. The model is calibrated with regards to the flow velocities and the sediment deposition within the domain. A summary of the model accuracies (MA) are shown in table 11. These accuracies are further elaborated in the sections below.

5.1.1 River discharge

The model was first calibrated for the observed flow velocities by means of the variable discharge quantity. The main goal of this parameter was to obtain similar directions of flow as measured in the field. Secondary, the magnitude of the flow velocities are also impacted by this parameter and therefore investigated. Five runs were executed for the L-transect with varying discharges of 750 - 1000 - 1250 - 1500 - 1750 m^3/s . Hereafter it became clear that the 750 and 1000 m^3/s runs were not necessary for the S-transect.

The results for the direction of flow are shown in figures 37 and 38. In this plot the x and y component of the modelled and measured flow velocities are shown. The directions of the observed flow velocities were altered, based on the relative position of the fringe, to correspond with the modelled velocities. All calibration runs for both transects show good agreement with the x component (along-river direction). Negative values indicate flow directed upstream while positive values are downstream directed flows. Positive flow velocities become larger with an increase in discharge for both transects, and is in line with the direction of the discharge boundary. It is interesting to see that also the upstream directed negative flows become larger with increasing discharges, which is due to the increasing negative discharges imposed on the boundary. This observation seems to be more significant at the S-transect compared to the L-transect. The modelled maximum negative and positive discharges also differ between the transects. Larger negative flows can be seen at the S-transect (± -15 cm/s (S) and ± -10 cm/s (L)), while the L-transect has larger positive flows (± -17.5 cm/s (S) and ± 10 cm/s (L)). This can be an indication for the S-transect model to be more sensitive towards the tidal boundary,

Table 11: Model accuracies (MA) of the calibration runs.

	Q [m^3/s]					n [$m^{1/3}/s$]		
	750	1000	1250	1500	1750	0.02	0.035	0.05
<i>S-transect</i>	-	-	0.79	0.73	0.76	0.76	0.69	0.57
<i>L-transect</i>	0.52	0.56	0.52	0.57	0.61	0.61	0.62	0.61

while the L-transect model is influenced more by the discharge boundary. Especially the results of the x component is of interest when interpreting these results, since the observed velocities are mostly in the y plane. Both models show very little flow in the y plane, especially the S-transect model. Theoretically this can be explained by the locations of the forest fringe of both transects relative to the river stream. The S-transect is more angled towards the river stream, while the L-transect is more or less perpendicular. In both models the transects are exactly perpendicular towards the river stream, explaining the slightly different direction of the predicted velocities compared to the observed velocities.

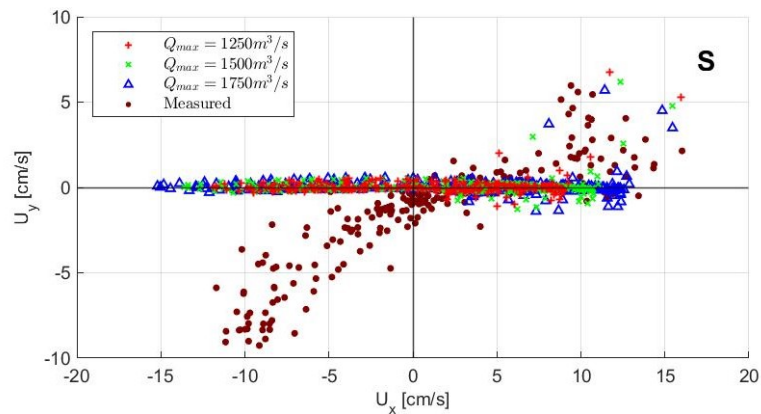


Figure 37: X and Y component of the measured and modelled flow velocities at S1.

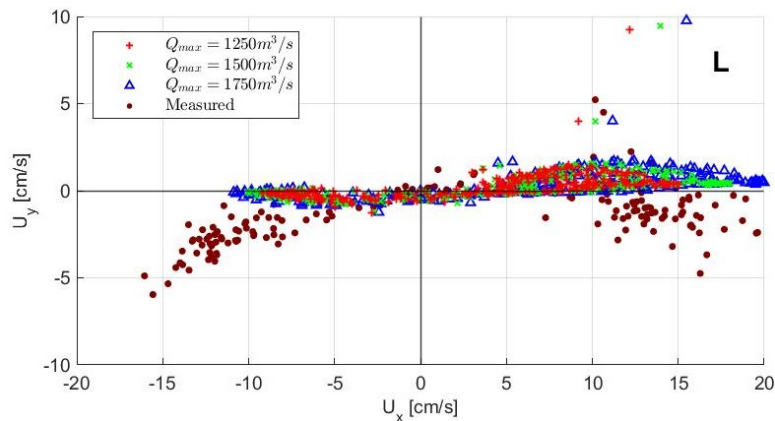


Figure 38: X and Y component of the measured and modelled flow velocities at L1.

Figures 39 and 40 show the magnitude of the flow at S1 and L1 over the time, along with the moving average of the field measurements. It should be noted that the field observations are an weighted moving average (60-min, see chapter 2), in order to filter out any irregularities. The duration of the measured tidal wave therefore appear shorter than the modelled tidal wave, but this is partly due to the moving average discarding the outer values. Another reason is the lack of field observations for

water depths smaller than 40 cm. The blue dashed line indicates the modelled water level. Figure 39 shows that for most tides at the S-transect, the flow velocity during flood tide is overestimated for all runs. The timing of slack tide during high water (HW) is represented well for nearly all tides, however, the last two tides are about 1-2 hours out of sync compared to the field observations. Possible explanations for this could be significant onshore directed winds, sudden increase of river discharges or other natural variability's. The model produces slight tidal asymmetries, starting with a stronger flood flow velocities, and ending with stronger ebb flow velocities. Overall, a discharge of $1250 \text{ m}^3/\text{s}$ shows to be a very good fit with regards to the field observations ($\text{MA} = 0.79$) but with a small underestimation of the flood tide. Model accuracies of $1500 \text{ m}^3/\text{s}$ ($\text{MA} = 0.73$) and $1750 \text{ m}^3/\text{s}$ (0.76) are similar and also appear a good fit (Moriassi et al., 2007).

Figure 40 shows the results for the L-transect. All runs show decent agreement with the shape of the majority of the measured velocity profile. The L-transect model shows, in line with figure 38, a clear tidal asymmetry with the ebb-tide being more dominant. To a certain degree, larger discharges perform better regarding the estimation of the ebb tides, while the performance during flood tide is not constant. The L-transect shows accurate estimates of slack tides during HW, where velocities nearly become zero. But, the modelling of the fourth tidal wave is, comparable with the S-transect, out of sync with the field observation, possibly indicating natural variability in the tides or rivers. A discharge of $1750 \text{ m}^3/\text{s}$ shows to be a satisfactory fit for the L-transect ($\text{MA} = 0.6$). Other runs show lower accuracies but are also satisfactory.

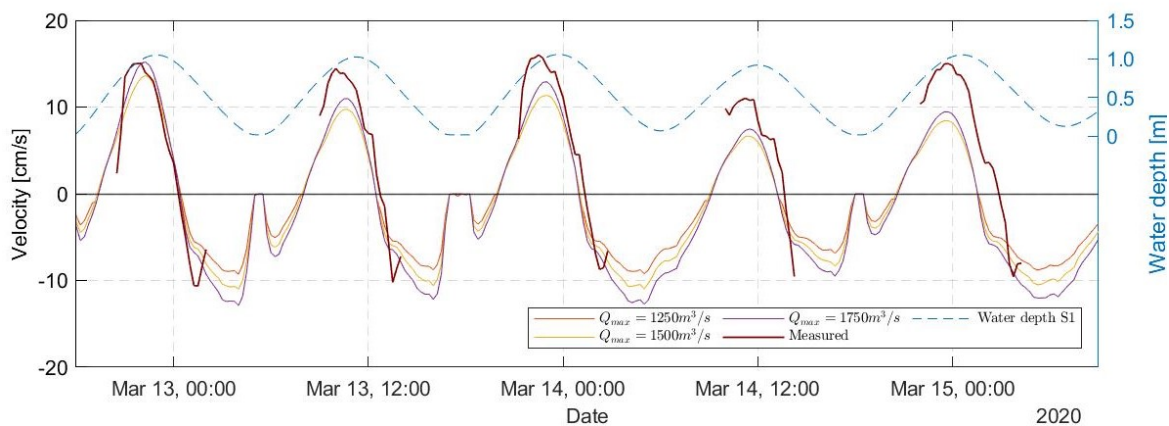


Figure 39: Magnitude of the modelled and measured flow velocity at S1. Blue dashed line indicates the modelled water level.

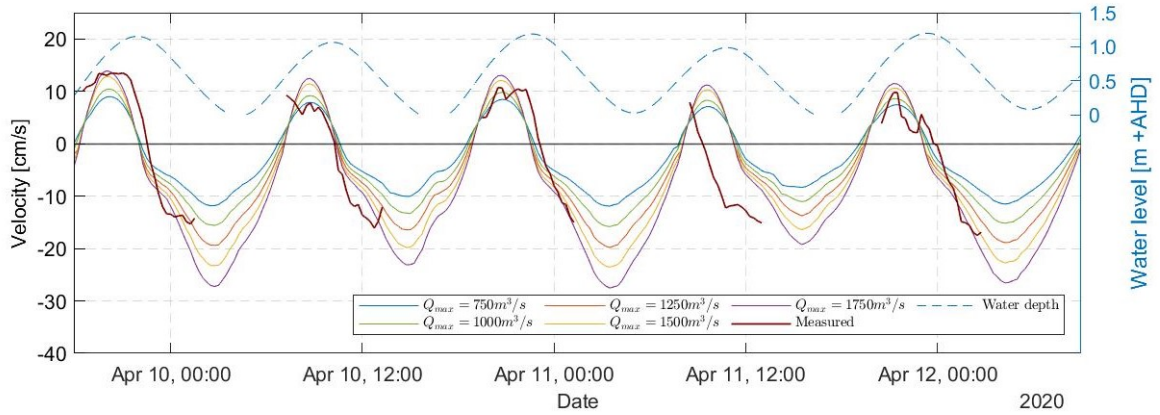


Figure 40: Magnitude of the modelled and measured flow velocity at L1.

5.1.2 Manning's coefficient

Secondly, the models were calibrated by the Manning coefficient within the range of $0.02 - 0.05 \text{ s/m}^{-1/3}$. The results as well as the field observations are displayed in figures 41 and 42. These figures show all calibration runs as well as the field observations and the modelled water levels.

In general, both transects show as expected lower flow velocities with increasing Manning coefficients. The degree in which the flow velocity decreases between different parameter values is larger for the L-transect. Here, a decrease of maximum 7 cm/s during ebb tides between the parameter values of 0.02 and 0.035 can be seen, while a decrease of 3-4 cm/s is modelled at the S-transect. This can be explained by the width of both transects. The tidal wave travels further into the forest at the L-transect, travelling a larger surface area. This larger surface area leads to more momentum loss due to the bed roughness. A Manning coefficient of 0.02 appears to be a very good fit for the S-transect model (MA = 0.76). A coefficient of $n = 0.035$ (MA = 0.69) is a good fit, and $n = 0.05$ (MA = 0.57) is satisfactory. All roughness coefficient calibration runs for the L-transect are satisfactory, with a coefficient of 0.035 being slightly better (MA = 0.62) compared to $n = 0.02$ and $n = 0.05$ (both MA = 0.61).

5.1.3 Sediment deposition

Two times four runs have been executed with different sediment concentrations and settling velocities as input. The time frame of both models corresponded with the time frame of the tile sampling, enabling comparison between the model and field. In figures 43 and 44 the deposition rates for the two parameter settings are shown per location.

Both models clearly show increased deposition of sediments near the forest fringe. Almost all applied combinations of settling velocities and sediment concentrations overestimate the deposition rates at S2 and L2. For settling velocities between 0.25 and 0.75, the deposition rates are still within the same order of magnitude $O(10^1) \text{ mm/day}$. Sediment deposition decreases substantially for increasing

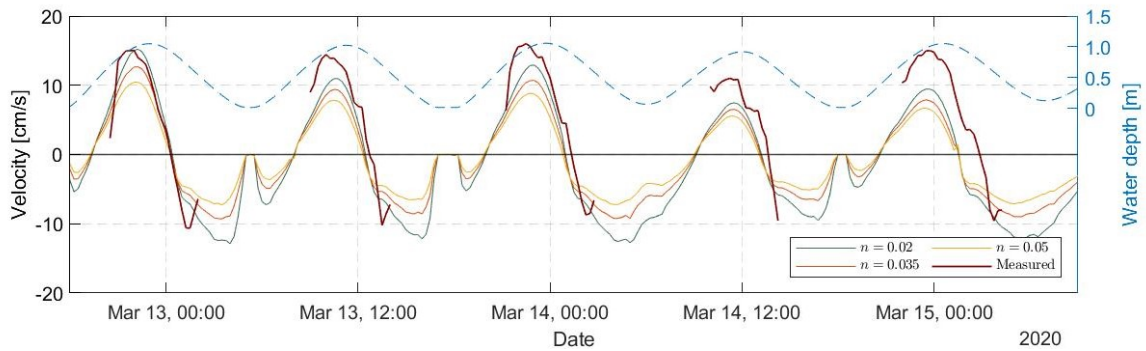


Figure 41: Results of the bed roughness calibration at S1.

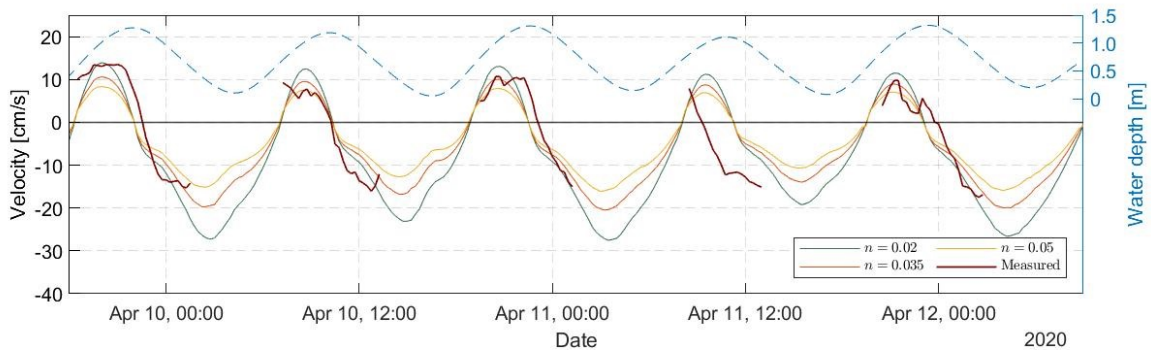


Figure 42: Results of the bed roughness calibration at L1.

settling velocities and decreasing sediment concentrations. The model results compare well with the deposition rates within the forest at S3 and L3. Near S3 the deposition is slightly underestimated for almost all calibrating runs, but appear to be correlating well with field observations. L3 on the other hand shows almost zero deposition for the 30 mg/l runs. Physically this can be explained by the fact that the elevation of L3 is almost the same as the height of the spring tides. Combining this with a computational threshold for sediment the morphodynamics in Delft-FM results in almost none deposition. At S4 and L4 no deposition is observed for all parameter ranges. This is due to the fact that during the modelled time frame no inundation occurs. However the tiles did contain deposited sediment in the field during the same time frame. This is likely due to the heavy rainfall within that period, inundating the forest and displacing sediment.

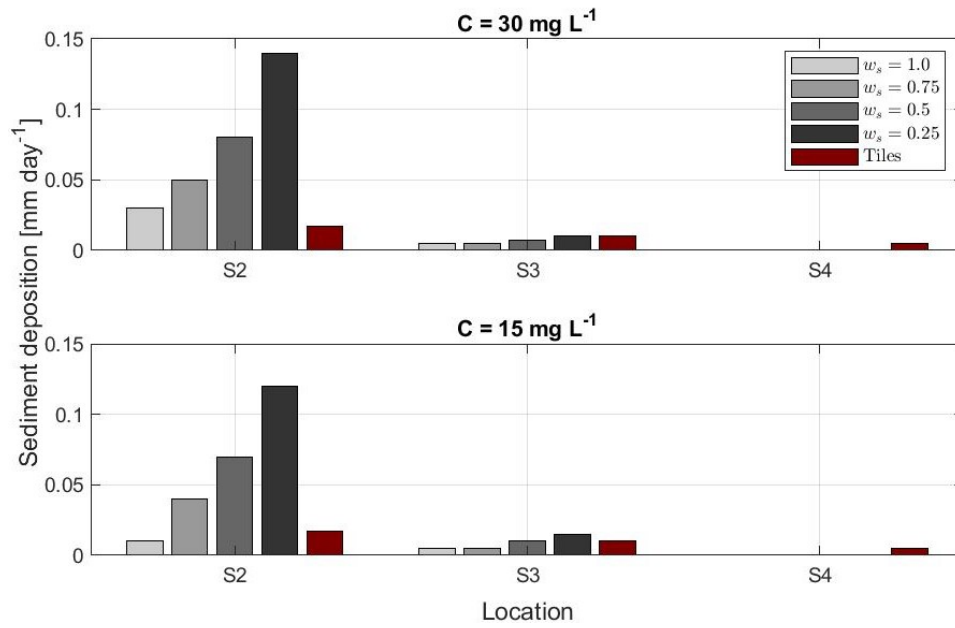


Figure 43: Observed and modelled sediment deposition for different suspended sediment concentrations and settling velocities (S-transect)

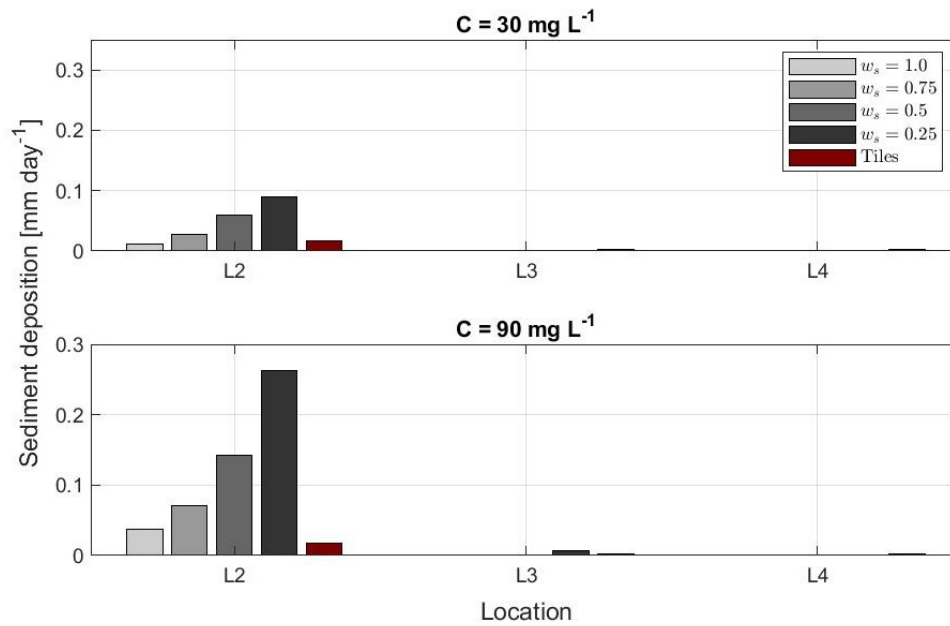


Figure 44: Observed and modelled sediment deposition for different suspended sediment concentrations and settling velocities (L-transect)

5.1.4 Summary calibration

Table 12 summarises final calibrated parameters, as well as the parameter set-up for the scenarios. Similar Manning coefficients, discharge properties and settling velocities are chosen for comparative reasons, these choices are further elaborated in chapter 6.

Table 12: Overview of the calibration results and the scenario run set-up. Subscripts 'S' and 'L' indicate the transects.

Calibration	Parameter	Value	Unit
Flow velocities	n	0.02	$s/m^{-1/3}$
	Q_{max}	1750	m^3/s
	Q_{base}	350	m^3/s
Sediment deposition	$C_{discharge,S}$	15	mg/l
	$C_{discharge,L}$	30	mg/l
	w_s	1	mm/s
Scenarios			
1. Reference scenario	Q_{max}	1750	m^3/s
	Q_{base}	350	m^3/s
	C_S	15	mg/l
	C_L	30	mg/l
2. River flood	Q_{max}	2670	m^3/s
	Q_{base}	1690	m^3/s
	C_S	300	mg/l
	C_L	300	mg/l
	Δh	2	m
3. Low flow	Q_{max}	1400	m^3/s
	Q_{base}	10	m^3/s
	Δh	0	m
	$C_{S,L}$	10	mg/l

5.2 Validation

After the model was calibrated, additional model runs were executed to validate the skill of the models in predicting the flow velocities during neap tides. Validation of the models comprised three days (figure 36). The quality of each of the validation simulations was assessed similar to the assessment of the calibration runs. Figures 45 and 45 show the outcome of the validation run for the S- and L-transects. The MA for the S-transect appears to be unsatisfactory (MA = 0.45). Alternating flood tides are significantly underestimated. Also, the timing of every other neap tide is off by multiple hours. In addition to the previous, during these tides the ebb flow velocities are also underestimated. The L-transects appears to be a satisfactory fit (MA = 0.59) the shape and timing of the velocity profiles are more or less similar. Model accuracies for the comparison of the flow velocities for the individual validation runs were lower than for the calibration runs for both models.

The lack of predicting capabilities for both models during neap tides can partially be attributed to the timing of the velocity profiles with respect to rise and fall of the tides. This is further discussed in chapter 6. Despite the unsatisfactory result of the S-transect, this study continues with the calibrated model. When comparing the low flow conditions and flood event to the reference situation, the timing becomes of less importance.

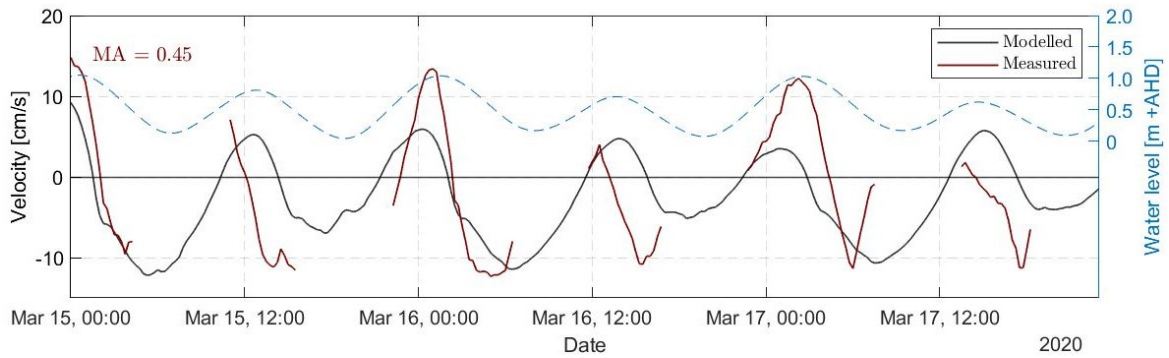


Figure 45: Observed flow velocities and modelled flow velocities during the calibration run for the S-transect. The model accuracy is plotted in the upper left corner.

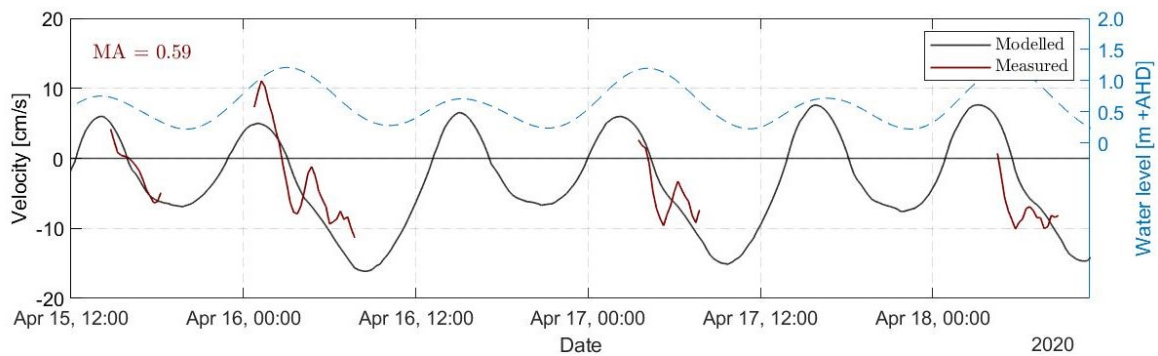


Figure 46: Observed flow velocities and modelled flow velocities during the calibration run for the S-transect. The model accuracy is plotted in the upper left corner.

5.3 Scenario results

This section presents the results of the scenarios. Three different river flow scenarios were executed in order to determine the impact of seasonal variations. The duration of these runs is 10 days, with one day used for spin-up. First, the modelled hydrodynamics are shown, and this section continues with the morphodynamics for each scenario.

5.3.1 Hydrodynamics

Short transect

Figure 47 show the modelled flow velocities at S1 to S3 for all three scenarios during spring and neap tides. In this figure the water levels during the reference and low flow scenario are shown. The water level for the flood scenario is constantly 2 m + AHD and not visualised. Negative flow velocities indicate, in line with previous velocity analysis, a seaward directed current. Positive values are interpreted as landward directed currents. The results for the entire time-frame are shown in figure 60 in Appendix C.

First, the reference situation, as calibrated, is visualised with a black line in figure 47. The reference situation shows during spring tides a relative stronger flood tide compared to the ebb tide at S1, and this is more pronounced at S2. Ebb flow seems to be dominant at all stations. S3 shows during inundation constantly a seaward directed current. This could be due to local variations in bed level, or that S3 is inundated with water originating from the discharge boundary. Velocities range at S1 range between 12-15 cm/s (spring) and 5-12 cm/s (neap). At S2 they range between 2-4 cm/s (spring) and 1-3 cm/s (neap). S3 generally has velocities of around 1 cm/s .

The low flow scenario is set-up with a relatively small base and maximum discharge (e.g. 10 and 1400 m^3/s), and visualised with the green line in figure 47. The low flow scenario shows distinctive differences compared to the reference situation. First, larger flood tides are modelled at S1 (+ 4 cm/s) and S2 (+ 2 cm/s) for spring neap tides, while S3 shows overall a decrease in velocities (- 0.5 cm/s). In contrast to the increase during flood tides, this scenario shows a significant decrease during ebb tides at S1 and S2 with the same order of magnitude. With lower discharges imposed on the boundary, the tides are being suppressed with less force, and therefore give shape to the hydrodynamics within the domain. Also, the low scenario with an almost negligible discharge, shows a clear tidal asymmetry (strong inflow and weak outflow). A possible explanation for this can be that the energy loss due to the vegetation and bottom friction becomes more relevant for the determination of the velocity profile. Finally, the ratio of the flood and ebb phase shows a clear difference compared to the reference situation as shown by the moments in slack tide. The duration of the flood phase increases, while the duration of the ebb phase decreases.

In figure 47, the flood scenario is shown with a red line. Some observations can be made about the effects of an increased river discharge. First, flow velocities at S1-3 are in the same order of magnitude compared to the other two scenarios. The shape however is substantially different from previous discussed runs. S1 and S2 show similar results, with nearly all flow being directed seaward. Where there were multiple peaks in the velocity profile in previous scenarios, this scenario shows a smooth line almost identically shaped as the imposed discharge boundary. This can be attributed to the fact that the discharge boundary is the only boundary condition that affects the flow velocities within domain, since the seaward boundary is a constant water level. An interesting observation can be seen at S3, and to a certain degree at S2. These sub-figures show the presence of landward directed flows. This is explained by the occurrence of an eddy within the system during these conditions, which is shown in Appendix D. This eddy is more pronounced during spring tide, compared to neap tide.

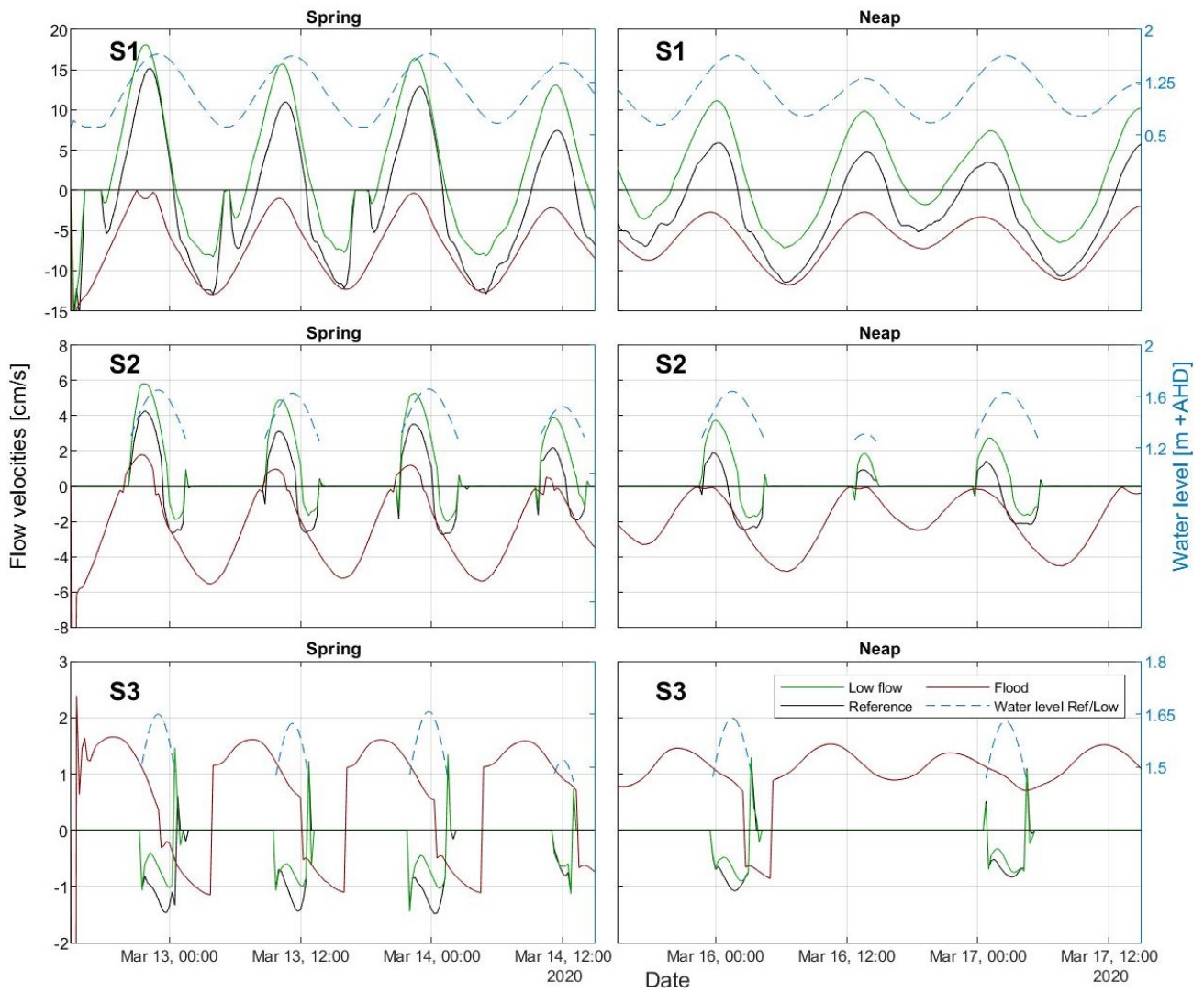


Figure 47: Modelled flow velocities at S1-3 for the three scenarios. The water levels plotted correspond with the reference/low flow scenario. Water levels during the flood scenario are constantly 2 m + AHD.

Long transect

The hydrodynamics of the L-transect model are shown in figure 48. The results for the entire time-frame are shown in figure 61 in Appendix C

First, the reference scenario shows that flow velocities at L1 typically range between 12-27 *cm/s* (spring) and 6-15 *cm/s* (neap). At S2 they range between 4-6 *cm/s* (spring) and 2-5 *cm/s* (neap). L3 appears to be barely inundating, and thus the flow velocities are below the 3 *cm/s*. The calibrated reference scenario displays a explicit asymmetry between the flood and ebb tides. At L1 and L2, the ebb tides are during spring tides almost twice as large compared to the flood tides. This is less pronounced during spring tides at L2 and all neap tides, but still noticeable. L3 barely inundates during both spring and neap tides. Here, all currents are seaward directed, which again can be attributed to local variations in bed level, or that S3 is inundated by river discharge.

The low flow scenario shows comparable results as observed at the S-transect model. At L1, ebb tides become slightly larger while velocities during flood tides decrease substantially. The turnaround of ebb-dominance to flood-dominance, as seen at the S-transect, is only partly visible in this figure. L1 and L2 remain ebb-dominant during spring tides, while L1 and L2 show a slight flood dominance during neap tides. An explanation for this could be the choice of the time frame. Figure 36 tells us that the the lowest water levels, and thus the largest negative discharges, are not within the time frame of the scenario runs. The turnaround of the tide-dominance is therefore not excluded from occurring, but it is not visible within these results. The L-transect shows, in line with the S-transect, an extended flood phase and reduced ebb phase implying that the tidal boundary becomes more defining regarding the hydrodynamics.

The flood scenario shows, largely in line with the S-transect model, a velocity profile that corresponds with the shape of the variable discharge. Near L1 during spring tides, seaward directed flow velocities show an increase of 10 *cm/s*, on the other hand, the flood velocities become negative and become around 7 *cm/s*. During neap tides the velocity profile is again entirely negative, meaning a seaward direction, and their magnitude fluctuates between the 25 and 9 *cm/s*. The magnitude of flow velocities vary between 17 *cm/s* seaward directed and 2 *cm/s* landward directed during spring tides. Neap tides waver between 12 and 4 *cm/s*. In the bottom right figure it appears that a river flood results in a constant inundation at L3, as opposed to normal conditions when no inundation takes place. On the contrary to the S-transect, no eddy is observed within the domain. The small bumps at L3 and L2 during spring tides could indicate a small local eddy near the station, this is however not visible within the domain.

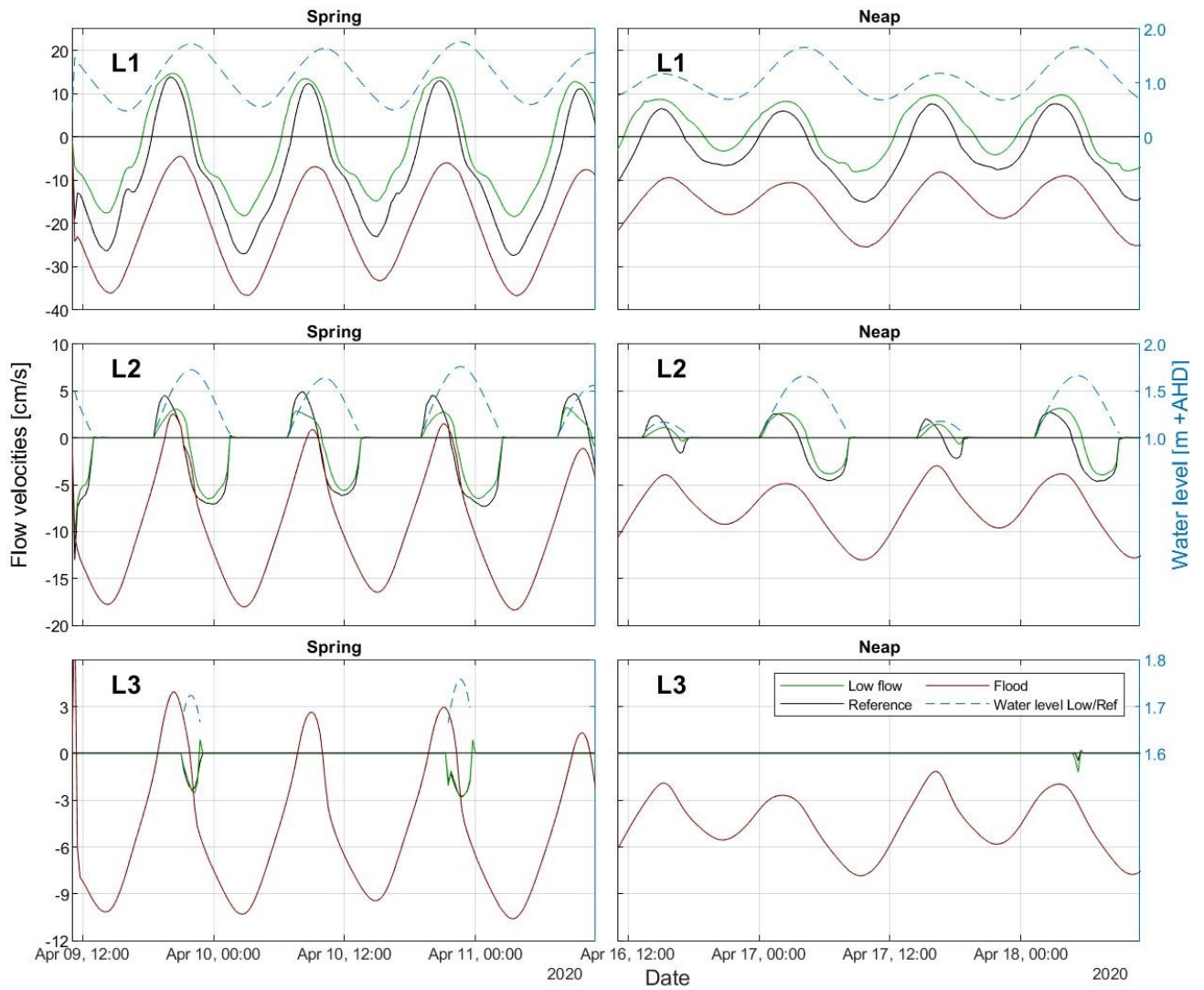


Figure 48: Modelled flow velocities at L1-3 for the three scenarios. The water levels plotted correspond with the reference/low flow scenario. Water levels during the flood scenario are constantly 2 m + AHD

5.3.2 Morphodynamics

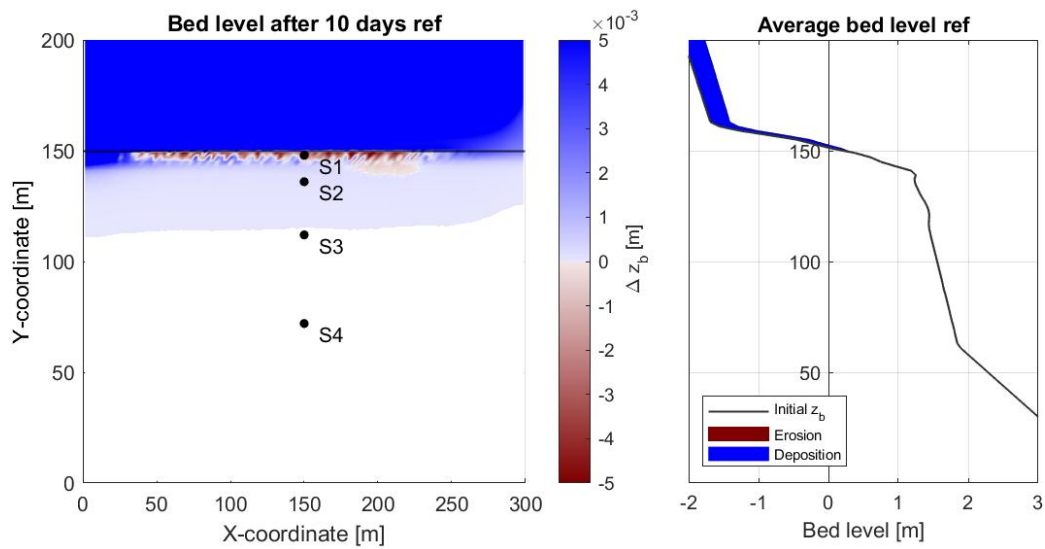
The presented hydrodynamics influence the sediment dynamics and morphology of the system. This chapter will analyse the morphological changes as a result of the scenarios. Figures 49 and 51 show on the left hand side the deposition and erosion differences Δz_b across the domain. All locations as well as the forest fringe are added to the figures. The right hand plots show the average (initial) bed level between $x = 100$ and $x = 200$, in order to get rid of any disturbances near the domain boundaries. Gradients in erosion and deposition in this plot are multiplied with a factor 15 for visibility.

Short transect

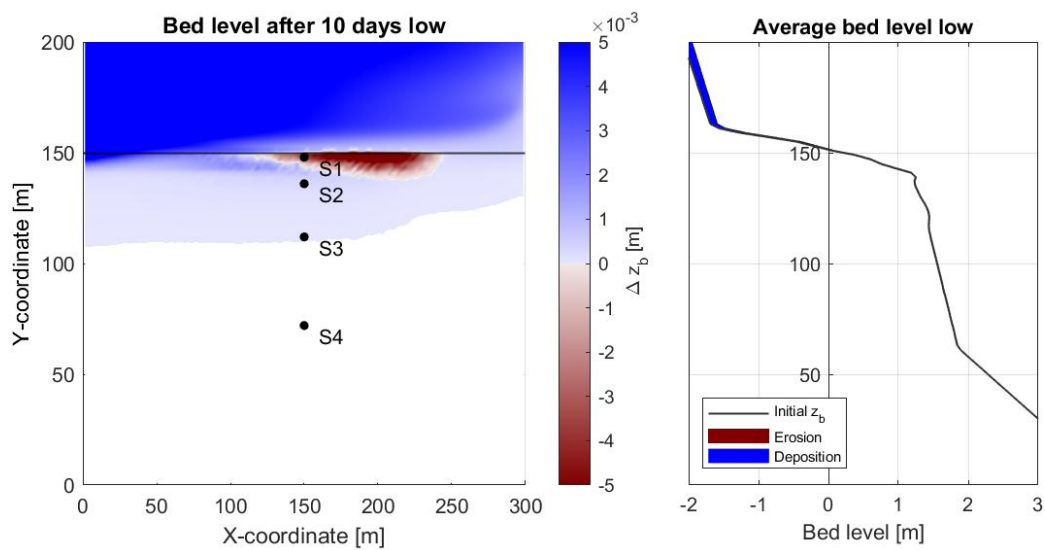
In figure 49a the morphodynamics for the reference scenario can be seen. Deposition gradients across the domain are largest in the river and near S1, where deposition rates up to 2 mm/day are observed for the latter. Inland at S2, deposition is relatively small ($< 0.02 \text{ mm/day}$), and sediment is not deposited further into the forest than $y = 115$ before S3. Secondly, this figure suggests that a certain degree of erosion is taking place at the border of the fringe near S1. Coincidentally, this is also where the initial bed layer thickness becomes zero. This, in combination with the steep slope at the fringe, results in erosion gradients. The degree of erosion does not exceed 0.5 mm/day .

In figure 49b the morphodynamics for the low flow scenario can be seen. Inland deposition rates are around 0.03 mm/day near S2, sedimentation is not observed further than $y = 110$, with a negligible amount of deposition at S3. This means that during low flow conditions, the sediment is carried slightly further into the forest compared to the reference situation. This is likely due to the increased flood velocities, and decreased ebb velocities. The lower ebb velocities could potentially result in less re-entrainment of sediments, thus explaining the observed deposition. These results show that the limited supply of sediments does not affect the sediment deposition within the mangrove. Again, erosion is occurring near the boundary of the initial bed thickness at $y = 150$. This is due to the relatively strong ebb-flow, as shown in figure 47, eroding the mudflat.

In figure 49a the results of the flood scenario are visualised. Significant rates of deposition can be seen, where rates almost exceed 60 mm/day for the river and mudflat. Rates of 10 mm/day are modelled for S1, while near S2 and S3 have deposition rates of 5 mm/day and 0.4 mm/day . The observation point at S4 gives a deposition rate of zero, but if the x-coordinate were to be chosen otherwise ($x = 50$ or $x = 275$), then a deposition rate of around 0.1 mm/day is found. The limit of where sediments are deposited during flood conditions lies at $x = 60 \text{ m}$, which is coincidentally where the elevation profile becomes the same height as the imposed water level of $2 \text{ m} + \text{AHD}$. This scenario thus allows sediments to travel up to 60 meter further into the forest compared to the previous scenario's. Finally, the deposition gradients in the along-river direction, shows a sinusoidal function. This is attributed to the observed eddy which is visualised in Appendix D.

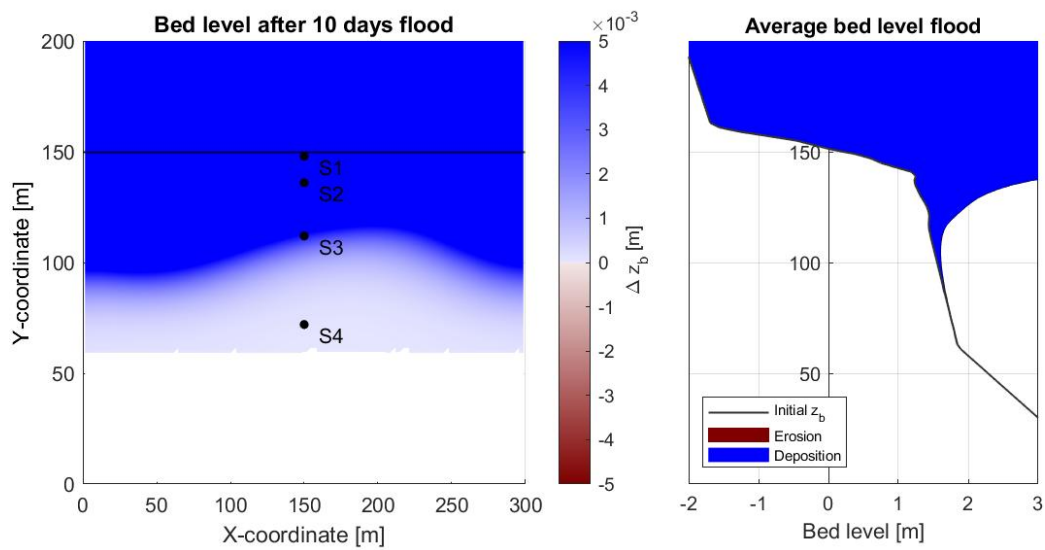


(a) Reference scenario



(b) Low flow scenario

Figure 49: Degree of deposition and erosion gradients across the area of interest S-transect (left). The black line indicates the location of the forest fringe. Red indicates erosion while blue indicates deposition. The right plot shows the average bed level profile after the run (between $x = 100$ and $x = 200$). Amounts of erosion/deposition are multiplied with a factor 15 for visibility.



(c) Flood scenario

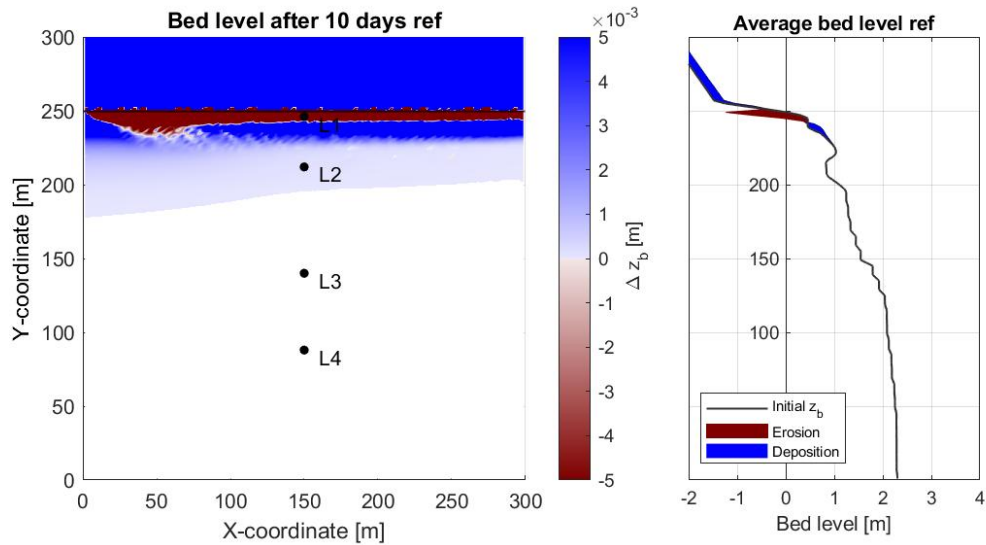
Figure 49: Degree of deposition and erosion gradients across the area of interest S-transect (left). The black line indicates the location of the forest fringe. Red indicates erosion while blue indicates deposition. The right plot shows the average bed level profile after the run (between $x = 100$ and $x = 200$). Amounts of erosion/deposition are multiplied with a factor 15 for visibility. (cont.)

Long transect

In figure 50a the results of the morphodynamics after 10 days are visualised. The foreshore, where L1 is located is eroding with a rate of 1.5 mm/day . On the contrary, sediment is being deposited at L2 in a rate of 0.03 mm/day . The limits of sediment deposition are at the western boundary near $y = 175$ with a rate of 0.01 mm/day . Sediment travels less far into the forest near the eastern boundary ($y = 205$). When averaged between $x = 100$ and $x = 150$, deposition occurs around 60 meters from the forest fringe, which is significantly further compared to the S-transect (35 m). Compared to the S-transect, larger deposition rates are observed in the first 20 meters inland from the fringe. Comparable with the S-transect, these results also show a strong erosion near the fringe, with a patch near $x = 50$ as most significant. This patch is a result of the strong ebb-tides, as visualised in 48. Since this erosion is near the edge of the domain, it is not taken into account in the right-hand plot.

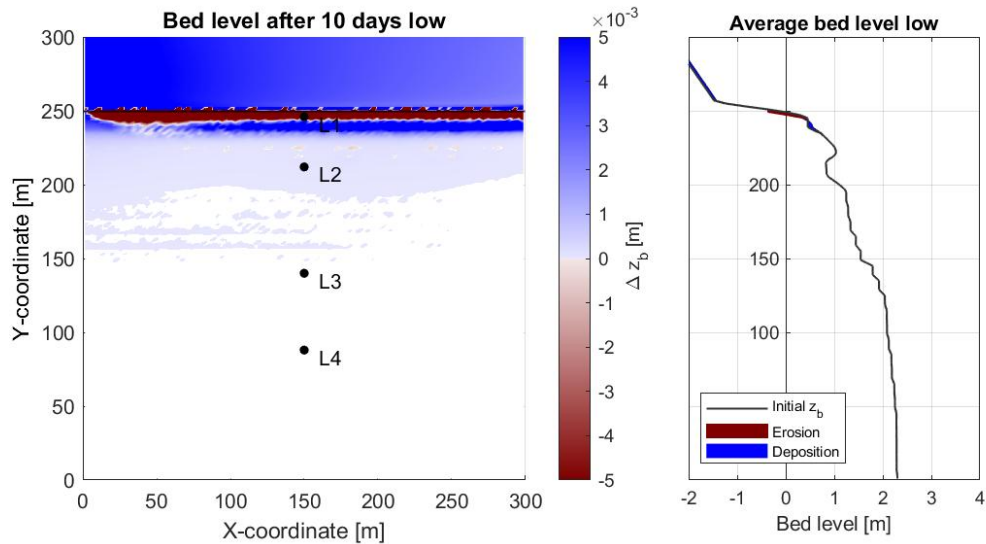
Figure 51a shows the result after 10 days of low flow. The erosion near L1 results in 1.1 mm/day , which is comparable with the reference situation. A negligible amount of sediment is deposited near L2 (0.003 mm/day). Despite the lower depositions near the L1 and L2, this figure shows that the suspended sediments are able to travel further into the forest since the limit of deposition lies around $y = 150 \text{ m}$. This can be attributed to the difference in ebb flows, which are substantially lower compared to the reference situation, thus enabling the sediments to settle. The patch of erosion near the fringe at $x = 50$ is still present, but less pronounced due to the lower ebb velocities (figure 48).

Figure 51b shows the gradients in sedimentation and erosion after the flood scenario. L1 is on the contrary to S1 eroding with a rate of 10 mm/day , which is almost 8 times more compared to the reference and low flow scenario. As the right-hand plot of 51b shows, significant volumes of sediment is being transport and deposited far into the forest. Rates of sedimentation are at L2 and L3 respectively 11 mm/day and 0.8 mm/day . The limit of sedimentation is uniformly distributed in the along-river direction and lies at $y = 130$, coinciding with the elevation profile intersecting $2 \text{ m} + \text{AHD}$. This means that during flood conditions, sediment can travel around 80 meters further into the forest compared to the reference situation. The erosion observed at the eastern boundary between $y = 225$ and $y = 250$ is likely a discontinuity within the model and corresponding boundary condition. Larger flow velocities during spring tides are observed within this region. This patch does not have consequences for the results of the model, since the eroded sediment is likely to have flowed out the domain and not returned due to the constant positive discharge.

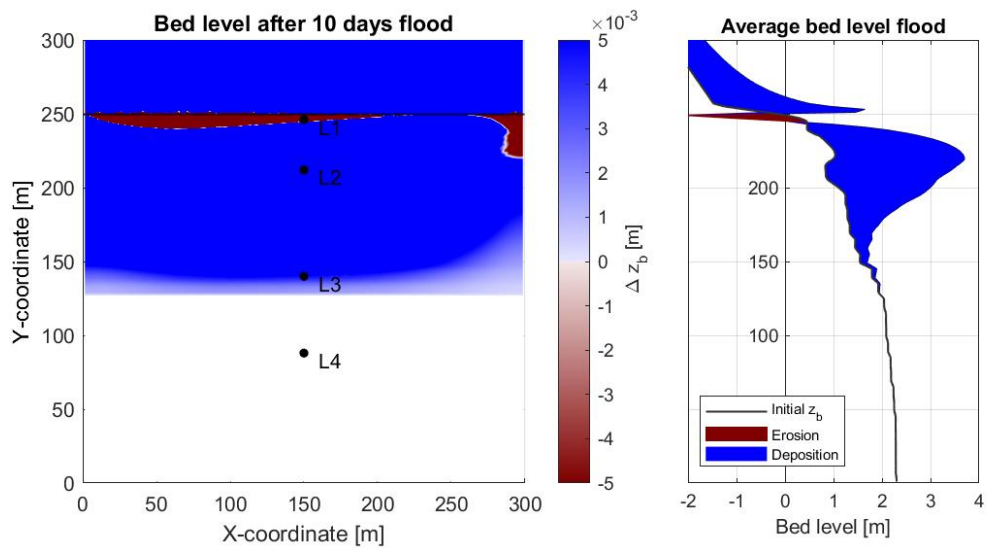


(a) Reference scenario

Figure 50: Degree of deposition and erosion gradients across the area of interest L-transect (left). The black line indicates the location of the forest fringe. Red indicates erosion while blue indicates deposition. The right plot shows the average bed level profile after the run (between $x = 100$ and $x = 200$). Amounts of erosion/deposition are multiplied with a factor 15 for visibility.



(a) Low flow scenario



(b) Flood scenario

Figure 51: Degree of deposition and erosion gradients across the area of interest L-transect (left). The black line indicates the location of the forest fringe. Red indicates erosion while blue indicates deposition. The right plot shows the average bed level profile after the run (between $x = 100$ and $x = 200$). Amounts of erosion/deposition are multiplied with a factor 15 for visibility. (cont.)

6 Discussion

In this study the effects of mangrove width on the hydro- and sediment dynamics in South Ballina's mangrove system was investigated. The first part of this study consisted of a field campaign, followed by a model study. This chapter starts with discussing the field data results. Next, the set-up and results of the modelling part are discussed. Finally, the limitations and recommendations of this study regarding the mangrove system are examined.

6.1 Effect of mangrove width on mangrove dynamics

The goal of the executed fieldwork was to obtain quantitative data about the two transects, in order to accurately assess the impact of mangrove width on the hydrodynamics and morphodynamics.

6.1.1 Hydrodynamics

The current velocities measured at both transects typically ranged between 0.05 and 0.15 *cm/s*, and are in line with previous mangrove studies by e.g. [Van Santen et al. \(2007\)](#) and [Horstman et al. \(2013a\)](#). The tidal in- and outflows clearly showed an asymmetrical pattern during spring tides: at S1 the flow is more flood-dominant with higher velocities during flood tides and a more sluggish flow was identified during subsequent ebb tides. L1 predominantly showed an ebb-dominance, where the outflow of the tides was of a higher velocity. During neap tides, the currents at S1 appeared to be alternating between ebb and flood dominance. Tides at L1 became entirely ebb-dominant, which implied that no reversal of flow occurs near this transect. Thus, the forces generated by the tides which 'push back' the river flow, are being suppressed by the river's discharge. All observed differences in flood or ebb dominance can be attributed to the estuarine location and orientation of both transects, and not to the difference in mangrove width. First, the L-transect is located 3 km further upstream, which affects the tidal back-push. Secondly, the width of the river is significantly smaller near the L-transect compared to the S-transect (350m to 550m) possibly resulting in higher flow velocities, and thus more momentum, within the river stream. Lastly, figure 8b shows the presence of sandbanks and trainer walls near the S-transect, which could guide the river's discharge through the northern part of the river and thus causing less obstruction to the rising tides through the southern part of the river, resulting in larger flood flow velocities. This possible flow pattern is visualised in figure 65 in Appendix E.

The direction of flood tides at L1 and S1 also showed variations, namely; at L1 the flow is more or less parallel towards the main channel; at S1, the flood tide enters the forest under a 45° angle. This can be attributed to the relative position of the fringe with respect to the dominant flow direction in the estuary. The fringe of S1 is at an angle of around 20° towards the river's stream, which leads to a more cross-shore directed inflow compared to L1. Also, directly downstream of the S-transect, the Richmond River bends towards the estuary's mouth thus resulting in a flow parallel towards the transect. The L-transect is located perpendicular relative to the main channel and therefore the landward directed flow velocities are lacking. The results thus suggest that inundation of this transect is occurring through sheet-flow entering the forest upstream or downstream of the transect rather than flows directly across the local forest fringe.

6.1.2 Morphodynamics

During low tides, Suspended Sediment Concentration (**SSC**) samples were taken by walking into the river and filling the bottles by hand. Disturbing the near bed sediment through this method is very likely, even when taking a small 'rest' period into account in order to let the sediment settle again. Sampling during high tide was done by boat, where the arrival speed was minimised to not disturb the sediment. Samples showed low variance which indicates a high accuracy of the sampling method. Measured **SSC** typically ranged between the 30 and 90 mg/l at the L-transect, while the S-transect ranged between 10 and 40 mg/l . [Hossain et al. \(2001\)](#) found in their study near the estuary's mouth an concentration of not more than 30 mg/l during normal flow conditions. On the contrary, the study by [Adame et al. \(2010\)](#) found **SSC**'s of around 117 mg/s in similar rivers (e.g. semi diurnal, low tidal range, 'extreme late summer') in Southern-Queensland. This difference is attributed to the higher flow velocities observed by [Adame et al. \(2010\)](#) ($\approx 0.8m/s$). Larger concentrations were found during low tides, implying a mostly fluvial origin of the estuary's sediment. The difference between both transects is probably due to the location of the turbidity maximum within the estuary, which is likely to be situated upstream of the S-transect. Previous paragraph already stated the relation between the tides and river discharge, but it appears that the same interaction is occurring with regards to the sediment rich Richmond River and sediment poor tides. Another reason for the difference in **SSC** is the width of the river, providing the river with a greater hydraulic radius, resulting in lower flow velocities and settlement of the sediments. This is also supported by the sandbanks in front of the S-transect as shown in figure [8b](#), suggesting excessive sedimentation within the estuary.

Clear differences regarding the grain size distribution at both transects were detected. This can be attributed to spatial segregation of coarse and fine sediments by the meandering Richmond River, usually with the most coarse material in the outer bend. Since the L-transect is located in an inner bend of the Richmond River, and the S-transect is more or less located in the outer bend of the river (see figure [8b](#)), this is the most logical explanation.

The observed deposition rates by the tiles showed a cross-shore decrease with the highest rates found near the forest fringe and very low deposition in the forest. The rates and distribution are in line with the findings of [Horstman et al. \(2017\)](#). The repetitive tiles showed small variations, which can be attributed to the spatial variability of the soil, and the self-scouring of small channels during ebb-tides ([Wolanski, 1992](#); [Horstman et al., 2015](#)). Pressure gauge data showed the lack of inundations of S3 and L3. In addition, both models showed no deposition at these locations, which is contradicting with the measured deposition rates at the same locations. An explanation for this is that heavy rainfall during the study period could have disturbed the sediment which led to deposition on the tiles. To get a more comprehensive insight in the deposition rates throughout the spring-neap cycle, samples should also be taken during neap tides and preferably additional moments. Lengthening the sampling period of the tiles would also increase the accuracy of the measurements, since short term variations in **TSS** and flow velocities would be smoothed.

As expected, the rates of the **RSET**'s are not in line with the sediment deposition rates of the tiles. This is due to multiple reasons. First, since the rods of the **RSET**'s are anchored at an depth of 10 meters it accounts (to a certain degree) for the compaction of the substrate. Second, the tiles

only sampled during multiple spring tides. By combining the results from the tiles, both reference models and the RSET's some trends can be seen. They all point in the direction that the front of both transects (S1-2 and L1-2) are accreting due to the deposition of sediments. Also, during normal conditions, locations that are more inland (S3-4 and L3-4) lack accretion which leads to a decrease in bed elevation likely due to the compaction of the soil. The model study also showed a difference in deposition in the first 20 meters inland from the fringe. Given that Mean Sea level (MSL) is around 1 m + AHD, it can be seen in figures 49a and 50a that during a water level corresponding with MSL, inundations occur up to 25 meters inland from the fringe at the L-transect. On the contrary, the elevation profile allows only inundations up to 10 meters inland from the fringe at the S-transect, thus explaining the sedimentation patterns.

Summarising, all observed and modelled differences in hydro- and morphodynamics during normal conditions between both transects are explained by the estuarine location and orientation, the biogeophysical settings and the elevation profile, and not the difference in mangrove width.

6.2 Effect of variations in river discharge characteristics on the behaviour of the mangrove system

Two numerical models which inherently differ in mangrove width were set-up based on field observations. These models set-up was changed to mimic conditions during high and low flow conditions to explore the mangroves' response to variable conditions.

During low flow conditions, both models showed a turnaround from ebb-dominance towards flood dominance throughout the spring-neap cycle. This can have multiple implications for the dynamics within both system. First, a flood dominance can induce a residual accumulation of water in the estuary by temporarily pushing the river's low discharge back, resulting in a net input of suspended sediment in the estuary Hossain et al. (2001). Due to the higher flood flow velocities that are modelled, suspended sediments can be transported further into the forest. However, this did not affect the amount of deposition within the forest compared to the reference situation. This is due to the fact that during low flow conditions, the available sediment is lower compared to the reference situation.

Modelled flow velocities during flood conditions showed clear differences between both transects, and can be linked to the differences in flow domain. A larger flow domain at the S-transect will lead to relatively lower velocities within the stream and excessive sedimentation within the river stream and foreshore (figure 49c). Contrasting, the relative smaller flow domain at the L-transect has resulted in larger flow velocities in the river, not allowing the large of amounts of sediment to settle. It appears that the suspended sediments are carried in large volumes into the transect, where they deposit (51b). The L-transect shows inundations up to 120 m of the forest fringe, while the S-transect is inundated up to 90 m from the forest fringe. Combining this with the large depositions, it is suggested that the mangrove acts as a traditional floodplain (Teo, 2010). Floodplains in general are natural features that provide floodwater storage and conveyance to reduce flood velocities and flood peaks, and curb sediments Wolanski and Ridd (1986); Teo (2010). In other words, the Richmond River has a limited capacity for water and sediment and when this is exceeded, flooding of the adjoining mangroves as floodplain occurs, which then act to store this water and sediment. The hydrodynamic and morpholog-

ical processes on floodplains are associated with the floodplain characteristics e.g. surface topography, vegetation and the varying quantity and size of available water and sediment [Teo \(2010\)](#). This study investigated a minor flood with a return period of one in two years. It is however likely that there is a limit towards the magnitude of the flood on one hand, and the amount of deposition in the forest on the other hand. In the case of a significant larger flood, flow velocities in the mangroves are likely to be higher, thus disabling sediments to settle. The L-transect already showed erosion during the flood scenario, which could indicate that the limit regarding river discharge is not far off. This inverse proportion between the flood magnitude and the sediment trapping capacity is also acknowledged by [Hossain et al. \(2001\)](#).

It is acknowledged by studies (e.g. [Kirwan and Megonigal \(2013\)](#); [Willemsen et al. \(2016\)](#)) that coastal squeeze can reduce the inter-tidal area, depleting the mangroves from the ready supply of sediments upon which their survival depends. From a mangrove perspective, the findings in this study thus strongly indicate the need for a-periodic flood events to occur, in order for higher elevated parts of the mangrove forest to inundate and accrete.

During all scenario runs significant erosion took place near the fringe. There are multiple explanations for this occurrence. It is most likely that the set-up of the initial homogeneous sediment bed layer thickness is not optimal. From $y = 0$ to $y = 250$ (L) and $y = 150$ (S), the sediment layer has a thickness of 5m, from the latter cross-shore locations to the northern part of the domain the thickness has a thickness of 0m. Thus, it is likely that an instability in the model has occurred, which can explain this erosion. On the other hand, the elevation profile obtained in the field showed a steep decline after the fringe, this may indicate that the bathymetry in the field is not yet in equilibrium.

6.3 Limitations

This section describes limiting factors in the set-up of both models and the subsequent calibration and results.

6.3.1 Model set-up

First, both models are defined as a simple square with a constant slope in foreshore, while the local situation and bathymetry are more complex. These variations in bathymetry affect the flow and wave patterns and could provide other results or new insights in the system's behaviour. The river depth profile that is implemented in DFM is somewhat questionable, mainly due to the presence of geomorphological attributes such as sandbanks, rock walls near the ferry and the breaker walls at the S-transect. In figure [8b](#) multiple sandbanks can be observed, indicating spatial variability in the currents of the River. Also, a submerged barrier is located 200 meters directly in front of the fringe. This barrier lies around 0.5 meters below **MSL**. The presence of the barrier in addition to the fact that the fairway is occasionally being dredged makes it difficult to estimate the direction of currents by looking at aerial pictures. Likewise, the limits and location of the discharge boundary could be argued. Preliminary runs showed the impact of this boundary set-up on the magnitude and direction of the modelled flow velocities. For the L-transect this can be physically explained by the fact that the

transect is located in the inner bend of the Richmond River. The open boundary has the same width as the river, but the majority of the flow will lie within the outer bend of the river. However, best results were obtained when the chosen discharge boundary for the L-transect starts at the upper part of the domain and ends at the forest fringe ($\Delta y = 350m$). Implementing an accurate representation of bathymetry and geomorphology could yield different flow patterns and higher flow velocities near the fringe, resulting in more estuarine sediment flowing into the forest.

Preferably, the flood scenario is set-up with a combination of a water level boundary condition and discharge boundary on the western side of the domain, and a tidal boundary on the eastern side of the domain. However, DFM does not allow a combination of a discharge boundary condition and water level boundary condition imposed on the same computational cells. This led to the set-up of a discharge boundary on the western boundary, representing the flood velocities, and a constant water level on the eastern boundary representing the increased water levels due to the flood. By implementing a sinusoidal shape into the discharge boundary, the effect of the tidal back-push is mimicked. Due to the small size of the domain in along-river direction, this is a valid assumption. But, the accuracy of this modelling limitation could not be verified. Also, in reality there could be a discharge threshold after which the tidal back push is completely nullified, and the discharge boundary becomes constant.

6.3.2 Calibration and validation

Calibrating both models accordingly with the same input parameters appeared to be rather hard. In order to accurately represent the shape, direction and magnitude of the flow velocities in L1 and S1 some assumptions had to be made.

In section 5.1, the results regarding the calibration are presented. The choice for $Q_{max} = 1750 m^3/s$ ($Q_{base} = 350 m^3/s$) appeared to be the best fit for the L-transect. But, this did not result in the best model accuracy (MA) for the S-transect. A choice is made based on the cumulative MA of both transects. With this model choice S1 slightly underestimates the magnitude of the flood-tide. Increasing the calibration discharge to e.g. $2000 m^3/s$, would not yield more accurate results since the model would overestimate the x-component and still underestimate the y-component of the flow. The modelled deviation in the y-component arises due to the fact that the TCM only measures the top column, while DFM is depth averaged. A discharge of $1750 m^3/s$ seemed to be the best overall fit for the magnitude and shape of the velocity profiles. However, according to Hashimoto et al. (2006) and Hossain et al. (2001) this discharge almost corresponds with an a-periodic floods. It is not likely that during the fieldwork period of about 2 months, a constant flood discharge was present. The implication of this result, is that the model is being calibrated during river flood conditions, while a calibrated model during 'normal' conditions is desired. This result can also have an impact on other model parameters (e.g. discharge boundary conditions and sediment properties), which are likely to have different values under river flood conditions, compared to normal conditions. These implications are however unknown.

The calibration of the Manning's coefficient also yielded different best fits. Again, a choice is made based on the cumulative performance of both models, which was a value of ($0.02 s/m^{1/3}$). This value is in line with previous studies about mangrove modelling (e.g. Horstman et al. (2015); Willemsen et al. (2015); Lesser et al. (2004)). The choice for one Manning coefficient for both transects despite the

differences in substrate characteristics is done for comparative reasons. Also, drag forces can primarily be attributed to the pneumatophores and not the soil characteristics [Norris et al. \(2017\)](#). Since the pneumatophore count and characteristics near L1 and S1 were comparable, this appears to be a valid assumption. A side-note regarding the found discharge and Manning's coefficient should be placed. In reality, a higher Manning's coefficient in combination with a higher discharge would probably yield the same results regarding flow velocities. Although both found values agree with common values found in literature, this still remains a point of attention.

Models were calibrated for their deposition predictions at S2-4 and L2-4 during subsequent spring tides. Both models showed accurate predictions of the deposition at S2-4 and L2-4 with calibrated settling velocities and SSC's. Settling velocities were set at 1 *mm/s*, which is higher compared to modelling studies by e.g. [Willemssen et al. \(2016\)](#); [Horstman et al. \(2013b\)](#). Figures 16, 17, 47 and 48 show that S3 and L3 barely inundate during spring tides. And since the sediment computational threshold in DFM is 0.05m. This could affect the models performance regarding sedimentation or erosion predictions at these higher elevated parts of the model. Calibration of flow velocities and sediment deposition is performed during spring tides, due to the lack of data during neap tides. Fieldwork results showed significant differences in flow characteristics between spring and neap, which could lead to significant differences in deposition patterns during neap tides compared to spring tides. The model performance regarding the first is unknown.

Simulating flow velocities is proven to be successful for the L-transect with the obtained validation results. The validation for the S-transect proved to be unsatisfactory, where the performance lacked largely due to the estimation of the timing of the tides. Predictions were off for multiple hours, without a clear explanation. Figure 33 shows that there is a slight distortion of the UTide reconstruction and field observations, compared to observations at Byrnes Point. This could partly explain the delay in model prediction. Moreover, the inaccuracy could be due to a more complex flow pattern of the tidal wave in the field compared to the model, or due to variations in river discharge. Nevertheless, this is something that needs further attention in future studies.

6.4 Applicability

The numerical models have shown to be a useful tools to extend field-obtained data numerically. Both models are able to reproduce field-obtained flow velocities and deposition gradients well for spring tides. An significant advantage of these models is the formulation of a variable discharge boundary. In real-life systems, the complex interactions between rivers and tides often span multiple kilometres. These models allow the user to reduce the grids in along-river direction and thus reducing the complexity and run-time of the model. A side-note should be placed that the performance of the models is not known when the imposed sediment concentrations and salinity also become variable over time. Also, both models require limited input data in order to function properly. The models could therefore also be applied for analysis on different geometries and environmental settings.

7 Conclusions

The goal of this study is “*to gain insight in the morphodynamic response of two transect of different mangrove forest width, when considering multiple seasonal variations in forcing parameters*”. In order to achieve this goal, two research questions were defined. The conclusions will be given per research question.

7.1 The effect of mangrove width on the biophysical properties and interactions

The first research question is: “*What is the effect of mangrove width on the biophysical properties and interactions?*”

The flow velocities of both transects differ on both the magnitude, as well as the direction. The S-transect concluded to be more flood-dominant, while the L-transect primarily showed an ebb-dominance. This is explained by the difference in river width, the location of the transect within the estuary, the transect orientation with regards to the river and the presence of sandbanks and trainer walls near the S-transect. The direction of flow showed at the S-transect a more pronounced inland directed flood-tide. This is linked to the relative position of the fringe compared to main channel and thus the origin of the tidal wave as well as possible sheet-flow.

SSC were found to be larger during low tides compared to high tides, implying a mostly fluvial origin of the estuary’s sediment. The **SSC** also showed variations between the transects, with higher concentrations observed near the L-transect (10-40 *mg/l* (S), 30-90 *mg/l* (L)), and is attributed to the turbidity maximum within the estuary. Clear differences regarding the grain size distribution at both transects were detected which are due to spatial segregation of the meandering Richmond River. Long-term **RSET** data, combined with the model results and deposition tiles, showed that over the years the fringing locations S2 and L2 accrete. Also, locations that are more inland (S3-4 and L3-4) lack accretion during normal conditions, which leads to a decrease in bed elevation which is attributed to soil compaction. The model study explicitly showed that the elevation profile is the major driver in deposition patterns throughout the transects.

The results of the field campaign revealed that the effect of mangrove width on the biophysical properties and interactions is limited. The estuarine location, bio-geophysical settings and transect properties are concluded to be the major causes for the discovered differences between the two transects. The results from the model study regarding the effect of mangrove width on the biophysical properties and interactions remains inconclusive, since no clear comparison could be made. Many parameters between the two models differed, thus disabling a one to one comparison regarding the mangrove width.

7.2 The effect of mangrove width when seasonal variations are considered

The second research question is: “*What is the effect of mangrove width on the hydro- and morphodynamics, when variations in river discharge and sediment concentration are considered?*”

In addition to the field campaign, two accurate depth-averaged process-based numerical models were developed in Delft-3D Flexible Mesh (DFM), which showed decent estimations of flow velocities and deposition rates. The two models allowed for comparison of mangrove width by means of model simulations of variations in river discharge and fluvial sediment concentrations. During low flow conditions, both models showed a turnaround from ebb-dominance towards flood-dominance throughout the spring-neap cycle. This could lead to a temporarily accumulation of water in the estuary during the flood phase, resulting in a net accumulation of sediments in the river stream and foreshore. Also, the increased flow velocities enhance the sediment transport capabilities within the forest. But, during low flow conditions the fluvial sediment input is limited, and therefore the net deposition rates in the forest decreases.

Flood conditions will lead to larger velocities within the forest at the 'long' transect compared to the 'short' transect, and this is attributed to the limited width of the river in front of the long transect compared to the short transect. Despite the increase in flow velocities during a flood event, the mangroves are able to trap significantly more sediments compared to normal flow conditions. This is assigned to the large increase in fluvial sediment input compared to the reference situation. The model study also concludes that the Richmond River has a limited capacity for water and sediment and when this capacity is exceeded, flooding of the adjoining mangroves as floodplain occurs, which then act to store this water and sediment. This effect is observed to be larger at the L-transect compared to the S-transect, partly due to the width of the river, and partly due to the bathymetry of the transects.

The landward extent of the intertidal area at South Ballina's mangrove system is currently suppressed by a road, which limits the landward accommodation space for the mangroves. Combined with an expected rise in **SLR** in the future, this study strongly indicates the need for a-periodic flood events to occur, in order for higher elevated parts of the mangrove forest to inundate and accrete.

8 Recommendations

This study results in a number of recommendations. These recommendations are shown below, and concern additional fieldwork and modelling applications.

- *Additional fieldwork.* For a mechanistic understanding of the tidal routing of water and sediments through mangroves, additional field measurements are required to distinguish between the contributions of different environmental settings, such as the topography of the foreshore and river, vegetation and behaviour of the Richmond River throughout the year. Also, fluxes of sediments through the river, estuary mouth, forest fringe and inland locations are very valuable for a more quantitative comparison between the two transect regarding the morphodynamics. To obtain these sediment fluxes, velocity and SSC profiles in the river and near the forest fringe are required throughout a spring-neap cycle, but also on a more seasonal scale. Finally, substrate samples indicated that there is spatial variability in the sediment characteristics within the estuary. The next step would be to analyse the sediment and SSC properties for e.g. density or organic matter content. These aforementioned measurements also function as improvements regarding both models' performance.
- *Set-up of identical models differing in slope and width.* This study investigated the effect of mangrove width on the hydro- and morphodynamics. The two models that have been set-up are however varying over multiple parameters and therefore the answer to the main question remains inconclusive. Ideally, two identical models are used. These models should have a linear elevation profile, identical boundary conditions and foreshore bathymetry, and should only vary in slope and width.
- *Effect of magnitude floods.* The model has been run with a flood with a 2-year return period. Hossain et al. (2001) states that during a flood with e.g. a 5-year return period could prevent any sediment to settle due to flood-related flow velocities. The effect of the mangrove system regarding floods with a larger return period should therefore be investigated. The next step would then be to observe the initial response of mangroves after flood conditions. This can be achieved by increasing the run-time of the models, and to limit the duration of flood conditions during these runs.

References

- Adame, M. F., Neil, D., Wright, S. F. and Lovelock, C. E. (2010), 'Sedimentation within and among mangrove forests along a gradient of geomorphological settings', *Estuarine, Coastal and Shelf Science* **86**(1), 21–30.
- Akumu, C. E., Pathirana, S., Baban, S. and Bucher, D. (2011), 'Examining the potential impacts of sea level rise on coastal wetlands in north-eastern NSW, Australia', *Journal of Coastal Conservation* **15**(1), 15–22.
- APHA (2017), Standard Methods for the Examination of Water & Wastewater, Technical report.
- Balke, T., Bouma, T. J., Horstman, E. M., Webb, E. L., Erftemeijer, P. L. and Herman, P. M. (2011), 'Windows of opportunity: Thresholds to mangrove seedling establishment on tidal flats', *Marine Ecology Progress Series* **440**, 1–9.
- Balke, T., Swales, A., Lovelock, C. E., Herman, P. M. and Bouma, T. J. (2015), 'Limits to seaward expansion of mangroves: Translating physical disturbance mechanisms into seedling survival gradients', *Journal of Experimental Marine Biology and Ecology* **467**, 16–25.
URL: <http://dx.doi.org/10.1016/j.jembe.2015.02.015>
- Balke, T., Webb, E. L., van den Elzen, E., Galli, D., Herman, P. M. and Bouma, T. J. (2013), 'Seedling establishment in a dynamic sedimentary environment: A conceptual framework using mangroves', *Journal of Applied Ecology* **50**(3), 740–747.
- Bao, T. Q. (2011), 'Effect of mangrove forest structures on wave attenuation in coastal Vietnam', *Oceanologia* **53**(3), 807–818.
- Baptist, M. J. (2005), *Modelling floodplain biogeomorphology*, Vol. Dr.
- Best, S., Van der Wegen, M., Dijkstra, J., Willemsen, P. W., Borsje, B. W. and Roelvink, D. J. (2018), 'Do salt marshes survive sea level rise? Modelling wave action, morphodynamics and vegetation dynamics', *Environmental Modelling and Software* **109**(September 2017), 152–166.
URL: <https://doi.org/10.1016/j.envsoft.2018.08.004>
- Boone Kauffman, J. and Donato, D. C. (2012), 'Protocols for the measurement, monitoring and reporting of structure, biomass and carbon stocks in mangrove forests'.
- Borsje, B. W., de Vries, M. B., Hulscher, S. J. and de Boer, G. J. (2008), 'Modeling large-scale cohesive sediment transport affected by small-scale biological activity', *Estuarine, Coastal and Shelf Science* **78**(3), 468–480.
- Borsje, B. W., van Wesenbeeck, B. K., Dekker, F., Paalvast, P., Bouma, T. J., van Katwijk, M. M. and de Vries, M. B. (2011), 'How ecological engineering can serve in coastal protection', *Ecological Engineering* **37**(2), 113–122.
URL: <http://dx.doi.org/10.1016/j.ecoleng.2010.11.027>

-
- Bouma, T. J., Friedrichs, M., Klaassen, P., Van Wesenbeeck, B. K., Brun, F. G., Temmerman, S., Van Katwijk, M. M., Graf, G. and Herman, P. M. (2009), 'Effects of shoot stiffness, shoot size and current velocity on scouring sediment from around seedlings and propagules', *Marine Ecology Progress Series* **388**(May 2014), 293–297.
- Bryan, K. R., Nardin, W., Mullarney, J. C. and Fagherazzi, S. (2017), 'The role of cross-shore tidal dynamics in controlling intertidal sediment exchange in mangroves in Cù Lao Dung, Vietnam', *Continental Shelf Research* **147**(October 2016), 128–143.
URL: <http://dx.doi.org/10.1016/j.csr.2017.06.014>
- Bunt, J. S. (1996), 'Mangrove zonation: An examination of data from seventeen riverine estuaries in tropical Australia', *Annals of Botany* **78**(3), 333–341.
- Callaway, J. C., Cahoon, D. R. and Lynch, J. C. (2015), 'The Surface Elevation Table-Marker Horizon Method for Measuring Wetland Accretion and Elevation Dynamics', (June 2015), 901–917.
- Codiga, D. L. (2011), 'Unified Tidal Analysis and Prediction Using the UTide Matlab Functions', pp. 1–60.
URL: <papers2://publication/uuid/C87EF698-E7AE-4579-816B-4E71F22E56B4>
- Craft, C., Clough, J., Ehman, J., Jove, S., Park, R., Pennings, S., Guo, H. and Machmuller, M. (2009), 'Forecasting the effects of accelerated sea-level rise on tidal marsh ecosystem services', *Frontiers in Ecology and the Environment* **7**(2), 73–78.
- Dalrymple, R. A., Kirby, J. T. and Hwang, P. A. (1984), 'Wave Diffraction Due To Areas of Energy Dissipation', **110**(1), 67–79.
- de Groot, R., Brander, L., van der Ploeg, S., Costanza, R., Bernard, F., Braat, L., Christie, M., Crossman, N., Ghermandi, A., Hein, L., Hussain, S., Kumar, P., McVittie, A., Portela, R., Rodriguez, L. C., ten Brink, P. and van Beukering, P. (2012), 'Global estimates of the value of ecosystems and their services in monetary units', *Ecosystem Services* **1**(1), 50–61.
URL: <http://dx.doi.org/10.1016/j.ecoser.2012.07.005>
- de Vos, W.-J. (2004), 'Wave attenuation in mangrove Wetlands - Msc Thesis'.
- Deltares (2020a), '3D/2D modelling suite for integral water solutions: Delft3D Hydro-Morphodynamics User Manual', p. 214.
- Deltares (2020b), 'D-Morphology User Manual'.
- Draper, J. (2017), 'Assessing subtropical mangrove forest characteristics and biomass in Ballina, New South Wales'.
- Dronkers, J. (1986), 'Tidal asymmetry and estuarine morphology', *Netherlands Journal of Sea Research* **20**(2-3), 117–131.
- Duke, N. C. (1992), 'Mangrove floristics and biogeography', (January 1992), 63–100.

-
- Duke, N. C., Ball, M. C. and Ellison, J. C. (1998), 'Factors influencing biodiversity and distributional gradients in mangroves', *Global Ecology and Biogeography Letters* **7**(1), 27–47.
- Elfrink, B., Hanes, D. M. and Ruessink, B. G. (2006), 'Parameterization and simulation of near bed orbital velocities under irregular waves in shallow water', *Coastal Engineering* **53**(11), 915–927.
- Finlayson, C. M., Davis, J. A., Gell, P. A., Kingsford, R. T. and Parton, K. A. (2013), 'The status of wetlands and the predicted effects of global climate change: The situation in Australia', *Aquatic Sciences* **75**(1), 73–93.
- Friess, D. A., Krauss, K. W., Horstman, E. M., Balke, T., Bouma, T. J., Galli, D. and Webb, E. L. (2012), 'Are all intertidal wetlands naturally created equal? Bottlenecks, thresholds and knowledge gaps to mangrove and saltmarsh ecosystems', *Biological Reviews* **87**(2), 346–366.
- Furukawa, K. and Wolanski, E. (1996), 'Sedimentation in mangrove forests'.
- Furukawa, K., Wolanski, E. and Mueller, H. (1997), 'Currents and sediment transport in mangrove forests', *Estuarine, Coastal and Shelf Science* pp. 301–310.
- Giri, C., Ochieng, E., Tieszen, L. L., Zhu, Z., Singh, A., Loveland, T., Masek, J. and Duke, N. (2011), 'Status and distribution of mangrove forests of the world using earth observation satellite data', *Global Ecology and Biogeography* **20**(1), 154–159.
- Glamore, W. C., Rahman, P. F., Cox, R. J., Church, J. A. and Monselesan, D. P. (2015), 'Sea Level Rise Science and Synthesis for NSW NSW Office of Environment and Heritage' s Coastal Processes'.
- Hashimoto, T. R., Saintilan, N. and Haberle, S. G. (2006), 'Mid-Holocene development of mangrove communities featuring Rhizophoraceae and geomorphic change in the Richmond River Estuary, New South Wales, Australia', *Geographical Research* **44**(1), 63–76.
- Heumann, B. W. (2011), 'An object-based classification of mangroves using a hybrid decision tree-support vector machine approach', *Remote Sensing* **3**(11), 2440–2460.
- Horstman, E. M., Dohmen-Janssen, C. M., Bouma, T. J. and Hulscher, S. J. (2015), 'Tidal-scale flow routing and sedimentation in mangrove forests: Combining field data and numerical modelling', *Geomorphology* **228**, 244–262.
URL: <http://dx.doi.org/10.1016/j.geomorph.2014.08.011>
- Horstman, E. M., Dohmen-Janssen, C. M. and Hulscher, S. J. (2013a), 'Flow routing in mangrove forests: A field study in Trang province, Thailand', *Continental Shelf Research* **71**, 52–67.
- Horstman, E. M., Dohmen-janssen, C. M. and Hulscher, S. J. (2013b), 'Modelling tidal dynamics in a mangrove creek catchment in Delft3D', (3-4).
- Horstman, E. M., Dohmen-janssen, C. M., Narra, P. M. F., Berg, N. J. F. V. D., Siemerink, M. and Hulscher, S. J. M. H. (2014), 'Wave attenuation in mangroves : A quantitative approach to field observations', *Coastal Engineering* **94**, 47–62.
URL: <http://dx.doi.org/10.1016/j.coastaleng.2014.08.005>

-
- Horstman, E. M., Mullarney, J. C., Bryan, K. R. and Sandwell, D. R. (2017), 'Deposition gradients across mangrove fringes', *Coastal Dynamics* **8**(012), 1045–1046.
- Hossain, S. and Eyre, B. (2002), 'Suspended sediment exchange through the sub-tropical Richmond River estuary, Australia: A balance approach', *Estuarine, Coastal and Shelf Science* **55**(4), 579–586.
- Hossain, S., Eyre, B. and McConchie, D. (2001), 'Suspended sediment transport dynamics in the sub-tropical micro-tidal Richmond River estuary, Australia', *Estuarine, Coastal and Shelf Science* **52**(5), 529–541.
- Hutchings, P. and Saenger, P. (1972), 'Ecology of mangroves', *Australian Ecology Series* **59**(5), 352–353.
- Kazemi, A., Evans, H. B., Van De Riet, K., Castillo, L. and Curet, O. M. (2019), 'Hydrodynamics of Mangrove Roots and its Applications in Coastal Protection', *OCEANS 2018 MTS/IEEE Charleston, OCEAN 2018* pp. 1–8.
- Kirwan, M. L., Guntenspergen, G. R., D'Alpaos, A., Morris, J. T., Mudd, S. M. and Temmerman, S. (2010), 'Limits on the adaptability of coastal marshes to rising sea level', *Geophysical Research Letters* **37**(23), 1–5.
- Kirwan, M. L. and Megonigal, J. P. (2013), 'Tidal wetland stability in the face of human impacts and sea-level rise', *Nature* **504**(7478), 53–60.
- Krauss, K. W., Lovelock, C. E., McKee, K. L., López-Hoffman, L., Ewe, S. M. and Sousa, W. P. (2008), 'Environmental drivers in mangrove establishment and early development: A review', *Aquatic Botany* **89**(2), 105–127.
- Lee, S. Y., Primavera, J. H., Dahdouh-guebas, F., McKee, K., Bosire, J. O., Cannicci, S., Diele, K., Fromard, F., Koedam, N., Marchand, C. and Mendelssohn, I. (2014), 'Ecological role and services of tropical mangrove ecosystems : a reassessment', *Global Ecology and Biogeography* pp. 726–743.
- Lesser, G. R., Roelvink, J. A., van Kester, J. A. and Stelling, G. S. (2004), 'Development and validation of a three-dimensional morphological model', *Coastal Engineering* **51**(8-9), 883–915.
- Lugo, A. E. and Snedaker, S. C. (1974), 'The Ecology of Mangroves', *Annual Review of Ecology and Systematics* **5**(1), 39–64.
- Marois, D. E. and Mitsch, W. J. (2015), 'Coastal protection from tsunamis and cyclones provided by mangrove wetlands - A review', *International Journal of Biodiversity Science, Ecosystem Services and Management* **11**(1), 71–83.
URL: <http://dx.doi.org/10.1080/21513732.2014.997292>
- Massel, S. R., Furukawa, K. and Brinkman, R. M. (1999), 'Surface wave propagation in mangrove forests', *Fluid Dynamics Research* **24**(4), 219–249.
- Mazda, Y., Kanazawa, N. and Wolanski, E. (1995), 'Tidal asymmetry in mangrove creeks', *Hydrobiologia* **295**(1-3), 51–58.

-
- Mazda, Y., Kobashi, D. and Okada, S. (2005), 'Tidal-scale hydrodynamics within mangrove swamps', *Wetlands Ecology and Management* **13**(6), 647–655.
- Mazda, Y., Magi, M., Motohiko, K. and Hong, P. N. (1997), 'Mangroves as a coastal protection from waves in the Tong King Delta, Vietnam'.
- McIvor, A., Spencer, T., Möller, I. and Spaldin, M. (2013), 'The response of mangrove soil surface elevation to sea level rise', *Nature Conservancy and Wetlands International* .
- Meteorology, B. o. (2020), 'WillyWeather'.
URL: <https://wind.willyweather.com.au/nsw/far-north-coast/ballina.html>
- Moriasi, D. N., Arnold, J. G., Liew, M. W. V., Bingner, R. L., Harmel, R. D. and Veith, T. L. (2007), 'Model evaluation guidelines for systematic quantification of accuracy in watershed simulations.', **50**(3), 885–900.
- Mullarney, J. C. and Henderson, S. M. (2019), 'Flows within marine vegetation canopies', *Advances in Coastal Hydraulics* pp. 1–21.
- Noor, T., Batool, N., Mazhar, R. and Ilyas, N. (2015), 'Effects of Siltation, Temperature and Salinity on Mangrove Plants', *European Academic Research* **2**(11), 14172–14179.
URL: www.euacademic.org
- Norris, B. K., Mullarney, J. C., Bryan, K. R. and Henderson, S. M. (2017), 'The effect of pneumatophore density on turbulence: A field study in a Sonneratia-dominated mangrove forest, Vietnam', *Continental Shelf Research* **147**(October 2016), 114–127.
- NSW Government (2020), 'NSW Tides, 2019-2020'.
- Perkins, M. J., Ng, T. P., Dudgeon, D., Bonebrake, T. C. and Leung, K. M. (2015), 'Conserving intertidal habitats: What is the potential of ecological engineering to mitigate impacts of coastal structures?', *Estuarine, Coastal and Shelf Science* **167**, 504–515.
URL: <http://dx.doi.org/10.1016/j.ecss.2015.10.033>
- Poppema, D. (2017), 'Experiment - supported modelling of salt marsh establishment : Applying the Windows of opportunity', (June), 68.
- Quartel, S., Kroon, A., Augustinus, P. G., Van Santen, P. and Tri, N. H. (2007), 'Wave attenuation in coastal mangroves in the Red River Delta, Vietnam', *Journal of Asian Earth Sciences* **29**(4), 576–584.
- Ribberink, J. S. (2011), 'River Dynamics II : Transport Processes and Morphology', (March), 85.
- Roos, P. C. (2014), 'Marine Dynamics - Lecture notes and exercises on tides and wind-driven flow', pp. 1–79.
- Ryder, D., Mika, S., Richardson, M., Schmidt, J. and Fitzgibbon, B. (2015), 'Richmond Ecohealth Project 2014: Assessment of River and Estuarine Condition - Final Technical Report', (June).
URL: <https://www.ipart.nsw.gov.au/files/5d55f177-6785-4e2b-abea-4314fb4be5eb/Attachment-12.1-UNE-Richmond-Catchment-Ecohealth-Report.pdf>

-
- Saad, S., Husain, M. L., Yaacob, R. and Asano, T. (1999), 'Sediment accretion and variability of sedimentological characteristics of a tropical estuarine mangrove: Kemaman, Terengganu, Malaysia', *Mangroves and Salt Marshes* **3**(1), 51–58.
- Saintilan, N., Rogers, K., Kelleway, J. J., Ens, E. and Sloane, D. R. (2018), 'Climate Change Impacts on the Coastal Wetlands of Australia', *Wetlands* pp. 1–10.
- Smith, T. J. (1987), 'Effects of light and intertidal position on seedling survival and growth in tropical tidal forests', *Journal of Experimental Marine Biology and Ecology* **110**(2), 133–146.
- Temmerman, S., Bouma, T. J., Govers, G., Wang, Z. B., De Vries, M. B. and Herman, P. M. (2005), 'Impact of vegetation on flow routing and sedimentation patterns: Three-dimensional modeling for a tidal marsh', *Journal of Geophysical Research: Earth Surface* **110**(4), 1–18.
- Temmerman, S., Meire, P., Bouma, T. J., Herman, P. M. J., Ysebaert, T., Vriend, H. J. D., Nargis, C. and Orleans, N. (2013), 'Ecosystem-based coastal defence in the face of global change', *Nature* pp. 1–5.
- Teo, F. Y. (2010), 'Study of the Hydrodynamic Processes of Rivers and Floodplains with Obstructions Fang Yenn Teo', (September).
- The Open University (1999a), 'Waves, Tides and Shallow-Water Processes - Chapter 1: Waves', **5**, 95–108.
- The Open University (1999b), 'Waves, Tides and Shallow-Water Processes - Chapter 2: Tides', pp. 50–86.
- Thom, B. G., Wright, L. D. and Coleman, J. M. (1975), 'Mangrove Ecology and Deltaic-Estuarine Geomorphology: Cambridge Gulf-Ord River, Western Australia', *Journal of Ecology* **63**(1), 203–232.
URL: <http://www.jstor.org/stable/2258851>
- Tomlinson, P. (1986), *The botany of mangroves*, Cambridge University Press.
- University of Twente (2019), 'Syllabus Coastal Dynamics - Chapter 4: Short Waves', **27**(0), 1–20.
- Van Loon, A. F., Te Brake, B., Van Huijgevoort, M. H. and Dijkema, R. (2016), 'Hydrological classification, a practical tool for mangrove restoration', *PLoS ONE* **11**(3), 1–26.
- van Rijn, L. (2007), 'Unified View of Sediment Transport by Currents and Waves. II: Suspended Transport', *Journal of Hydraulic Engineering* **133**(4), 440–450.
URL: [http://ascelibrary.org/doi/abs/10.1061/\(ASCE\)0733-9429\(2007\)133:9\(1048\)](http://ascelibrary.org/doi/abs/10.1061/(ASCE)0733-9429(2007)133:9(1048))
- van Rijn, L. (2008), 'Principles of fluid flow and surface waves in rivers, estuaries, seas and oceans - Chapter 8'.
- Van Rijn, L. C., Ribberink, J. S., Van Der Werf, J. and Walstra, D. J. (2013), 'Coastal sediment dynamics: Recent advances and future research needs', *Journal of Hydraulic Research* **51**(5), 475–493.

-
- Van Santen, P., Augustinus, P. G. E. F., Janssen-Stelder, B. M., Quartel, S. and Tri, N. H. (2007), 'Sedimentation in an estuarine mangrove system', *Journal of Asian Earth Sciences* **29**(4), 566–575.
- Watson, J. G. (1928), *Mangrove forests of the Malay Peninsula*, 6 edn, Fraser & Neave, Singapore.
- WBM Oceanics (n.d.), 'Richmond River Estuary Processes Study Executive Summary'.
- Willemsen, P. W., Horstman, E. M., Borsje, B. W., Friess, D. A. and Dohmen-Janssen, C. M. (2016), 'Sensitivity of the sediment trapping capacity of an estuarine mangrove forest', *Geomorphology* **273**, 189–201.
URL: <http://dx.doi.org/10.1016/j.geomorph.2016.07.038>
- Willemsen, P. W. J. M., Horstman, E. M., Borsje, B. W. and Friess, D. A. (2015), 'Decreased Resilience of Mangroves stressed by Human Interference', pp. 1–23.
- Winterwerp, J. C. (2002), 'On the flocculation and settling velocity of estuarine mud', *Continental Shelf Research* **22**(9), 1339–1360.
- Winterwerp, J. C., Erftemeijer, P. L., Suryadiputra, N., Van Eijk, P. and Zhang, L. (2013), 'Defining eco-morphodynamic requirements for rehabilitating eroding mangrove-mud coasts', *Wetlands* **33**(3), 515–526.
- Wolanski, E. (1992), 'Hydrodynamics of mangrove swamps and their coastal waters', *Hydrobiologia* **247**(1-3), 141–161.
- Wolanski, E. and Ridd, P. (1986), 'Tidal mixing and trapping in mangrove swamps', *Estuarine, Coastal and Shelf Science* **23**(6), 759–771.
- Woodroffe, C. D. (1987), 'Pacific Island mangroves: distribution and environmental settings', *Pacific Science* **41**(1-4), 166–185.
- Woodroffe, C., Rogers, K., McKee, K., Lovelock, C., Mendelssohn, I. and Saintilan, N. (2016), 'Mangrove Sedimentation and Response to Relative Sea-Level Rise', *Annual Review of Marine Science* **8**(1), 243–266.

A Introduction to mangroves

Mangroves cover an entire ecosystem and not just one type of vegetation. A good understanding of what mangroves are and where and how they grow, is essential in order to understand the biophysical processes and for their possible implementation in coastal engineering. This chapter describes the biology and ecosystem of mangroves. First, a definition of mangroves is given. This is followed by two paragraphs about the biological and ecological aspects.

A.1 Definition

The term 'mangrove' is used in two ways. First, it can be interpreted as a single tree or shrub, with specific characteristics and a restricted living environment. Secondly, the term can be used to indicate tropical coastal vegetation consisting of such species (?). The definition according to [Duke \(1992\)](#) is that a mangrove is a tree, shrub, palm or ground fern, generally exceeding one half metre in height, and which normally grows above mean sea level in the intertidal zone marine coastal environments, or estuarine margins. The individual mangrove tree has a very distinct root structure, which will be described later in this chapter, which is able to obtain enough oxygen to survive during periodic inundations. The individual mangrove tree is capable of growing in intertidal zones, because it is tolerant to saline conditions. These saline conditions, along with a tidal regime and low energy wave environment, are in fact prerequisites to survive. The individual trees and their associated organisms (e.g. microbes, fungi, plants and animals) constitute the 'mangrove forest community' or 'mangal'. The mangal and its associated abiotic factors constitute the mangrove ecosystem ([Hutchings and Saenger, 1972](#); [Duke, 1992](#); [Tomlinson, 1986](#)).

Mangroves are regarded as the second highest valued biomes according to [de Groot et al. \(2012\)](#). The only biome with a higher economical value are coral reef ecosystems. These values are based on provisioning services (e.g. food, fresh water, wood), regulating services (e.g. climate, floods, diseases, purifying water), habitat services for different species and cultural services such as aesthetics or educational or recreational functions [de Groot et al. \(2012\)](#).

A.2 Biological aspects

The biological aspects that are elaborated on in this paragraph are the different species, the root structures and processes that influence the growth and development of mangroves.

A.2.1 Mangrove species

The classification of mangroves is not straightforward, species have often been categorized as 'true' mangroves and others as 'mangrove associates' ([Duke, 1992](#)). [Lugo and Snedaker \(1974\)](#) describes mangroves as a group of halophytic species belonging to twelve genera in eight different families. The combination of morphological and physical adaptations which is observed in this diverse group of plants have no equal among other plant families. There are certain attributes which are commonly shared among mangrove species, namely: mechanisms for coping with high salt concentrations, viviparous propagulus, structures to support the above ground mass and special breathing structures such as, pneumatophores and small air-breathing lenticals ([Duke, 1992](#)).

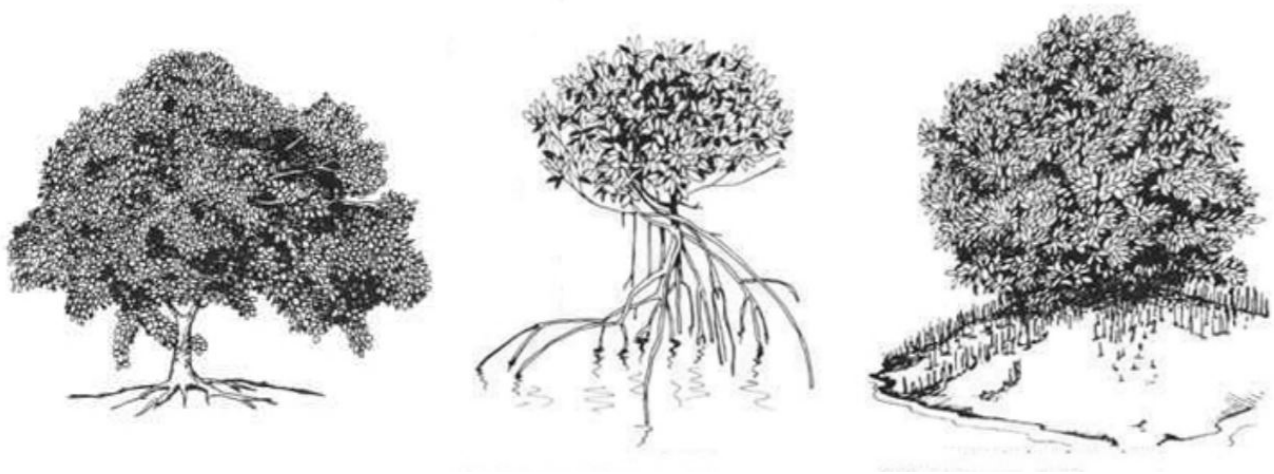


Figure 52: *White mangrove (l), Red mangrove (m), Black mangrove (r) de Vos (2004)*

Many botanists and researchers on mangroves still disagree over what constitutes a mangrove. Because of this, the number of mangrove species varies throughout literature. One of the best-documented and still relevant definition of mangroves is by Tomlinson (1986). In his book he states that his assessment is somewhat arbitrary and that the limits can be subject to discussion. Tomlinson (1986) identifies three groups; major elements of mangrove communities (Appendix A), minor elements of mangrove communities (Appendix A) and mangrove community associates.

Of all these species, the most well known and most common are the species of the genera *Rhizophora* and *Avicennia*. These representatives, *Avicennia germinans* and *Rhizophora mangle*, are often referred to as, respectively, the ‘Black mangrove’ and the ‘Red mangrove’. Together with the ‘White mangrove’, *Laguncularia racemosa*, they are the main mangrove species in the New World (Oceania and the Americas, see Figure 52 (Tomlinson, 1986).

A.2.2 Root structures

A very distinct characteristic of mangroves is their unique root system, which is highly variable for different species. Since mangroves are situated at inter-tidal flats which are submerged periodically, the mangroves need aerial roots for oxygen uptake. With the focus on the interaction between hydrodynamics and morphodynamics within mangroves, the root characteristics are of great interest, since they have an impact on the biophysical interactions in mangroves. The main types of aerial roots as proposed by Tomlinson (1986), but also supported by Hutchings and Saenger (1972), are summarized below and discussed briefly.

1. Stilt roots. This refers to the branched, looping aerial roots that arise from the trunk and lower branches of *Rhizophora* (figure 53). The description of ‘stilt’ roots refers to the supportive character these roots have. They are not only for aerial ventilation, but gradually take over the supportive function of the lower part of the trunk as the tree gets older. The nature of the spread of the roots is viewed as opportunistic since new roots arise only where the roots are damaged.

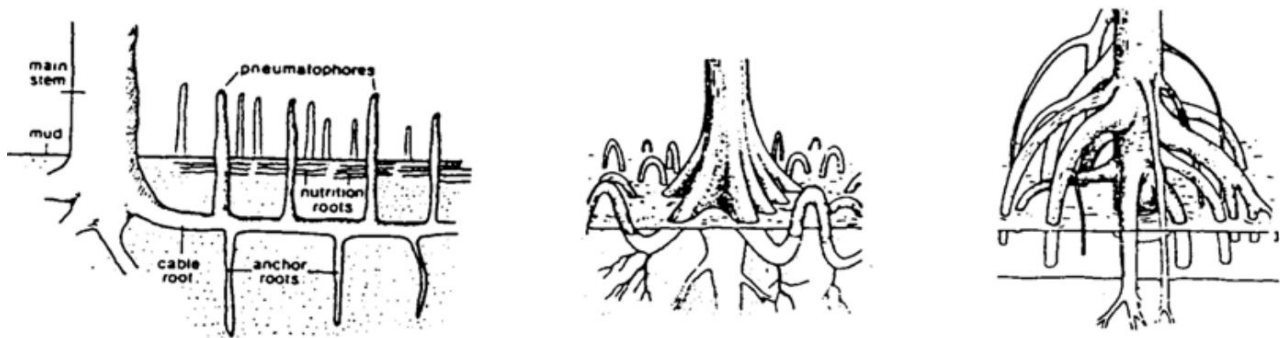


Figure 53: Different root systems; Pneumatophores (l), knee roots (m), stilt roots (r) de Vos (2004)

In a limited extent, stilt roots are found in species of *Bruguiera* and *Ceriops* and sporadically in some species of *Avicennia*.

2. Pneumatophores in *Avicennia* and *Sonneratia*. Pneumatophores are erect lateral branches of the horizontal roots, which are themselves buried in the substrate (figure 53). The pencil-like erect branches spaced at regular intervals are the visible part of the root system. In *Avicennia* these roots are of limited height (usually less than 30cm) and develop little thickening. In *Sonneratia* the roots have a much longer period of development and display secondary thickening so they can become up to 3m. The surface of the *Avicennia* remains smooth and spongy, while the *Sonneratia* have a more wood-like structure.
3. Pneumatophores in *Laguncularia*. The aerial roots of the *Laguncularia* are often not visible. However, these roots can under certain circumstances develop aerial roots, which rarely exceed 20cm. The development of these roots is considered facultative which results in some populations lacking them.
4. Root knees in *Bruguiera* and *Ceriops*. In these genera the horizontal roots periodically reorient as they grow through the substrate away from the parent tree. This results in a pronounced loop before continuing its horizontal growth. These branches or loops develop secondary thickening, and at these places new horizontal and anchoring roots are formed due to branching.
5. Root knees in *Xylocarpus*. Local erect outgrowths of the upper surface of the horizontal root system are a feature of the *Xylocarpus mekongensis* species. These knees are formed entirely by local secondary growth in the primary cable components. This is in the contrary with the root knees of *Bruguiera* and *Ceriops*, where the knees are a consequence of change in direction of primary root growth. Root knees in *Xylocarpus* may grow to a height of 50cm.
6. Pneumatophores in *Lumnitzera*. The root knees of *Lumnitzera* are not very pronounced. They may be thought of as structures intermediate between pneumatophores and knees.
7. Plank roots. In *Xylocarpus granatum* the horizontal roots become erected in the upper surface over their entire length due to eccentric cambial activity. Cambium is in plants the layer of actively dividing cells responsible for secondary growth.

Some species normally lack any elevated aerial part of the root system. These species may develop other structures to aerate the root system. This is however, not the subject of this study and therefore neglected.

A.2.3 Reproduction

Mangrove species are often hermaphrodite, which means that trees have both male and female flowers. Most mangroves are pollinated by animals (e.g. birds, bees, butterflies and bats). Only the *Rhizophora* species is said to be mainly pollinated by wind (Tomlinson, 1986). In order to reproduce, the establishment of seedlings is vital. However, due to tidal influence and wave attacks, the mangrove habitat is a rough environment for ordinary seeds to settle and develop. This led to the development of seedlings instead of seeds by some mangrove species. When the fruit of these species mature, the embryo grows first out of the seed coat and then out of the fruit while still attached to the parent plant. This is called 'true vivipary' and observed in the whole *Rhizophoreae* family. The advantage of true vivipary is that the seedling can develop more rapidly when it reaches favorable substrates. In some mangroves 'cryptovivipary' exists, in which the embryo emerges from the seed coat but not the fruit before it is separated from the parent plant. This is more common in the *Aegiceras*, *Avicennia*, *Nypa* and *Pelliciera* families. The reason why vivipary is so common in mangroves is a topic that fostered plenty of discussion but no generally accepted explanation Tomlinson (1986).

A.3 Ecological aspects

To get insight in the functioning of the mangrove, as a possible laboratory' for hydraulic measurements, some subjects need to be addressed and clarified. In this paragraph, the distribution and zonation of mangroves over the world, the settings in which they occur and the types of mangrove forests are described. Also, a few important factors influencing the growth and development of mangroves are discussed.

A.3.1 Distribution

Duke (1992) argues that mangroves are distributed over the world according to three important scales, namely: coastal range, location within an estuary and the position along the inter-tidal profile. On a global scale, mangrove plants are found throughout tropical regions of the world. More precisely, there is a clear tropical distribution pattern with major deviations matching the warm and cold oceanic currents Duke (1992). The African Euro-Asian continents and the Pacific Ocean are the two major barriers which influence the dispersal of most warm coastal marine organisms. This results in a division of mangrove species into two global hemispheres. The Atlantic East Pacific, often referred to as the *New World*, and the Indo West Pacific, or *Old World*, see figure 54 (Tomlinson, 1986). These more-or-less equal portions of the earth also have equivalent areal extent of mangrove forests Duke (1992), but not in number of mangrove species. The New World group only has 8 species, whilst the Old World includes 40 species (Tomlinson, 1986; Duke, 1992).

Mangroves are also distributed along two other scales, namely their location within an estuary, and their position along the intertidal profile Duke (1992). Vegetational zonation of the mangroves has long attracted scientific interest states Bunt (1996). Within the mangrove forests, communities are

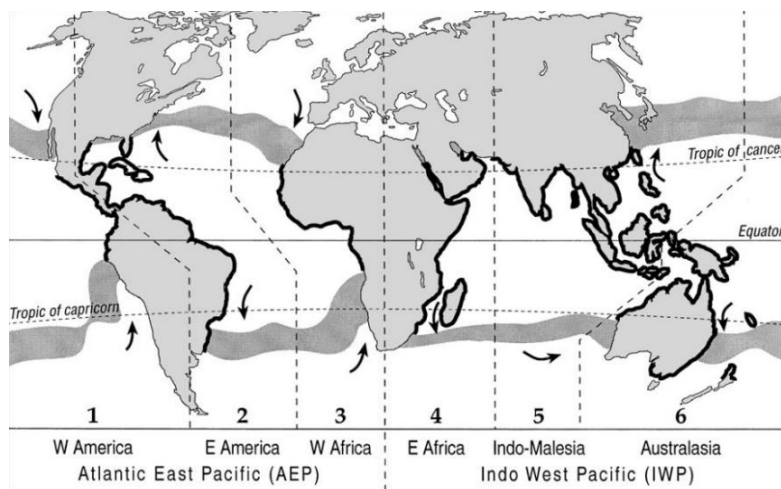


Figure 54: World distribution of mangroves showing their coastal extent (outlined) and two global hemispheres as discussed in text [Duke \(1992\)](#)

often zoned parallel to the shoreline, with series of different species dominating distinct sections from shore to the landward limits. For vegetation along open shorelines in Eastern Australia the following zonation from land to sea can be recognised [Bunt \(1996\)](#): (1) landward fringe; (2) landward *Avicennia*; (3) *Ceriops* thickets; (4) *Bruguiera* forests; (5) *Rhizophora* forests; (6) seaward fringe (*Aicennia* and/or *Sonneratia*). [Bunt \(1996\)](#) also concludes that describing zones in mangroves has to be done with care, since the above stated patterning is not globally applicable. Other authors argue that external physical forces such as variation in frequency of tidal inundation, tidal range, and salinity cause zonation ([Thom et al., 1975](#); [Smith, 1987](#); [Heumann, 2011](#)).

The spatial distribution of mangrove species within an estuary can be classified into three categories [Duke et al. \(1998\)](#): downstream, intermediate and upstream. These categories are regarded as proportional to each other.

A.3.2 Environmental settings

Mangroves occur in a number of environmental settings, consisting of particular suites of recurring land-forms while they differ in the physical processes responsible for sediment transport and deposition [Woodroffe \(1987\)](#). These environmental settings describe which particular combinations of geomorphological processes are dominant, which in turn affect the ecological constraints on the population and development of mangrove species [Adame et al. \(2010\)](#). The geophysical characteristics (e.g. climate, tides and sea-level), the geomorphological characteristics (the dynamic history of the land surface and present-day geomorphological processes) and the biological characteristics (e.g. micro topographic, elevation and sediments, drainage and nutrient status) define the setting. [Woodroffe \(1987\)](#) gives a summary of the five environmental settings as described by [Thom \(1982, 1984\)](#). A schematic representation can be seen in figure [55](#).

1. *River dominated*. Most of the mangrove forests can be found in river dominated deltas along coastlines of low tidal range. The river distributes enormous amounts of sediment into the delta

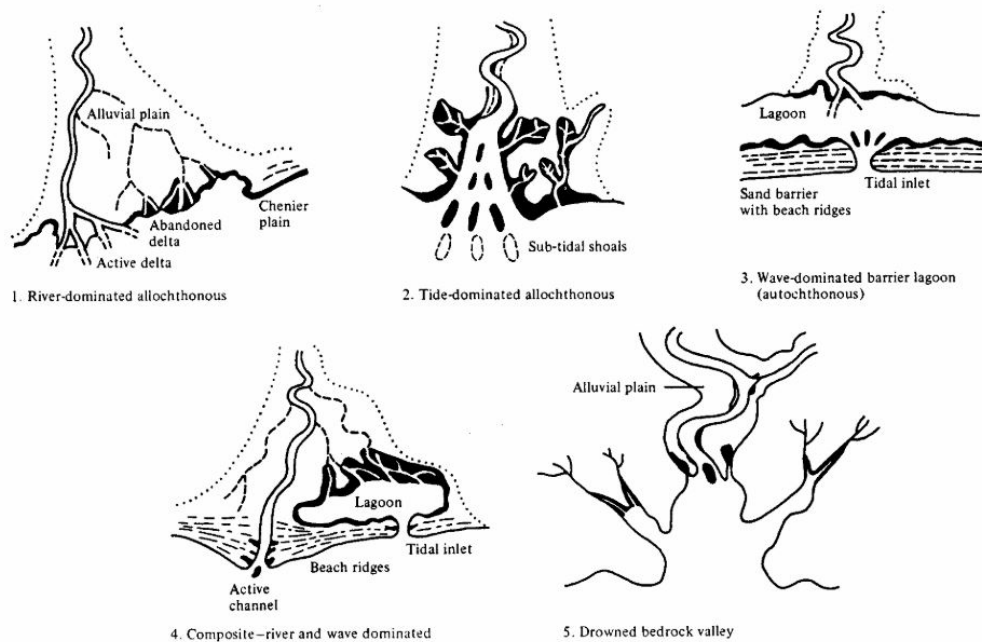


Figure 55: Five geomorphological settings for mangroves as stated by Woodroffe (1987) (de Vos, 2004)

and are therefore very dynamic. Since the freshwater discharge is relatively high, the river outlet and branches may not be inhabited by mangroves. Instead, the adjacent plains are more suitable for mangrove colonisation. Examples of this setting are the Mississippi delta in the USA and the Atrato delta in Colombia.

2. *Tide dominated.* Tide dominated areas are characterised by a high tidal range (< 4m) and an extensive, low-gradient inter-tidal zone where mangrove species can develop. In this zone, estuaries are characterised by strong bidirectional tidal velocities and low wave energies due to dissipation over the large tidal flats. As seen in figure 55, mangroves can be along the tidal flats and in the branches of the river. Examples are the Klang delta in Malaysia and the Ord River delta in Australia.
3. *Wave dominated.* Coasts that are dominated by wave energy and where there is an abundant supply of sand, formation of shore-parallel sandy ridges or barriers occur. High wave energy and sandy substrates are usually not favourable for mangrove colonisation, but mangroves are found on the protected leeward side of the barriers and along the shores of the lagoon. An example of this is Tugurah Lake in Australia.
4. *Composite river and wave dominated.* This setting is a combination of the river and wave dominated settings (setting 1 and 3). In the composite settings, rivers carry large volumes of sand to a wave dominated coast. Complex landforms and lagoons are developed where fluvial sands are distributed along the coast. Mangroves colonisation takes place along abandoned river branches, near river mouths, and along lagoon shores. An example is the Grijalva delta in Mexico.

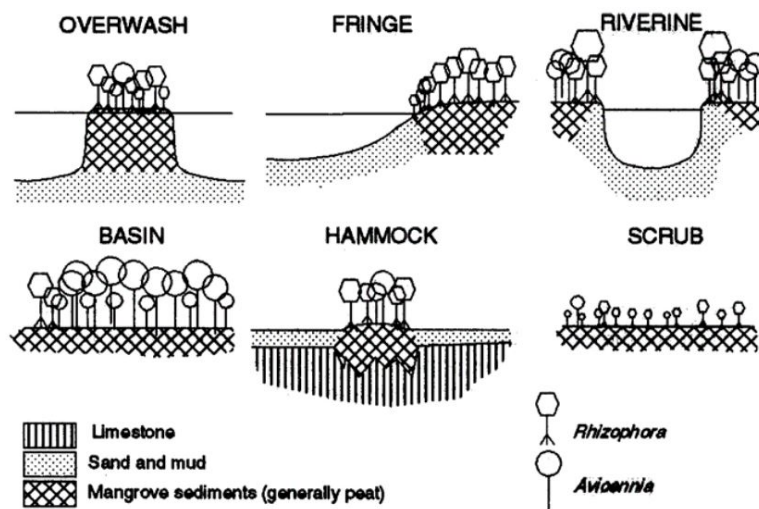


Figure 56: Mangrove forest types de Vos (2004)

5. *Drowned bedrock valley*. These setting occur near steep rocky valley systems, which have been drowned by a rising sea level. Due to low river discharge, low wave action, and low tidal range the sediment deposition is minimal creating an open estuarine system. Mangroves occur on the heads of the drowned river branches. This setting is usually found at the Pacific coast of the United States. Another example is Broken Bay in Australia.

A.3.3 Types of mangrove forests

Lugo and Snedaker (1974) developed a functional classification of mangrove forests, which is widely used and accepted. This classification consists of six categories and is shown in figure 56 and discussed briefly.

1. *Overwash*. Consisting of islands which are frequently overwashed at high tide. Multiple species of mangroves may be present, but *Rhizophora* usually dominates.
2. *Fringe*. This forest type occurs along the fringes of protected shorelines and islands and is best defined along shorelines whose elevations are higher than mean tide. Due to the relatively open exposure along shorelines, the fringe forest is occasionally subjected to strong winds or storms.
3. *Riverine*. The riverine type designates the tall floodplain forests which occur along river and creek drainages. They are usually separated from the drainage way, but flushed daily by the tides. This type is often behind a fringe forest occupying the slope of the drainage way.
4. *Basin*. This forest type occurs in inland areas where drainage depressions which channel terrestrial runoff towards the coast. Close to the coast, they are influenced by daily tides and are usually dominated by *Rhizophora sp.* More inland, the influence of the tide decreases and other species such as *Avicenniaceae* occur.

-
5. *Scrub or Dwarf*. All main species are present, but the height is limited to around 1.5-2m. These areas are characterized by high EvapoTranspiration (ET) and low precipitation rates causing high levels of soil salinity. Salinity and nutrients appear to be the limiting factors affecting growth.
 6. *Hammock*. A variant of the basin forest occurs, but where the ground is slightly elevated relative to surrounding areas.

Lugo and Snedaker (1974) remarks that the given functional classification is derived for mangroves in Florida, but has been observed in mangroves on the Western Hemisphere as well. Krauss et al. (2008) argue that a split of these functions is needed in order to be more inclusive of global mangrove settings. They propose an combination of the geomorphological settings (as discussed in section A.3.2 to produce an overall classification scheme robust to the many conditions of mangrove forests globally.

A.3.4 Factors influencing mangrove growth and establishment

In this section, different factors which influence the establishment and development of mangroves are discussed.

Tidal range

The tidal range is the main driver which determines the area and zonation where different mangrove species grow. The larger the tidal flat, the wider the area influenced by tidal inundations is. Subsequently, the species diversity is strongly influenced by the tidal range. More different species can be found within a forest with large differences in inundation levels and salinity. The literature is not clear about a minimum and maximum tidal range for mangroves to develop, but nowadays the classic hydrological mangrove classification of Watson (1928) is still applied (Van Loon et al., 2016). Watson (1928) found that mangrove forests in Malaysia can be grouped into 5 numerical classes by means of their tidal regime, elevation and flooding frequency. Despite its wide applications, some adaptations were necessary in order to make it more suitable for irregular tides and elevation. The adapted classification, with the inclusion of the duration of the inundation and a sixth class, has been used ever since (Van Loon et al., 2016).

Windows of Opportunity

Not only growth of mangroves attracts interest among researchers, also the factors which influence the colonisation are of great interest. Windows of opportunity are periods where disturbances are low or absent in order for the seedling to establish. However, there used to be a general lack of mechanistic understanding of the processes responsible for these thresholds (Bouma et al., 2009). In order to generate a mechanistic understanding of the thresholds for mangrove colonisation on tidal flats, the boundary conditions that offer the window of opportunity are of critical importance (Balke et al., 2011).

Balke et al. (2011) showed with flume studies and field observations that 3 thresholds have to be passed until the seedling is successfully established. First, anchorage of the seedling requires a minimum period during which it is free from inundation after reaching the substrate. Second, the root growth has to surpass a certain minimum length to withstand disturbances of hydrodynamic forces by waves and currents induced on the seedlings. Third, the root length needs to be sufficient to resist disturbances from removal of sediment around the seedling. This can be due to sediment mixing

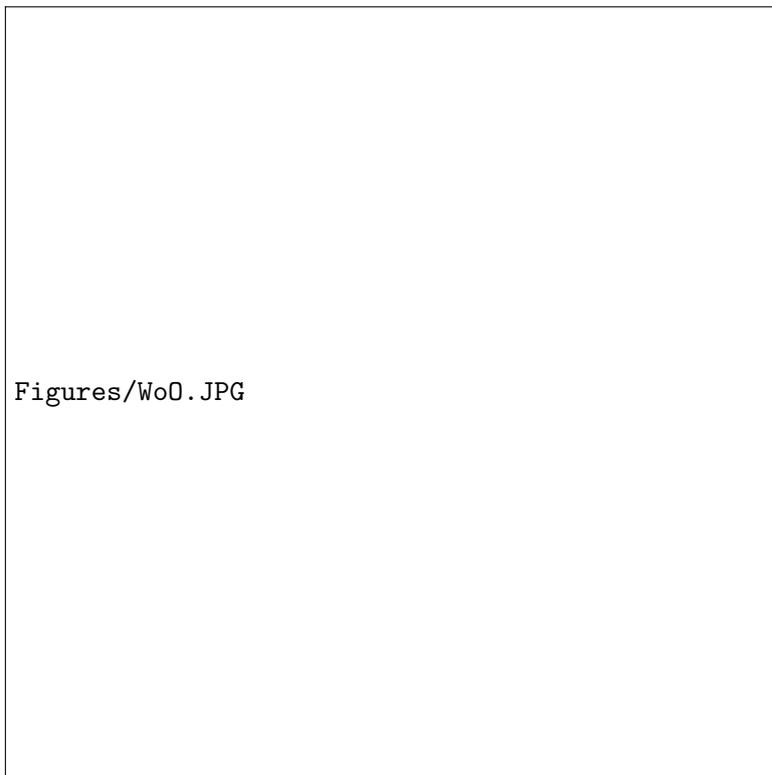


Figure 57: Schematic representation of the three thresholds that need to be reached during establishment of an *Avicennia* seedling (Balke et al., 2011)

and/or sheet erosion. Figure 57 shows a schematic representation of the three thresholds as described by Balke et al. (2011). In a more recent study, Balke et al. (2013) performed experiments to elucidate the effect of sediment disturbance in combination with water movement and inundation stress during the seedling stage. Also, Balke et al. (2015) provides a first attempt to model and potentially predict seedling survival dynamics along a elevation gradient, where physical disturbance is the main bottleneck which limits mangrove development. The model they developed can be used as a tool to hindcast and potentially predict mangrove colonisation on tidal flats.

Temperature

Temperature is a major factor that varies within the distributional range of mangrove vegetation and can therefore have a large impact on seedling establishment. Mangroves may encounter either high or low temperature extremes (Krauss et al., 2008). Low temperature is widely regarded as the primary control on the latitudinal limits of mangroves globally (Tomlinson, 1986; Duke et al., 1998). Mangrove plants do not adequately develop when annual average air temperatures are below 19°C . This corresponds with the sea water isotherm of 20°C during the coldest period of the year (Noor et al., 2015). Photosynthesis is reported to decline sharply when the air temperature exceeds 30-35°C (Noor et al., 2015; Duke et al., 1998).

Salinity

One of the most important and considered driver in mangrove establishment and growth is salinity (Tomlinson, 1986; Krauss et al., 2008). As mentioned before, mangroves do not require salt water, but only tolerate it. This feature enables them to grow in coastal waters without competition of other plant species that do not tolerate salt water. Salinity refers to the number of grams of dissolved salts in 1000 grams of seawater. Values are usually expressed in parts per thousand (‰) and range from 33 to 38 ‰ in the open ocean (Tomlinson, 1986). As for many other ecological restraining factors, it is the extremes that are limiting. Some species can adjust to about 90 ‰, but higher tolerances have been mentioned. The optimal range for tree growth fluctuates between 5 and 75 ‰. The tolerance level for saline environments is not equal among all families. Since there is a salinity gradient, the difference in tolerance level can cause zonation (section A.3.1) within the mangrove community. Three coping mechanisms related to high salt concentrations are mentioned by Noor et al. (2015). These are; (1) salt exclusion at root level, (2) salt excretion and (3) salt accumulation within leaf cells followed by defoliation (premature removal of leaves). Even with these mechanisms, tree growth is still inversely proportional to salinity (Noor et al., 2015; Smith, 1987).

Concluding remarks

There are still a lot of biotic interactions and environmental factors which influence the mangrove flora and development which are not described in this study. Other important drivers are predominantly rainfall, storms, currents, sea level rise, sediments, nutrients and oxygen Duke et al. (1998). Later in this report, attention is given to currents, sea level rise and sediments. The importance of the remaining drivers is known, but not extensively elaborated on in this report.

B Biophysical interactions

In this research, biophysical interactions concern the impacts of hydrodynamic forces on vegetation and the land surface and inversely the feedback of vegetation on the hydrodynamics and sediment transport dynamics. This section is structured by first describing the process in a general way, and then applying it to a mangrove environment.

B.1 Hydrodynamics

With mangroves existing at the land-sea interface and being subject to inundations, physical processes related to hydrodynamics and morphodynamics shape the mangrove environment. The physical processes work at different time and length scales. The available knowledge on these physical processes that are of importance in a mangrove ecosystem and some gaps in the existing knowledge are described in this section. This section will start with the hydrodynamics on the largest scales, and it will conclude with turbulence, which are the smallest scale of hydrodynamic forces that are relevant. The processes are first described in a general way, and then applied to a mangrove environment.

B.1.1 Tides

Tidal characteristics

The longest oceanic waves are those associated with the tides. They are characterised by the rhythmic rise and fall of sea-level over a period of half a day or a day. The rise and fall are a result of the horizontal progression of water in the tidal wave. The rising tide is often referred to as *flood* whereas the falling tide is called the *ebb* (The Open University, 1999b; Roos, 2014). Because of their long period and wavelength, tidal waves behave as depth-dependent shallow-water waves. Since $c = \sqrt{gh}$ holds, the wave crest (high water) will travel faster than the wave trough (low water). As a result, there is an asymmetry in the tidal cycle, with a relatively long time interval between high water and the succeeding low water, and a shorter interval between low water and the next high tide. The peak current velocity is thus usually larger at ebb than at flood tide (Mazda et al., 1995).

Tidal attenuation

Usually, lower velocities in the forests are observed due to the presence of vegetation, which in turn cause extra turbulence that dissipates the tidal energy (Kazemi et al., 2019). This results in a gradient in flow velocity during ebb and tide, often referred to as the 'tidal asymmetry'. This tidal asymmetry is acknowledged and described by i.a. Dronkers (1986); Furukawa et al. (1997) and Mazda et al. (1995). The latter found that the tidal current velocity in a mangrove creek is the sum of two components; u_H and u_A . u_H is due to tidal flows in a tidal channel without a floodplain, and is tidal symmetric. u_A is due to water exchange between the creek and the swamp, and shows a clear tidal asymmetry. A numerical model was developed by Horstman et al. (2015) to study the contributions of various biogeophysical mangrove settings to these observed tidal dynamics. They concluded that the topography and relative elevation are the main drivers of this tidal flow routing, instead of vegetation density. Wolanski (1992) showed that tidal currents in the creek generally exceed 1 m/s, with stronger ebb currents than flood currents. Tidal current velocities in mangroves are in general much lower than in the tidal creeks or in the waters in front of the mangrove forest and have a maximum of around 0,2

m/s (Furukawa et al., 1997). As stated before, the lower velocities in the forests are mainly due to the energy dissipation by vegetation. The impact of this energy dissipation mechanism is according to Mazda et al. (1997) and Mazda et al. (1995) larger compared to bottom friction. In section B.2, the effects of tides and tidal asymmetry on the sedimentation patterns will be discussed.

B.1.2 Short Waves

Wave characteristics

The periodic short surface waves that can generally be observed on beaches, have wave lengths and wave periods which are an order of magnitude smaller than the long waves as induced by tidal forces. Short waves can be described with the two-dimensional (2DV) Navier-Stokes Equations (Furukawa et al., 1997). The Linear Wave Theory (LWT), which gives insight in water flows and pressures as induced by short waves over the water depth, is an approximation to describe the progression of sinusoidal waves from deep to shallow waters (University of Twente, 2019).

The energy a wave possesses is in two forms (The Open University, 1999a):

1. *Kinetic Energy*, which is the energy inherent in the orbital motion of the water particles.
2. *Potential Energy*, possessed by the particles as a result of being displaced from their mean (equilibrium) position.

For a water particle in a given wave, energy is continually being converted from potential energy (at the crest and trough) to kinetic energy (as it passes through the equilibrium position), and back again. The total wave energy E per unit area is described by the following formula:

$$E = 1/8\rho gH^2 \quad (\text{B.1})$$

When waves approach the shore, wave energy is transmitted in the cross-shore direction of the propagation. The velocity of this propagation is equal to the group velocity of the waves and is determined by:

$$c_g = n \cdot c \quad (\text{B.2})$$

In which c is the wave celerity of a single wave, and n a dimensionless factor which depends on the ratio between water depth and wavelength. The wave celerity and n are described by:

$$c = \frac{\omega}{k} \quad \text{and} \quad n = \frac{1}{2} \left(1 + \frac{2kh}{\sinh 2kh} \right) \quad (\text{B.3})$$

In this formula, ω represents the rotational speed of the waves, k the wave number and h the water depth. They are described by:

$$\omega = \frac{2\pi}{T} \quad \text{and} \quad k = \frac{2\pi}{L} \quad (\text{B.4})$$

The only unknowns in the LWT are now the wave period T and wavelength L . The calculation of the wavelength is an iterative process, since the dispersion relation of the wavelength is a function of itself:

$$L = L_0 \tanh \frac{2\pi h}{L} \quad \text{with:} \quad L_0 = \frac{gT^2}{2\pi} \quad (\text{B.5})$$

The final unknown variable, L_0 is the wavelength at deep water. Finally, the energy flux F can be determined. The flux describes the transmitted wave energy in the direction of the wave propagation:

$$F = E \cdot c_g \quad \text{or} \quad F = E \cdot n \cdot c \quad (\text{B.6})$$

Following from the Linear Wave Theory, the orbital velocity u with the velocity amplitude \hat{U} can be written as:

$$u(x, z, t) = \hat{U}(z) \sin(\omega t - kx) \quad \text{with:} \quad \hat{U}(z) = \omega a \cdot \frac{\cosh k(h+z)}{\sinh kh} \quad (\text{B.7})$$

The simple wave theory introduced above is a first-order approximation, and makes certain assumptions (The Open University, 1999a). The most relevant assumption is that it assumes an uniform depth and the bottom has no bumps and subsequently no bottom friction (Mullarney and Henderson, 2019; The Open University, 1999a).

Wave attenuation

Waves penetrating through mangrove forest are subject to substantial energy loss and are dissipated (Dalrymple et al., 1984; Horstman et al., 2014; Massel et al., 1999; Mazda et al., 1995). There are two main energy dissipation mechanisms in the mangrove forests; multiple interactions of wave motion with mangrove trunks and roots, and bottom friction. Bottom friction can be accommodated through the concept of a bottom friction coefficient (Massel et al., 1999). Factors within the forest itself that determine the amount of drag include the specific characteristics of the species (e.g., presence of pneumatophores or complex root systems), the density of the forest, and the diameter of the tree stems (Marois and Mitsch, 2015).

As discussed above, there is a general consensus that drag force plays an important part in the behaviour of waves in mangroves. However, Mullarney and Henderson (2019) adopt the Linear Wave Theory, which neglects drag, for the modelling of wave attenuation. Instead, they used the drag to be a linearized function of the velocity to represent the drag force. They argue that non-dissipative linear theory provides a useful first approximation, because drag often has a small effect within a single wave period.

The paper by Horstman et al. (2014) gives a nice overview of previous studies about wave attenuation in mangroves. Horstman et al. (2014) also compares the wave attenuation in these different mangrove and vegetation settings. Studies mentioned are amongst other things Mazda et al. (1995, 2005); Quartel et al. (2007) and Bao (2011). As modelling of waves through vegetation becomes more sophisticated, there are still some challenges for future research. The estimation of mean drag and wave dissipation in flexible canopies remains a significant challenge Mullarney and Henderson (2019).

Current research emphasizes the function of coastal protection by mangroves (Borsje et al., 2011). Marois and Mitsch (2015) conducted a review of recent research regarding the extent of coastal protection provided by wave attenuation in mangroves, that includes observational studies, numerical modelling, and laboratory experiments. They described their findings based on the methodology and

event type and concluded that observational studies have not provided conclusive results on the extent of coastal protection provided by mangroves from extreme natural disasters. However, results from several recent numerical and physical models support the mitigating capabilities of mangroves for cyclone storm surges and small tsunamis. Further research is still needed to provide a better assessment of the feasibility of incorporating mangroves into coastal protection plans (Borsje et al., 2011; Marois and Mitsch, 2015; Temmerman et al., 2013).

B.1.3 Turbulence

The most complex dynamics of water occurs on the smallest scale. This irregular motion results in chaotic changes in pressure and flow velocity, which is in contrast to laminar flow, where fluid flows in parallel layers with no disruption between those layers. The presence of vegetation or roughness introduces significant spatial variation to flow and turbulence, which ultimately affects the distribution of sediment within vegetated areas (Mullarney and Henderson, 2019). These obstacles also generate complex two-dimensional currents, with jets, eddies and stagnation regions (Furukawa et al., 1997). Drag forces and turbulent intensity depend on properties of the flow (e.g. flow velocity and level of submergence) as well as the vegetation characteristics: the number, size, shape and flexibility of stems (Norris et al., 2017). Flows which encounter vegetation will form turbulent wakes once the Reynolds number is greater than about 50 for single stems and within the range of 150-200 for multiple stems. Within these wakes, the energy of waves and currents is converted into turbulent energy.

Multiple studies (Temmerman et al., 2005; Norris et al., 2017) defined the canopy drag force per cubic meter, denoted as F_D as a function of the vegetation geometry and the properties of the flow. This expression however neglects the interactions between stems, which may often be valid (Mullarney and Henderson, 2019):

$$F_D = \alpha \frac{1}{2} C_D \rho U^2 \quad \text{with} \quad C_D = f(Re) = f\left(\frac{UD}{\nu}\right) \quad (\text{B.8})$$

Where C_D is the drag coefficient, $\alpha = N \cdot D$ is the frontal area of the canopy per cubic meter calculated by the number of stems per square meter of the bed N and diameter D and U is the fluid velocity in front of the stem. The drag coefficient is a function of the Reynolds Number. This is an indicator for the turbulence of the flow with the flow velocity, stem diameter and viscosity as parameters.

B.1.4 Density induced flow

Density induced flow is, as stated in the section before, also a result of the turbulent flow due to pressure gradients. However this flow can, on a larger scale, also be related to spatial density gradients of the fluid-sediment mixture due to variations of temperature, salinity and/or sediment concentration. Density variations induced by salinity in the coastal zone are most commonly the result of lower density fresh water river outflow into saline sea water characterised with higher density. The presence of this salinity gradient leads to formation of horizontal and vertical circulation. The density gradient effect is most pronounced in the near-bed region increasing onshore near-bed velocities during flood and reducing offshore near-bed velocities during ebb. As a result, a landward near-bed residual current is generated, which may cause a net landward transport of sediments, while near the water surface residual flow is in the seaward direction (van Rijn, 2008)

B.2 Sediment dynamics

Sedimentation refers to the deposition of inorganic sediments and organic matter onto the soil surface. The substrate beneath mangroves is composed of both inorganic mineral sediments and organic components which originates primarily from mangroves and other organisms. Suspended sediment is introduced to coastal areas either by river discharge, dumping of dredged material and re-suspension of bottom sediment by waves and ships [Furukawa and Wolanski \(1996\)](#). In areas where there is a deficit of allochthonous sediments, mangroves themselves contribute to the accumulation of autochthonous material by peat formation, root matter or other organic materials. Allochthonous sediments are produced from outside a site, while autochthonous sediments are produced by living organisms.

Mangroves are generally known for being depositional sites for sediment and associated carbon and nutrients ([Furukawa and Wolanski, 1996](#); [Adame et al., 2010](#)). Most coastal mangroves are connected to the sea via a tidal creek. The sediment transport processes in these creeks have already been investigated in detail, and are predominantly hydrodynamic processes as described in section [B.1](#) ([Woodroffe et al., 2016](#)). In the following sub-sections, attention is given to sediment transport due to tides, waves and river discharge.

B.2.1 Sediment transport due to tides

The tidal asymmetry is acknowledged to be one of the major causes for the sediment deposition in mangroves [Furukawa and Wolanski \(1996\)](#). As mentioned before, the peak flood and ebb velocities during a tidal cycle are rarely of an equal magnitude. This leads to an effect called 'tidal pumping', where flood tides carry farther upstream than ebb flows carry it downstream. This mechanism can trap sediments in the estuary ([Woodroffe et al., 2016](#)). Not only the flow velocity impacts the sedimentation processes, also the grain and environmental properties have a large impact. The fall velocity of sediments is of particular interest, since it directly influences the ability of (suspended) sediments to settle. For natural sediments, the fall velocity w_s can be determined according to the parameters in equation [B.9](#) ([Ribberink, 2011](#)). The grain diameter appears to be the most significant parameter according to [van Rijn \(2007\)](#).

$$\omega_s = f(\rho_s, \rho, D, v, g,) \quad (\text{B.9})$$

The presence of other grains makes the fall velocity depend on the sediment concentration. The fall velocity decreases as the concentration increases due to hindered settling ([Winterwerp, 2002](#)). On the other hand, cohesive sediment flocculation (mostly mud) can significantly increase the fall velocity. [Furukawa and Wolanski \(1996\)](#) combines the fall velocity and flow velocity to derive an equation for the sedimentation rate S , and states:

$$S = C_o w_s \exp\frac{w_s x}{h u} \quad (\text{B.10})$$

Where C_0 is the sediment concentration at the creek bank, x distance into the mangrove forest from the tidal creek, h the water depth and u the flow velocity. This formula implies that smaller particles are often found more inland.

[Furukawa and Wolanski \(1996\)](#) show that mangroves actively create their own ecosystems by trapping sediment. The trapping mechanism is due to the high micro-turbulence created by the flow around

the vegetation, which maintains sediment in suspension at flood tidal currents. It should be noted that the trapping capacity, is highly dependent on the species Tomlinson (1986). This sediment settles at the time of slack flood tide, when turbulence decreases. This sediment is not likely to re-entrain in vegetated areas by ebb tidal currents, because of the sluggish flow velocity. These processes result in a net input of sediments into the vegetated areas of mangroves, while the creeks are scoured by the enhanced ebb tidal outflow due to the tidal asymmetry Mazda et al. (1995). In their field study Horstman et al. (2017) observed increased sediment concentrations in front of vegetated areas, which might be due to the sediment's re-suspension.

The trapping phenomenon is also explained by Wolanski and Ridd (1986). They describe, besides the trapping mechanism, the buoyancy effect. The observed buoyancy effect, an upward force exerted by a fluid to oppose the weight of an object or other fluid, is concluded to affect the settling of fine sediments out of suspension.

B.2.2 Sediment transport due to waves

In addition to tidal currents, short waves also contribute to bringing and keeping sediment in suspension in estuaries. The orbital velocities of the waves protrude downward to the seabed, where they are able to entrain sediments. The mobility of the sediment is measured by the so-called Shields-parameter θ Ribberink (2011). This parameter plays a significant role in the transport of sediment. The critical value, which determines the start of motion, depends on the grain attributes and the flow pattern near the bottom. When sediment particles are entrained underneath waves and near the bed, the particles are transported into the mangrove forest due to the horizontal wave progression. Dronkers (1986) notices that waves counteract a landward residual transport of fine sediment by tidal currents, or enhance a seaward residual transport. However, the cross-shore sand transport, in particular the wave related component, is not fully understood due to the complex interaction processes between the flow, suspended sand and the seabed Van Rijn et al. (2013); Elfrink et al. (2006).

B.2.3 Sediment transport due to river discharge

Freshwater discharge appears to be an important external physical force that controls sediment deposition and transport to the continental shelf through estuaries Hossain et al. (2001). This physical process is largely controlled by seasonal changes of the river discharge pattern. Due to significant increase in current velocity and river discharge, net sediment transport rate increases during the rainy months. At this time, the buoyancy effect is important as freshwater is captured in the forest during high tide. In addition, the increased erosion rates due to the increase in discharge velocity contributes to the sediment budget at the foreshore of mangroves. The low discharges during the dry season result in a landward transport of sediment by tides. But, the reduced river discharges lowers the fluvial sediment input (Hossain et al., 2001; Hossain and Eyre, 2002; Saad et al., 1999). In the end, the average sediment accretion rate is lower during dry seasons compared to wet seasons Saad et al. (1999).

B.3 Morphodynamics

In this sub-section, attention is given to the processes occurring in mangroves which are responsible for the mangrove morphodynamics. Current literature also suggests the importance of SLR to the morphodynamics of mangroves (McIvor et al., 2013; Akumu et al., 2011; Woodroffe et al., 2016). Also, understanding of the relation between SLR and mangroves is of importance for the author's thesis. For these reasons, the dynamics caused by SLR are also mentioned. This sub-section give an overview of current knowledge, but does not attempt to provide an extensive review or bibliography of relevant publications because of the large number of processes involved.

First, in order to understand when and where mangrove surface elevation is likely to be able to keep pace with sea level rise in the future, we need to understand the processes involved in surface elevation change. These processes can be divided into surface processes and sub-surface processes (McIvor et al., 2013).

B.3.1 Surface processes

Surface processes include all processes which affect the material arriving at the sediment surface and the fate of this material. A distinction can be made into four processes; sedimentation, accretion, erosion and faunal processes (i.e. processes caused by animals that live within mangrove areas). Sedimentation is already briefly explained briefly in section B.2. According to McIvor et al. (2013) the factors which are likely to affect sedimentation rates in mangroves are the amount of incoming sediment and locally generated material, the period of inundation when external material can settle, and factors affecting whether particles are able to settle or are quickly re-suspended, including flow rates and flocculation of particles. Sedimentation also contributes to accretion, which occurs when the deposited material becomes fixed in place. In other words, when it can no longer be washed away by waves and tides. Factors influencing the accretion are e.g. the growth of mangrove roots, formation of benthic mats and consolidation. Erosion refers to the loss of surface material caused by the top layer of the surface being sheared off by the flow of water. This leads to a loss in elevation. Erosion is dependent on the erodibility of the surface layer and the hydraulic stress. Finally, the surface is also affected by faunal processes. These processes are mainly due to the presence of crabs, according to McIvor et al. (2013).

B.3.2 Sub-surface processes

McIvor et al. (2013) proposes a distinction between three groups of subsurface processes, namely: the growth and decomposition of mangrove roots and organic matter, the swelling and shrinkage of soils and the compaction or compression of soils. The growth and decomposition of mangrove vegetation is influenced by tree health, salinity, temperature, nutrient, tree species, and soil aeration. Some of these factors have already been mentioned in section A.3.4. These factors can have a positive effect on vegetation growth, and thus an increase in sub-surface expansion. Conversely, when roots decompose, they take up less space, causing a reduction in soil volume and resulting in shallow subsidence. The swelling and shrinkage of soils can be attributed to an increase or decrease in the soil water content. Compaction of soils usually refers to the consolidation of soils over time, as soil particles are packed closer together and moisture is forced out of the soil. McIvor et al. (2013) state that there is little known about the factors affecting the compaction and compression of mangrove soils. Important factors are likely to be the weight of material or water pressing down on the soil, the relative volumes of particles

and pores, the soil composition (and particularly the organic content), and the depth of different soil layers.

B.3.3 Long-term tectonic and deep geological movements

Other factors which contribute to mangrove surface elevation and are not mentioned by [McIvor et al. \(2013\)](#), are deep tectonic processes ([Friess et al., 2012](#); [Glamore et al., 2015](#)). Surface elevation change induced by deep tectonic processes is due to multiple processes. First, the Glacial Isostatic Adjustment (**GIA**), which refers to the ongoing vertical movement of the land surface and changes in the earth's rotation following relief from extreme overburden pressures caused by thick ice sheets from the last ice age. **GIA** occurs in addition to tectonic movements or local land subsidence and is not uniform across the globe. According to [Glamore et al. \(2015\)](#), the **GIA** alone is projected to cause a slight fall of 0.4 mm per year in sea level relative to the land in **NSW**, Australia. Second, low-frequency, high-magnitude tectonic events over smaller spatial scales can cause instant changes in surface elevation. A less common cause of negative surface elevation change is deep, non-tectonic subsidence due to natural resource extraction. This is observed in both the Netherlands and the Mississippi delta [Friess et al. \(2012\)](#).

B.3.4 Effect of Sea Level Rise

According to [McIvor et al. \(2013\)](#) sea level rise is expected to affect several of the surface elevation processes within mangroves. First, a rise in sea level will result in an increased hydro-period, during which sedimentation can occur, possibly resulting in increased accretion. Second, a rise in sea level will increase water depth, allowing waves to penetrate further into mangrove areas. This can in turn lead to an increase in re-suspension and erosion of sediments, or to an increase in sediment delivery into the forest. Third, an increase in water logging is expected, which in turn leads to an absence of oxygen and thus possibly affecting root growth. Finally, groundwater levels are expected to rise, possibly affecting plant and sub-surface root growth. The above stated interactions are very hypothetical, since few studies have investigated them. However, it is clear that sea level rise could influence surface elevation change rates in multiple ways.

SLR requires mangroves to increase their surface elevation vertically (through sediment trapping or the addition of below-ground organic matter) and/or to move laterally inland to obtain an elevation gain that offsets the rate of **SLR**, so that the entire mangrove system maintains its relative position in the tidal frame [Willemsen et al. \(2016\)](#). Where possible, space should be allowed behind mangroves for their landward migration in the face of sea level rise. This will ensure that mangroves can continue to exist along a coast, even if they are not able to remain in their current location. For as long as some mangrove areas remain intact, they can be expected to continue to provide coastal defence services, such as wave reduction, and other ecosystem services, such as supporting fisheries. [McIvor et al. \(2013\)](#) The relationship between environmental factors and surface elevation change, and also any interactions between these processes are schematically shown in figure 58.

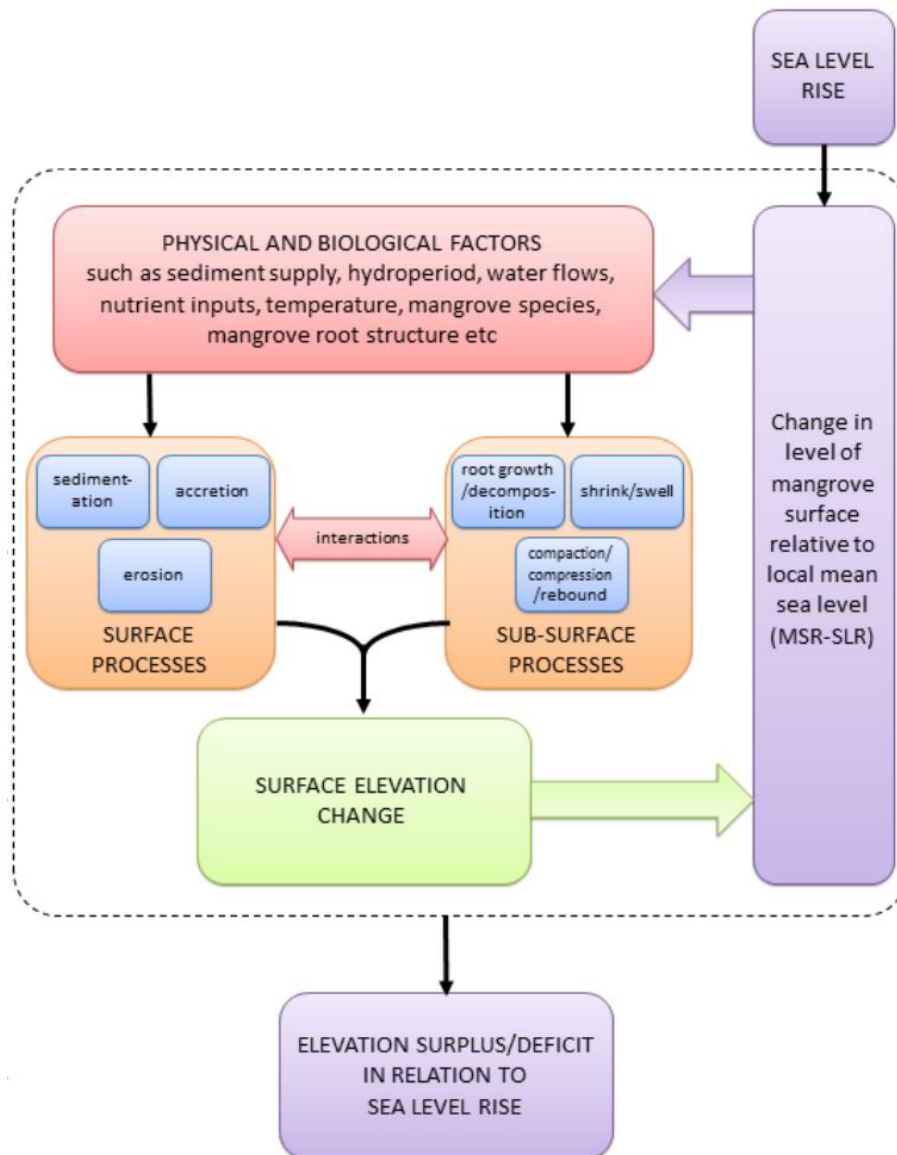


Figure 58: Environmental and biological factors influencing the surface elevation dynamics in mangroves (McIvor et al., 2013)

C Scenario results

C.1 Hydrodynamics

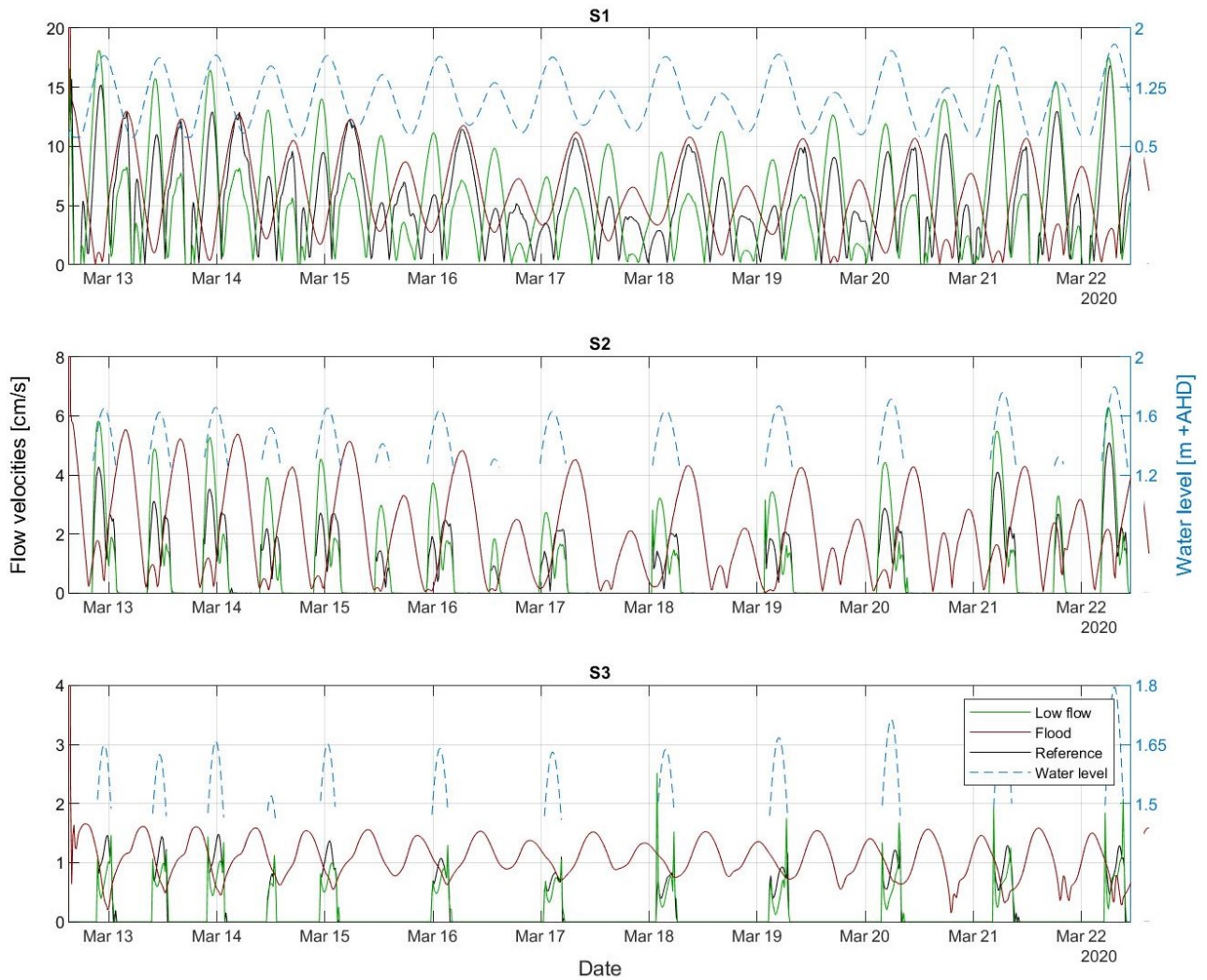


Figure 59: Modelled flow velocities at S1 for the four scenario's

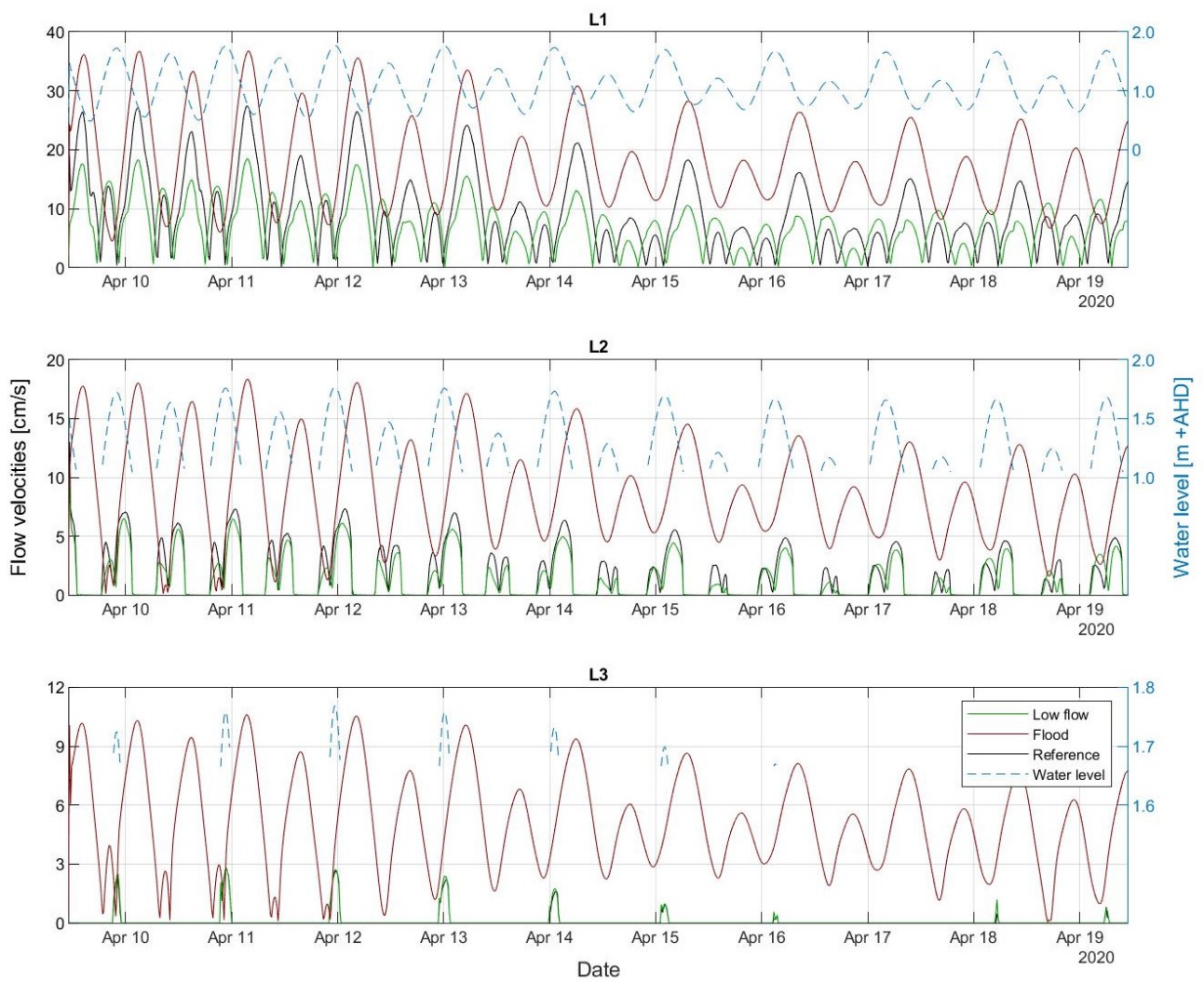


Figure 60: Modelled flow velocities at S1 for the four scenario's

C.2 Morphodynamics

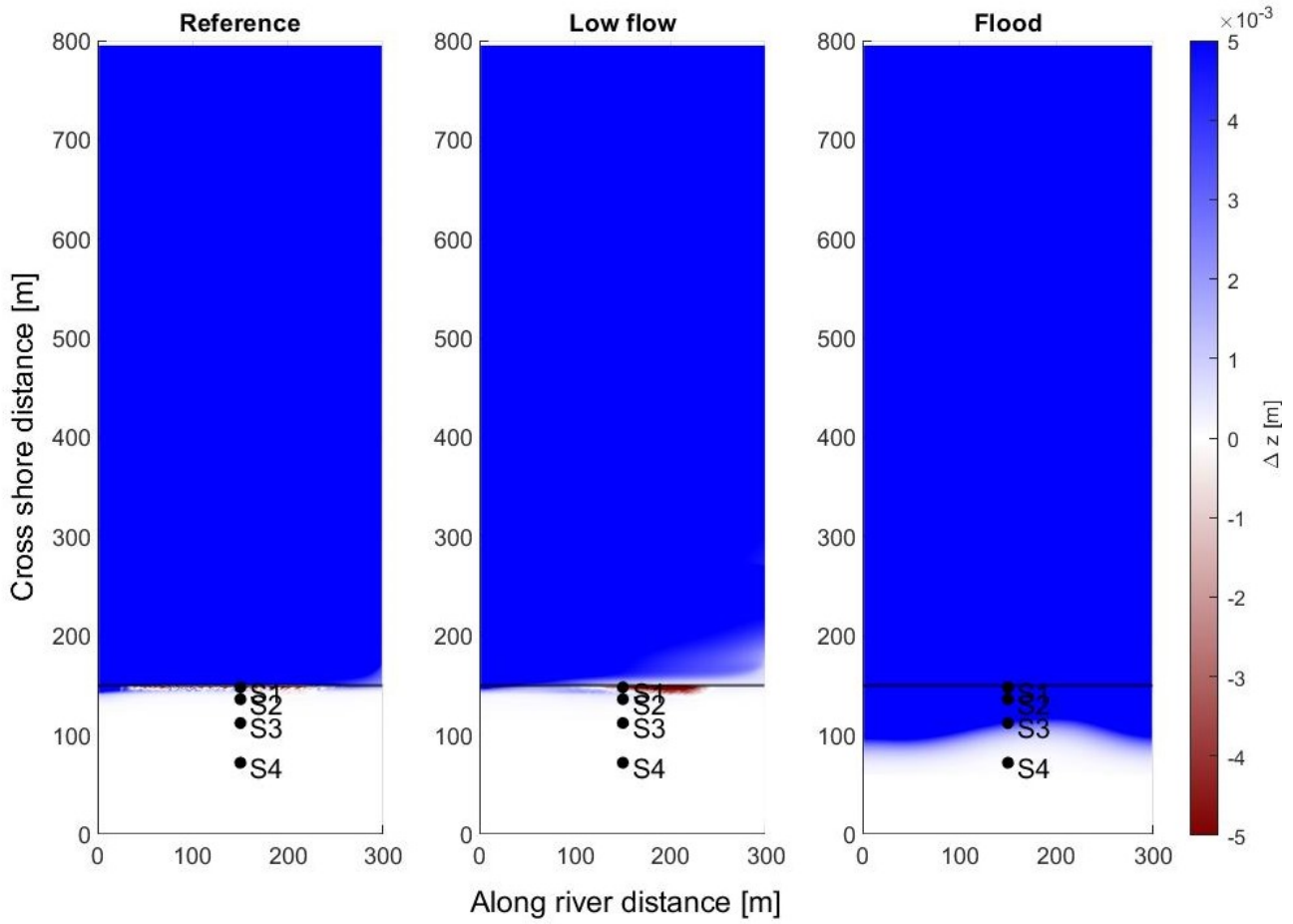


Figure 61: Deposition and erosion gradients across the domain for all scenario's. The black line indicates the location of the forest fringe. Red indicates erosion while blue indicates deposition.

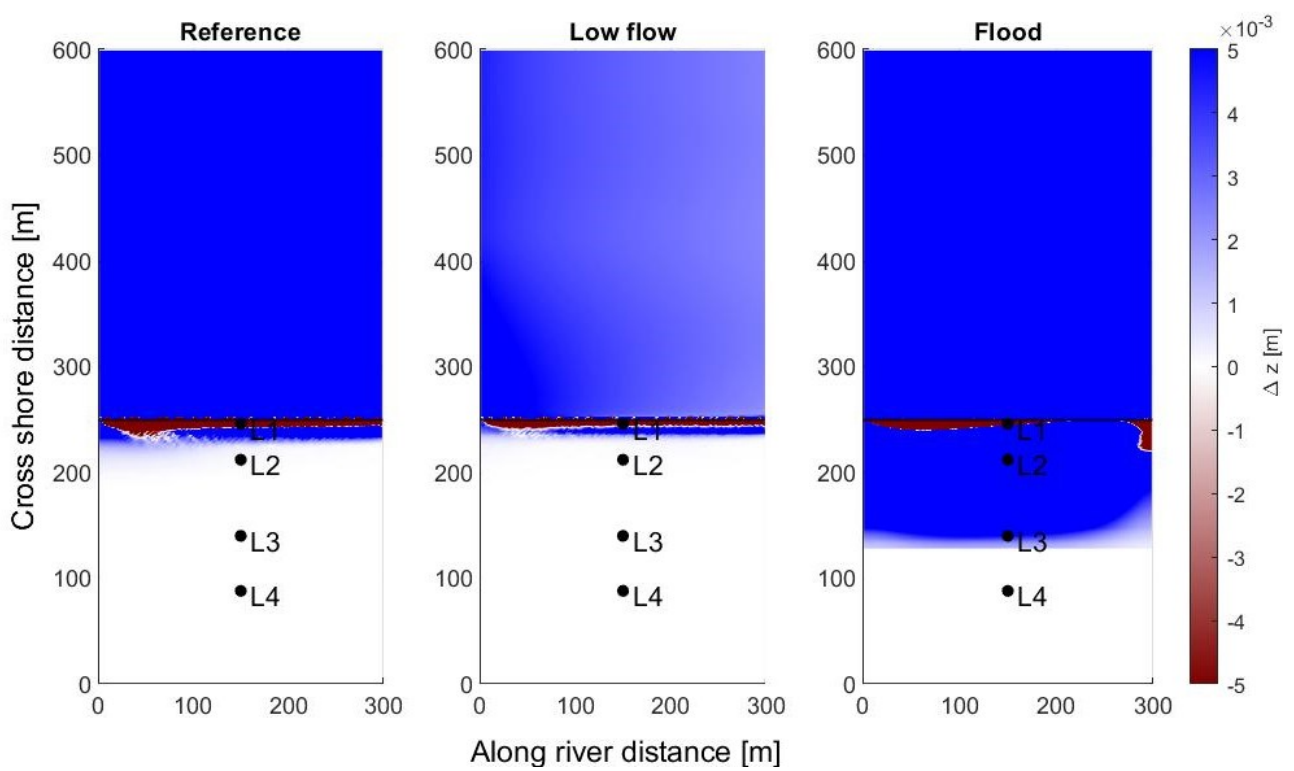


Figure 62: Deposition and erosion gradients across the domain for all scenario's. The black line indicates the location of the forest fringe. Red indicates erosion while blue indicates deposition.

D Flood scenario quiver

In the figures below, a close up of the direction of flow during the flood event can be seen. This snapshot is taken during a neap tide. It can be noticed that an eddy has formed within the transect, resulting in a inland directed flow.

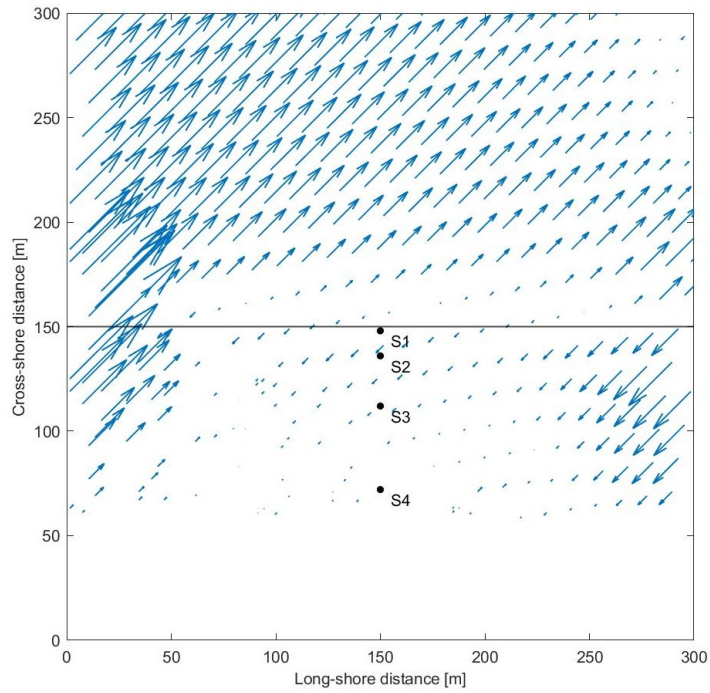


Figure 63: Direction of flow during the flood scenario. The black line indicates the fringe.

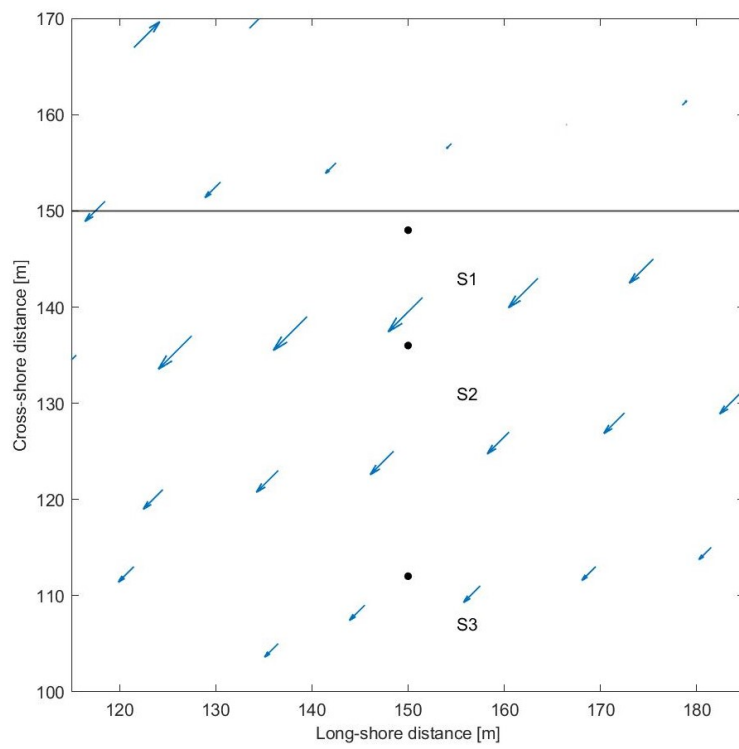


Figure 64: Close up of the quiver during the flood scenario.

E Direction of flow S-transect



Figure 65: Possible directions of flow during flood and ebb tide near the S-transect. Red arrows indicate river discharge, blue arrows indicate saltwater.